Portable X-ray Fluorescence and Nuclear Microscopy Techniques Applied to the Characterisation of Southern African Rock Art Paintings

by Ruan Steyn

Thesis presented in partial fulfilment of the requirements for the degree of Master of Science in the Faculty of Science, at Stellenbosch University

Supervisor: Prof. Paul Papka
Co-supervisor: Prof. Carlos Pineda-Vargas

April 2014

Stellenbosch University http://scholar.sun.ac.za

Declaration

By submitting this thesis electronically, I declare that the entirety of the work contained therein is my own, original work, that I am the sole author thereof (save to the extent explicitly otherwise stated), that reproduction and publication thereof by Stellenbosch University will not infringe any third party rights and that I have not previously in its entirety or in part submitted it for obtaining any qualification.

April 2014

Copyright © 2014 Stellenbosch University

All rights reserved

Stellenbosch University http://scholar.sun.ac.za

Acknowledgement

I would like to thank a number of people for their contributions to this work. Firstly thanks to my supervisor Prof. Paul Papka and co-supervisor Prof. Carlos Pineda-Vargas for their support and guidance throughout the project. Dr. Leon Jacobson for his valuable contribution as archaeology expert. Dr Brian Cross as experienced X-ray fluorescence software analyst, for his support with the spectra analysis code. Mr. Attie Esterhuyse, Dr. Marc Dupayrat and Dr. Mathieu Bauer from Thermo Scientific for their assistance with the hardware and software of the Thermo Scientific Niton spectrometer. Mr. Robert Redus from Amptek for his support on the Amptek spectrometer. The Geology Department of the University of Stellenbosch, specifically Ms. Cathy Clarke, and the McGregor Museum in Kimberley for making the samples available. Dr. Cynthia Sanchez-Garrido from the Central Analytical Facility at Stellenbosch for the standard reference materials. Prof. Shaun Wyngaardt for his contribution. The Materials Research Department (MRD) from iThemba Labs for the use of their facility. The National Research Foundation (NRF) for their financial support. Lastly but definitely not the least thanks to my family and friends for their support through this period, it is greatly appreciation.

Stellenbosch University http://scholar.sun.ac.za

Contents

Declaration **i**

Acknowledgement **ii**

Contents **iii**

Abstract **vii**

Uittreksel **ix**

List of Figures **xi**

List of Tables **xiv**

List of Appendices **xvi**

List of abbreviations and / or acronyms **xvii**

CHAPTER 1 INTRODUCTION **1**

1.1 INTRODUCTION 1

1.2 PROBLEM STATEMENT 2

1.3 LITERATURE REVIEW 2

1.4 RESEARCH OBJECTIVES 3

1.5 IMPORTANCE OF STUDY 3

1.6 RESEARCH METHODOLOGY 3

1.7 CHAPTER OUTLINE 4

CHAPTER 2 XRF SPECTROSCOPY AND PIXE THEORY **5**

2.1 INTERACTION OF PHOTONS WITH MATTER 5

2.2 XRF PROCESS AND CHARACTERISTIC X-RAY(s) 6

2.3 LABELLING OF X-RAY TRANSITIONS 6

Stellenbosch University http://scholar.sun.ac.za

2.4 FLUORESCENCE YIELD 8

2.5 MASS ATTENUATION COEFFICIENT 9

2.6 BREMSSTRAHLUNG 9

2.7 pXRF INTRODUCTION 11

2.8 pXRF SPECTROMETRY 12

2.8.1 X-ray Generator 13

2.8.2 Silicon Drift Detector (SDD) 14

2.8.3 Spectrometer Geometry 17

2.9 PROTON INDUCED X-RAY EMISSION (PIXE) 18

CHAPTER 3 SPECTRA EVALUATION AND CONCENTRATION EXTRACTION 20

3.1 SPECTRA SMOOTHING 22

3.2 SILICON ESCAPE PEAK 22

3.3 SUM PEAK REMOVAL 23

3.4 BACKGROUND REMOVAL 23

3.5 BLANK REMOVAL 24

3.6 INTENSITY EXTRACTION 24

3.6.1 Gaussian Peak Fitting: Linear Least Square 24

3.6.2 Gaussian Peak Fitting: Non-linear Squares 25

3.6.3 Non-Gaussian Fitting: Integrated 25

3.6.4 Non-Gaussian Fitting: Reference 25

3.7 CONCENTRATION EXTRACTION FOR PD-FP AND IOM-FP METHODS 26

3.8 LIMITATION OF THE SPECTRA EVALUATION AND CONCENTRATION EXTRACTION 27

Stellenbosch University http://scholar.sun.ac.za

CHAPTER 4 XRF TECHNIQUE VALIDATION 28

4.1 METAL ALLOY STANDARDS 29

4.1.1 Metal rock standards results 29

4.2 COIN STANDARDS 32

4.2.1 Coin standards results 32

4.3 ROCK STANDARDS 36

4.3.1 Rock standard preparation 36

4.3.2 Rock elemental conversion to oxide 36

4.3.3 Rock standards results 37

4.4 XRF TECHNIQUE VALIDATION CONCLUSIONS 39

CHAPTER 5 EXPERIMENTAL RESULTS 40

5.1 MOUNT AYLIFF ROCK ART FRAGMENT 40

5.1.1 Compound concentrations and conclusions 42

5.1.2 Semi-quantitative comparison of the two pXRF spectrometers 48

5.2 HA KHOTSO ROCK ART FRAGMENT 49

5.2.1 Compound concentrations and conclusions 51

5.2.2 PIXE elemental distribution map 53

5.3 ROCK ART PAINT THICKNESS PROPERTIES 55

5.4 EXPERIMENTAL RESULT CONCLUSIONS 55

CHAPTER 6 CONCLUSIONS AND RECOMMENDATIONS 57

6.1 CONCLUSIONS 57

6.2 RECOMMENDATIONS 59

Stellenbosch University http://scholar.sun.ac.za

BIBLIOGRAPHY 60

APPENDIX A: DIGITAL PULSE PROCESSOR [56] 66

APPENDIX B: PD-FP TFR INPUT FILE 68

APPENDIX C: ADMCA 75

APPENDIX D: LEVERBERG-MARQUARDT ALGORITHM 76

APPENDIX E: FP EQUATION 80

APPENDIX F: NITON XL3t AND AMPTEK SDD RESULTS FOR IRON (Fe) ALLOY METALS 81

APPENDIX G: AMPTEK SDD AND NITON XL3t COMPOUND CONCENTRATION RATIO VALUES FOR S, K_2O, CaO AND Fe_2O_3 83

APPENDIX H: ELEMENTAL MAPS OF THE HA KHOTSO ROCK OBTAINED WITH THE PIXE METHOD 85

Stellenbosch University http://scholar.sun.ac.za

Abstract

Non-destructive portable X-ray Fluorescence (pXRF) and Particle Induced X-ray Emission (PIXE) were used to measure the elemental concentration of rock art fragment paintings. For pXRF the Amptek Silicon Drift Detector (SDD) and Niton XL3t spectrometers were used to perform the measurements. These two spectrometers use different spectrum analysis methods. The Peak Deconvolution (PD) analysis method is used for the Amptek SDD and an Inverse Overlap Matrix (IOM) method is used for the Niton XL3t spectrometer.

The pXRF methods were validated by using alloys, coins and rock standards. The validation is important to establish if the pXRF technique is properly understood and used and to advance the investigation to more complex rock art paintings, with heterogeneous and layered properties. The elemental concentrations obtained for the Standard Reference Materials (SRMs), which were used for the validation, were in good agreement with that of the known concentration of the SRMs.

The two rock art fragments which were analysed from the Mount Ayliff and Ha Khotso caves were part of larger rock art painting prior to it being naturally exfoliated from the rock. For the Mount Ayliff rock art, seven paint points, two unpainted rock (varnish) point adjacent to the paint and the back of the rock were analysed. The colour of the paint ranged from black, shades of brown and shades of red. The black paint is due to manganese or charcoal. The red colour is due to iron oxide and the red-brown colour is due to Hematite (a type of ferrous oxide) [1]. For the Ha Khotso fragment the paint on the front of the rock and the rock substrate (back of the rock) were analysed.

For the Mount Ayliff rock art fragment the results for both pXRF spectrometers indicated that the elemental concentration was uniform across the fragment. This is due to the formation of a uniform layer of minerals such as silica and calcium introduced by the seepage of water through the cracks of the cave. Therefore no correlation could be established between the colour of the rock art paint and the elements detected, as was found with the work done by Peisach, Pineda and Jacobson [1]. For the Ha Khosto rock fragment a relation between the Ca composition and the cream colour of the rock art paint was established. Both the PIXE and pXRF techniques were used to identify the compound concentrations of the Ha Khotso rock art fragment. The comparison between the two techniques highlights the complexity of rock art paint analysis. The results from the PIXE elemental mapping indicated the non-uniform distribution of the elements in the analysed region.

Stellenbosch University http://scholar.sun.ac.za

From the rock art fragment measuring the analysed points 5 times and obtaining the same results, indicated that the particle size and inhomogeneities did not have much effect on the compound compositions.

In order to obtain high accuracy results with pXRF, sound scientific methodology with specific knowledge and expertise, not only about the XRF technique, but also about the sample under investigation is required. For alloy analysis pXRF is well suited, the analysis of geological material however more complex, since they are composed predominately of low atomic elements e.g. silicon, aluminium, magnesium, sodium, oxygen and carbon – all of which are excited with very low efficiencies.

Stellenbosch University http://scholar.sun.ac.za

Uittreksel

Nie-beskadigended X-straal Fluoresensie (pXRF) en Deeltjie Geinduseerde X-straal emmissie (PIXE) was gebruik om die elementêre konsentrasie van die rotstekeninge in hierdie studie te bepaal. Vir die pXRF-tegniek is die “Amptek Silicon Drift Detector (SDD)” en die “Thermo Scientific Niton XL3t” spektrometers gebruik gemaak om die metings uit te voer. Die twee spektrometers maak gebruik van verskillende spektrum analiseringsmetodes.Die “Peak Deconvolution (PD)” analiseringsmetode is gebruik vir die “Amptek SDD” en die “Inverse Overlap Matrix (IOM)” analiseringsmetode is gebruik vir die “Thermo Scientific Niton XL3t” spektrometer.

Vir die validasie van die pXRF-metode is van allooie, muntstukke en rots standaarded gebruik gemaak. Die validasie is belangrik om vas te stel of die pXRF tegniek behoorlik verstaan en gebruik word en om die ondersoek te bevorder na meer komplekse rotstekeninge, met heterogene en lae eienskappe. Die element konsentrasies wat vir die “Standard Reference Material (SRM)” wat gebruik is vir die validasie, was in 'n goeie ooreenkoms met die van die konsentrasie van die SRM, wat bekend is.

Die twee rotstekeninge wat ontleed is van die Mount Ayliff en Ha Khotso grotte en was deel van 'n groter rots kuns skildery voordat hul natuurlik afgebreek het. Vir die Mount Ayliff rotskuns, is sewe verf punte, twee ongeverfde rots (vernis) punte aangrensend aan die verf en die agterkant van die rots ontleed. Die kleur van die verf het gewissel van swart, skakerings van bruin en skakerings van rooi. Die swart verf kan toegeskryf word aan mangaan of houtskool. Die rooi kleur is as gevolg van ysteroksied en die rooi-bruin kleur is as gevolg van Hematiet ('n tipe van yster oksied) [1]. Vir die Ha Khotso rotskuns is die verf aan die voorkant van die rots en die rots substraat (agterkant van die rots) ontleed.

Vir die Mount Ayliff rotstekening het die resultate vir beide pXRF spektrometers aangedui dat die elementele konsentrasie uniform oor die rotstekening is. Dit is as gevolg van die vorming van 'n uniforme lagie van silica en kalsium, wat deur die sypeling van water deur die krake van die grot na die oppervlak van die rotstekening beweeg het. Daarom kon geen korrelasie tussen die kleur van die rotstekening en die elemente wat gemeet is bepaal word nie, soos gevind deur die werk van Peisach, Pineda en Jacobson [1]. Vir die Ha Khotso rotstekening is ‘n verband tussen die room kleur van die rotstekening verf en Ca konsentrasie gevind. Beide die PIXE en pXRF tegnieke is gebruik om die konsentrasies van die Ha Khotso rotstekening te identifiseer. Die vergelyking tussen die twee tegnieke beklemtoon die kompleksiteit van rotstekening verf analise. Die resultate van die PIXE elementele karakterisering het aangedui die nie-eenvormige verspreiding van die elemente in die ontlede area.

Stellenbosch University http://scholar.sun.ac.za

Deur die meting van die ontlede punte 5 keer te herhaal, en dieselfde resultate verkry, is ‘n aanduiding dat die deeltjie grootte en inhomogeniteite nie veel invloed op die elementele konsentrasies het nie.

Ten einde 'n hoë akkuraatheid resultate te kry met pXRF, moet goeie wetenskaplike metode toegepas word met spesifieke kennis en kundigheid, nie net oor die XRF tegniek, maar ook oor die rotstekening wat ondersoek word vereis. pXRF is wel geskik vir die ontleding van allooie, die ontleding van geologiese materiaal is egter meer kompleks, aangesien die materiaal hoofsaaklik bestaan uit lae atoomgetal elemente bv silikon, aluminium, magnesium, natrium, suurstof en koolstof - wat almal met lae doeltreffentheid opgewek en baie afgerem word in die materiaal.

Stellenbosch University http://scholar.sun.ac.za

List of Figures

Figure 2.1: X-ray interaction process.

Figure 2.2: X-ray fluorescence process [13].

Figure 2.3: Transitions that give rise to the various X-ray line emissions [14].

Figure 2.4: The K and L fluorescence yield as a function of atomic number, Z [13].

Figure 2.5: Amptek SDD Compton scattering spectrum for air with a Tungsten (W) X-ray tube.

Figure 2.6: pXRF system [13].

Figure 2.7: Transmission of X-ray from the X-ray generator [13].

Figure 2.8: Amptek SDD pXRF system setup.

Figure 2.9: Niton XL3t handheld XRF analyser [17].

Figure 2.10: Schematic cross section of a SDD with integrated FET [18].

Figure 2.11: Combination of the effect of transmission through the absorbers, such as the Beryllium window and the dead layer of the detectors, and the interaction in the SDD [19].

Figure 2.12: Geometry angles of a typical pXRF setup [20].

Figure 2.13: Van de Graff accelerator and NMP layout at iThemba Labs [21].

Figure 3.1: Peak Deconvolution (PD) processing steps [20].

Figure 4.1: Amptek SDD spectrometer spectrum for Brass.

Figure 4.2: Amptek SDD spectrometer spectrum for Nordic gold.

Figure 4.3: Amptek SDD spectrometer spectrum for the Krugerrand coin.

Figure 5.1: Mount Ayliff rock art fragment with the points that were characterised.

Figure 5.2: Amptek SDD spectrometer spectrum for the Mount Ayliff rock art fragment (point 1).

Stellenbosch University http://scholar.sun.ac.za

Figure 5.3 Elemental compositions by colour and back of the rock.

Figure 5.4: Compound and elemental concentration (wt %) per point for the Niton XL3t spectrometer.

Figure 5.5: Compound and elemental concentration (wt %) per point for the Niton XL3t spectrometer.

Figure 5.6: Compound and elemental concentration (wt %) per point for the Amptek SDD spectrometer.

Figure 5.7: Compound and elemental concentration (wt %) per point for the Amptek SDD spectrometer.

Figure 5.8: Ha Khotso rock fragment.

Figure 5.9: Amptek SDD spectrometer spectrum for the front of the Ha Khotso rock fragment.

Figure 5.10: CaO, S, CaO and Fe_2O_3 concentration measurements with the Amptek SDD and PIXE for the front and back of the Ha Khotso fragment.

Figure 5.11: K_2O, TiO_2, MnO and Cl concentration measurements with the Amptek SDD and PIXE for the front and back of the Ha Khotso fragment.

Figure 5.12: Si PIXE elemental composition map for the front of the rock.

Figure 5.13: Ca PIXE element composition map for the front of the rock.

Figure A.1: Block diagram of the Amptek SDD digital pulse processor DP5 [56].

Figure C.1: ADMCA program main display window.

Figure C.2: ADMCA window and calibrate dialog box.

Figure G.1: Amptek SDD and Niton XL3t ratio value for S at all points analysed.

Figure G.2: Amptek SDD and Niton XL3t ratio value for K_2O at the analysed points.

Figure G.3: Amptek SDD and Niton XL3t ratio value for CaO at the analysed points.

Figure G.4: Amptek SDD and Niton XL3t ratio value for Fe_2O_3 at the analysed points.

Stellenbosch University http://scholar.sun.ac.za

Figure H.1: Mg PIXE elemental composition map for the front of the rock.

Figure H.2: S PIXE elemental composition map for the front of the rock.

Figure H.3: K PIXE elemental composition map for the front of the rock.

Figure H.4: Fe PIXE elemental composition map for the front of the rock.

Stellenbosch University http://scholar.sun.ac.za

List of Tables

Table 2.1: Energy level and electron configuration.

Table 2.2: PD-FP (Amptek SDD) input values.

Table 4.1: SRM categories.

Table 4.2: Niton XL3t and Amptek SDD measurements for Stainless Steel 410.

Table 4.3: Niton XL3t and Amptek SDD measurements for CDA 715 alloy.

Table 4.4: Niton XL3t and Amptek SDD measurements for Inconel-600 alloy.

Table 4.5: Niton XL3t and Amptek SDD measurements for Ti-CP (Grade 2) alloy.

Table 4.6: Brass sample concentration results.

Table 4.7: Nordic gold coin concentration results.

Table 4.8: Copper coin concentration results.

Table 4.9: XRF analysis results of the Krugerrand coin [37].

Table 4.10: Stoichiometric factors [39].

Table 4.11: SARM 48 reference material [7].

Table 4.12: SARM 69 reference material [8].

Table 5.1: Compound and element concentration of measured points 1 to 5 for both the Niton XL3t and Amptek SDD spectrometers.

Table 5.2: Compound and element concentration of measured points 6 to 9 and back of the rock, for both the Niton XL3t and Amptek SDD spectrometers.

Table 5.3: Amptek SDD and Niton XL3t compound concentration ratio analysis for K_2O, CaO and Fe_2O_3.

Table 5.4: PIXE and Amptek SDD results for Ha Khotso rock art fragment.

Table F.1: Niton XL3t and Amptek SDD measurements for Stainless Steel 316 [57].

Stellenbosch University http://scholar.sun.ac.za

Table F.2: Niton XL3t and Amptek SDD measurements for Al 29-4-C alloy [58].

Table F.3: Niton XL3t and Amptek SDD measurements for F-255 alloy [59].

Table F.4: Niton XL3t and Amptek SDD measurements for 20Cb3 alloy [60].

Stellenbosch University http://scholar.sun.ac.za

List of Appendices

APPENDIX A: DIGITAL PULSE PROCESSOR [56]

APPENDIX B: PD-FP TFR INPUT FILE

APPENDIX C: ADMCA

APPENDIX D: LEVERBERG-MARQUARDT ALGORITHM

APPENDIX E: FP EQUATION

APPENDIX F: NITON XL3t AND AMPTEK SDD FOR IRON (Fe) ALLOY METALS

APPENDIX G: AMPTEK SDD / NITON XL3t COMPOUND CONCENTRATION RATIO VALUES FOR K_2O, CaO AND Fe_2O_3

APPENDIX H: ELEMENTAL MAPS OF THE HA KHOTSO ROCK OBTAINED WITH THE PIXE METHOD

Stellenbosch University http://scholar.sun.ac.za

List of abbreviations and / or acronyms

CAF	Central Analytical Facility
C/R	Compton-to-Rayleigh ratio
FP	Fundamental Parameter
FET	Field-Effect Transistor
FWHM	Full Width Half Maximum
IOM-FP	Inverse Overlap Matrix Fundamental Parameter
JFET	Junction gate Field-Effect Transistor
NMP	Nuclear Microprobe
PD	Peak Deconvolution
PD-FP	Peak Deconvolution Fundamental Parameter
PIXE	Particle Induced X-ray Emission
pXRF	portable X-ray Fluorescence
ROI	Region Of Interest
SDD	Silicon Drift Detector
SARM	South African Reference Material
SRMs	Standard Reference Materials
XRF	X-ray Fluorescence
Z	Atomic number

Stellenbosch University http://scholar.sun.ac.za

CHAPTER 1

INTRODUCTION

1.1 INTRODUCTION

South Africa has a very rich heritage of rock art, particularly rock paintings [2] left behind by the San hunter-gatherers, also known as Bushmen, which were the only inhabitants of a large part of the interior of the southern Africa. These rock art paintings can be found in caves or on rock faces, with visibility varying from very bright to barely visible. Common themes displayed were hunting scenes, animals and trance dance.

As the paintings are increasingly under threat of degradation, from a variety of causes, it is vital to carry out preferably non-destructive research to determine the elemental concentrations of rock art paint for preservation and future restoration purposes. In addition, the elemental concentrations of rock art paint can be used to obtain information about the raw material used during the paint preparation process, this will however not be explored in this study.

With the successful migration of the versatile XRF analytical technique, out of the laboratory to the field, rock art elemental concentration measurements with Portable X-ray Fluorescence (pXRF) have become increasingly common [3]. pXRF is a valuable technique with advantages such as, non-sample destructivity, quick analysis, portable and easy to use in field and the laboratory, relatively user friendly software interface and affordable equipment. Aaron N. Shugar from the Art Conservation Department of the Buffalo State College in New York, describe this period as an exciting time where the ongoing miniaturization of the analytical instrumentation has advanced to a state where traditionally lab-based analysis can now be performed in the field [4]. For pXRF the Amptek SDD and Niton XL3t spectrometer were used with a ‘point and shoot’ methodology. Data is collected by the spectrometer and propriety software is usually used for the determination of the elemental concentrations. The validation of the pXRF spectrometers were done by making use of various alloys, coins and rock reference materials.

Particle Induced X-ray Emission (PIXE) [5] which is a laboratory technique were also used, where protons generated by an accelerator and focused onto a very small area of the target material. PIXE is usually used to perform perform high sensitivity elemental concentration measurements [6].

The two rock art fragments from the Mount Ayliff and Ha Khotso caves were measured by making use of pXRF and PIXE.

Stellenbosch University http://scholar.sun.ac.za

1.2 PROBLEM STATEMENT

Since the rock art paintings degrade due to several causes such as weathering, the need to develop preservation and restoration strategy is of vital importance. This can be achieved by determining the elemental concentration of the rock art paint. Additionally surface deposition information, such as composition is necessary for patina restoration work.

The characterisation of the rock art paint can be challenging due to the fragment size, uneven or curved surfaces and variable thickness. According to Aaron N. Shugar, the fields of art and archaeology provide analysts with some of the most difficult sample to characterize [4].

1.3 LITERATURE REVIEW

X-ray fluorescence has a long and diverse history as an analytical technique. The development and miniaturization of components (detectors, X-ray tubes etc.) has facilitated the evolution of this powerful tool into a handheld / portable device [9,10]. The range of applications includes industries such as geology, mining, environmental and recycling. For geology pXRF is used for the characterization of rock, ores and metals in the mining industry. In the recycling industry pXRF has established itself as a technique of choice, due to its ability to accelerate the identification of alloys in scrap metals. Within the archaeology field itself, there have been diverse applications of XRF technology to analyse multiple materials. These include stones, rock art, stone based sculpture, architectural features such as glass, corroded metals, jewellery and museum collections. Several studies exploring the applicability of pXRF to a variety of case studies around the world has been conducted with great success [1,3,11,12]. These are however not the only application, many more related studies have been performed over the last decade as the equipment has improved.

Rock art which are represented in painting, drawings and engravings are essentially found across the world, including Africa, Australia, Southeast Asia, Europe, India, Northern and Southern America. These rock art sites typically form a very important part of the cultural heritage of the country and therefore the importance of developing conservation strategies to deal with problems that threaten rock art. These threats include water impact, salt decay, damage caused by animals and insects, soil and vegetation cover impact, site visitors and vandalism (graffiti). As a step towards the preservation and possible future restoration of the rock art, elemental concentration analysis of the rock art paint is performed by using a variety of both destructive and non-destructive techniques [1,3]. The elemental concentration of rock art paint is usually used to obtain information about the raw material used during the paint preparation process. Since the rock art usually consists of a large scheme of colours ranging from black, shades of brown and shades of red, the elemental concentrations of each individual colour is usually performed.

Stellenbosch University http://scholar.sun.ac.za

1.4 RESEARCH OBJECTIVES

This work focuses on the determination of the rock art elemental concentration of two fragments from the Mount Ayliff and Ha Khotso caves, to investigate four concepts:

1. Can the elements of the rock art paint be correctly identified by the two spectrometers?
2. Are the elemental concentration results obtained from the two different pXRF spectrometers in good agreement ?
3. Are the pXRF and PIXE results in good agreement ?
4. Is there a correlation between the colour of the rock art paint and the elements measured ?

1.5 IMPORTANCE OF STUDY

The non-destructive elemental concentrations measurements of rock art fragments can assist with the preservation and restoration strategies of rock art. Furthermore, accurate elemental concentrations results are not merely achieved by trusting the output results from the pXRF spectrometer, thorough information about the rock art fragment investigated should be known.

1.6 RESEARCH METHODOLOGY

The validation of the analytical pXRF technique was done with homogeneous standard reference materials (SRMs) with known composition and concentration. The SRM included nine alloys, three coins standards and two rock standards. The SRMs used for validation of the XRF technique where specifically selected to cover a range of atomic numbers (13 to 82) and different combinations of atomic numbers.

The validation of the homogeneous SRMs are important, to advance the investigation to unknown heterogeneous layered samples, such as the rock art paintings from the Mount Ayliff and Ha Khotso caves.

Stellenbosch University http://scholar.sun.ac.za

1.7 CHAPTER OUTLINE

Chapter one provided an overview of the importance, objectives and research methodology followed for this study. A literature review of relevant previous studies conducted to determine elemental concentration of rock art paint, with similar techniques is also included.

Chapter two cover the pXRF and PIXE theory which include concepts such as interaction of photons with matter, characteristic X-ray(s), labelling of the X-ray transitions, fluorescence yield, mass attenuation coefficients and bremsstrahlung. These concepts are fundamental to the understanding of the techniques. The experimental setup and components of each technique is also discussed.

Chapter three discusses the spectra evaluation and concentration extraction methodology followed.

Chapter four will provide the results of the pXRF technique validation. This is important to establish if the pXRF technique is properly understood and used.

Chapter five will provide the results of the measurements done on the rock art fragments. This chapter will also indicate if the elements are correctly identified and if there is a significant difference between the results for the different techniques.

Finally, chapter six will conclude the study and offer recommendations.

Stellenbosch University http://scholar.sun.ac.za

CHAPTER 2

XRF SPECTROSCOPY AND PIXE THEORY

2.1 INTERACTION OF PHOTONS WITH MATTER

The interaction of the X-ray(s) with matter can either be by absorption or scattering process. In materials with finite thickness some of the X-ray(s) can also be transmitted, as illustrated in Figure 2.1. The favoured process depends on the sample thickness, density, composition and the incident X-ray energy.

The absorption process occur when the X-ray interact with the absorbing material at atomic level to transfer its entire energy and causes XRF, which form the basis of XRF spectroscopy. Scattering involve the deflection of the incident photon with the scattered material, this can occur both with energy loss (Compton scattering) or without energy loss (Rayleigh scattering). Compton Scattering is the interaction between the incoming photon with the atoms of the target material which causes the photon to change direction.

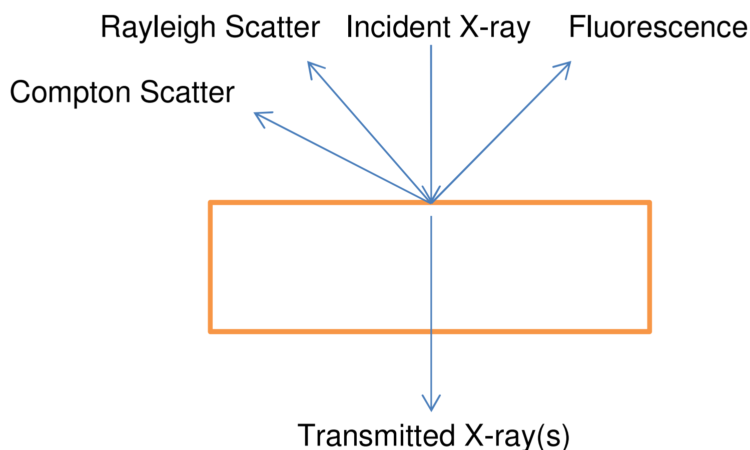

Figure 2.1: X-ray interaction process.

Stellenbosch University http://scholar.sun.ac.za

2.2 XRF PROCESS AND CHARACTERISTIC X-RAY(S)

For the Photoelectric absorption process to occur the energy of the photon needs to be equal or higher than the binding energy of the electron. An inner shell electron which is ejected after the incoming photon is completely absorbed leaves the atom in a highly excited state, since a vacancy has been created in one of the inner shells. The atom will return to its neutral state with the emission of a characteristic X-ray photon specific to the atom, also known as XRF and demonstrated in Figure 2.2. The energy difference between the ejected and replaced electron is characteristic of the element atom in which the fluorescent process occur. This is the key feature of XRF for elemental identification purposes.

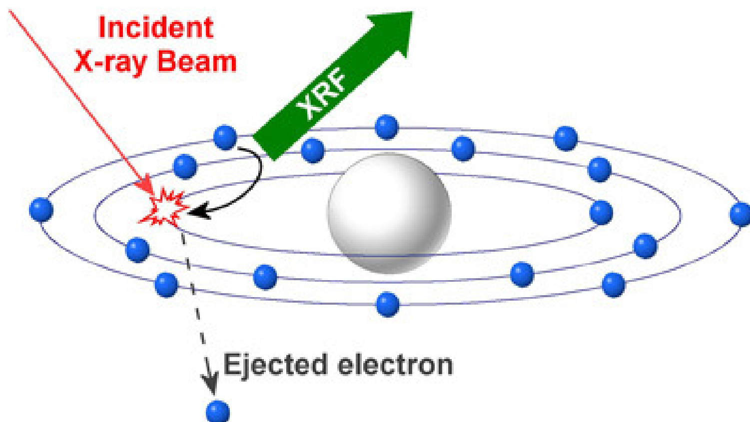

Figure 2.2: X-ray fluorescence process [13].

2.3 LABELLING OF X-RAY TRANSITIONS

With each unique atom having a number of available electrons and with all having different possible de-excitation routes, a set of selection rules have been defined to account therefore. Each electron in an atom can be defined by a set of four unique quantum numbers: n, l, m and s. The principal quantum number n take all integral values, with n = 1 being the K level and n = 2 the L level, the angular quantum number l taking all the values from n - 1 to zero, the magnetic quantum number m taking value from + l to – l and the spin quantum number s with a value of ± 1/2. The total momentum J of an electron is given by the vector sum of $l + s$.

The production of diagram lines requires that the principal number change by at least one (Δ n >= 1), the angular quantum number must change by at least one (Δ l = ± 1), and the J quantum number must change by zero or one (ΔJ = 0, ±1). Hence not all transitions from the outer shells or subshells are allowed, only those obeying the selection rules for electric dipole radiation. The transition that is not allowed is called forbidden lines, which arise from outer orbital levels where there is no sharp energy distinction between the orbitals.

The theory of X-ray spectra shows the existence of a limited number of allowed transitions, the rest is “forbidden”. The X-ray lines and energy levels are shown in the Figure 2.3 and Table 2.1:

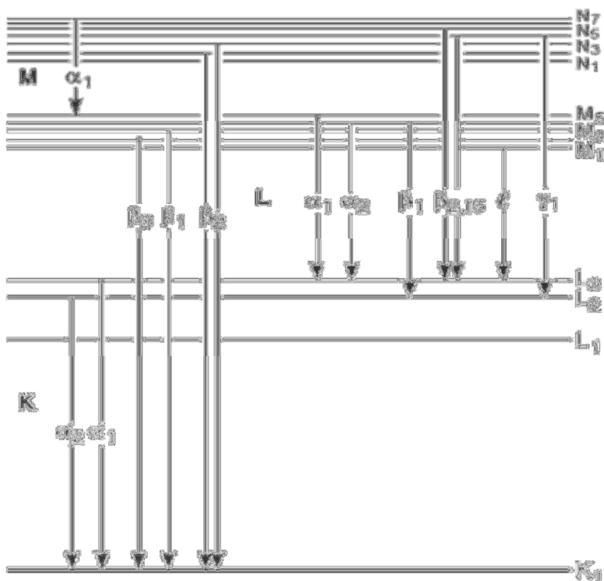

Figure 2.3: Transitions that give rise to the various X-ray line emissions [14].

Energy level	*Principle number n*	*Angular number l*	*Total momentum j*	*Electron configuration*
N_7	4	3	7/2	$4f_{7/2}$
N_5	4	2	5/2	$4d_{5/2}$
N_3	4	1	3/2	$4p_{3/2}$
N_1	4	0	1/2	4s
M_5	3	2	5/2	$3d_{5/2}$
M_3	3	1	3/2	$3p_{3/2}$
M_1	3	0	1/2	3s
L_3	2	1	3/2	$2p_{3/2}$
L_2	2	1	1/2	$2p_{½}$
L_1	2	0	1/2	2s
K_1	1	0	1/2	1s

Table 2.1: Energy level and electron configuration.

Stellenbosch University http://scholar.sun.ac.za

For example when an electron ejected from a K shell, the electron vacancy will be filled by an electron coming from the L shell. The transition is accompanied by the emission of an X-ray line known as the K_α line and leaves a vacancy in the L shell. If the atom already has sufficient electrons, the K shell vacancy might be filled by an electron coming from an M level that is accompanied by the emission of the K_β line. All the energies of the principal X-ray emission lines for the K and L shell can be found in Appendix II, Table 4 of Reference [15].

2.4 FLUORESCENCE YIELD

For an electron to be expelled from one of the orbitals, the X-ray energy must exceed to binding energy of the electron. Below the binding energy a drop in absorption is observed since the energy is not sufficient to emit electrons from that shell and too high in energy to emit electrons form the lower energy shells. If the energy is too high only a few electrons will be knocked out. As X-ray energy reduces and approaches the electron binding energy, the yield of the expelled electrons increases.

Since not all incident X-ray(s) result in the emission of characteristic X-ray(s) fluorescence, fluorescence yield is the ratio of fluorescence X-ray(s) to incident X-ray(s), as illustrated in Figure 2.4.

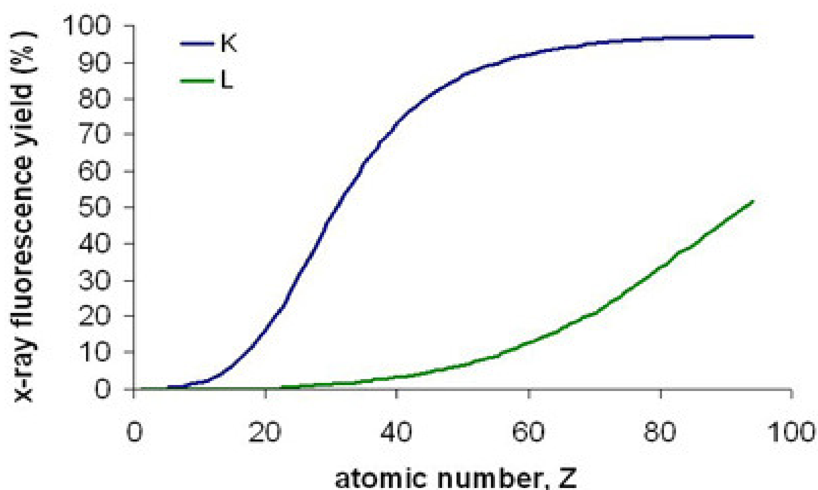

Figure 2.4: The K and L fluorescence yield as a function of atomic number, Z [13].

From Figure 2.4 it can be seen that the yield is low for light elements and high for heavy elements, this is mainly due to the Auger effect. This is a phenomenon were the filling of an inner shell vacancy of an atom is accompanied by the emission of an electron from the same atom i.e. instead of X-ray fluorescence, emission energy can be transferred to another electron, which is ejected from the atom. A consequence of the Auger effect is that the actual number of X-ray photons produced from an atom is

Stellenbosch University http://scholar.sun.ac.za

less than expected, since the vacancy in a given shell might be filled through non-radiative transition. Auger electrons are predominately produced during relaxation of K-shell ionisation of light elements ($Z < 20$) [15].

2.5 MASS ATTENUATION COEFFICIENT

The attenuation coefficient is the quantity that characterise how easily the material can be penetrated by an X-ray. A large attenuation coefficient is an indication that the X-ray is quickly attenuated (weakened) as it passes through the medium and a small attenuation coefficient means that the X-ray goes through the material quite easily.

The mass attenuation coefficient $\mu\ (\frac{cm^2}{g})$ is defined as the ratio of linear attenuation coefficient and the density of the material. The equation for the linear attenuation coefficient μ* per centimetre of travel in the absorber is:

$$\mu^* \left(\frac{1}{cm}\right) = \sigma_{tot} \left(\frac{cm^2}{atom}\right) \rho \left(\frac{g}{cm^3}\right) \frac{N_0}{A} \left(\frac{atoms}{g}\right)$$

where ρ is the density of the medium and N_0 is Avogadro's number.

Where σ_{tot} is the sum of the probability for each of the competing interaction processes. The sum of these cross sections is normalized to a per atom basis

$$\sigma_{tot} = \tau + \sigma_C + \cdots$$

where τ is the total Photoelectric absorption cross section per atom and σ_C the Compton collision cross section.

2.6 BREMSSTRAHLUNG

Bremsstrahlung occurs following the deceleration (loss of energy) of the electrons within the material, due to the interaction of the impinging electrons with the target elements. Hence at each collision as the electrons are decelerated part of the kinetic energy is lost and emitted as X-ray photons.

During a collision with material an electron can lose any amount of energy between zero and E_{max} which results in a bremsstrahlung continuum with energies in that range, as presented in Figure 2.5. The characteristic lines of Tungsten (W) and Argon (Ar) are superimposed on the bremsstrahlung continuum. The W is introduced from the anode material and the Ar from the air space between the sample and detector.

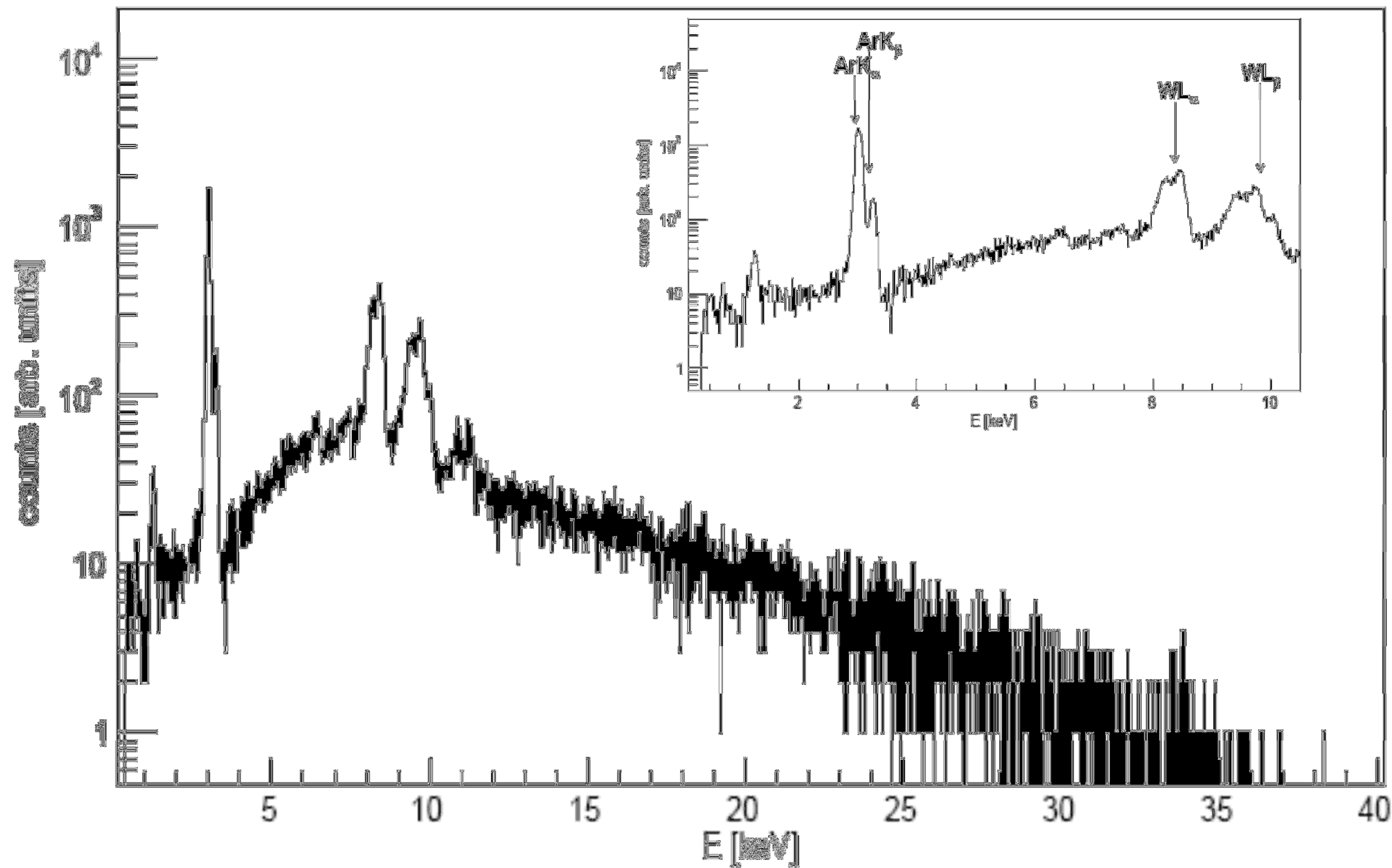

Figure 2.5: Amptek SDD Compton scattering spectrum for air with a Tungsten (W) X-ray tube.

2.7 pXRF INTRODUCTION

XRF spectroscopy is the technique used to analyse fluorescent X-ray(s), in order to determine the elemental composition of a particular material. The components of the pXRF device are a source of X-ray(s), a sample, detector, spectrometer and processor (computer), as illustrated in Figure 2.6.

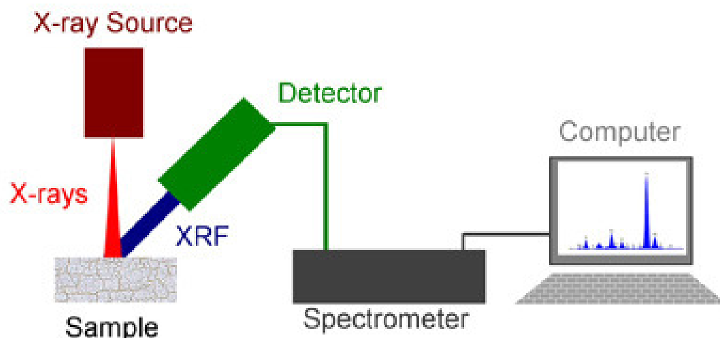

Figure 2.6: pXRF system [13].

The operating principle of an X-ray generator is to pass an electric current through a filament which causes electrons to be emitted. These electrons are then accelerated by high voltage (typically 25 – 50 kV) towards an anode (which is typically made of Ag or W material). The deceleration of the electrons (when they hit the anode material) causes an X-ray continuum to be emitted, known as Bremsstrahlung. Additionally a fraction of the electrons will cause characteristic X-ray fluorescence from the anode material. Hence the energy spectra from the X-ray generator will be the characteristic fluorescence lines from the target material superimposed on the broad bremsstrahlung continuum. This energy spectrum is then directed to the sample through the Beryllium (Be) window, as illustrated in Figure 2.7.

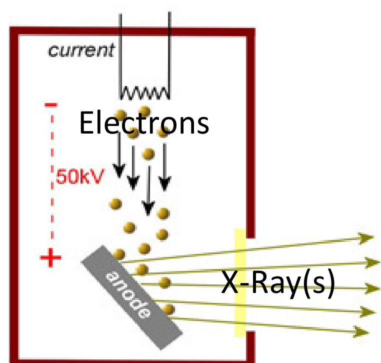

Figure 2.7: Transmission of X-ray from the X-ray generator [13].

The X-ray detector converts X-ray photon energies into measureable and countable voltage pulses. This is done by photoionization, where the interaction between the incoming X-ray photon and the active detector material produces an energetic electron which in turn produces many more. The incident X-ray is therefore essentially absorbed by the detector material, and causing one or more electron-hole pairs to form. The energy to do this is fixed for that particular material and therefore the X-ray will form as many electron-hole pairs as its energy will allow. These electrons are pulled of the detector to produce a current (which is proportional to the number of electron-hole pairs and directly related to X-ray energy) and converted into a voltage with amplitude proportional to the incident energy, by using a capacitor and resistor i.e. a voltage is thus generated for every X-ray photon that enters the detector.

The pre-amplification and processing electronics are then employed to maintain the linearity of the voltage signal with respect to the original charge pulse. In other words the rate at which the voltage signal is recorded is the same as the rate at which the X-ray photons enter the detector.

Therefrom, the multichannel analyser accumulates an energy spectrum of the sequential events in a histogram memory. The counts associated with a photon of a specific energy should hypothetically end up in a signal channel, but are distributed in a Gaussian fashion over several adjacent channels in the spectrum due to the statistical fluctuations in the number of electron-hole pairs created when an X-ray of a given energy enters the detector.

2.8 pXRF SPECTROMETERS

The two pXRF spectrometers used are the Amptek Silicon Drift Detector (SDD) and the Niton XL3t, with a Tungsten (W) and Silver (Ag) X-ray anode tube respectively, as demonstrated in Figure 2.8 and Figure 2.9. Both the spectrometers are capable of 40 kV excitation energy and uses SDD for detection. The spectrometers were placed as close as possible to the sample to minimize the X-ray attenuation by air, especially for the low energy X-ray(s) [16].

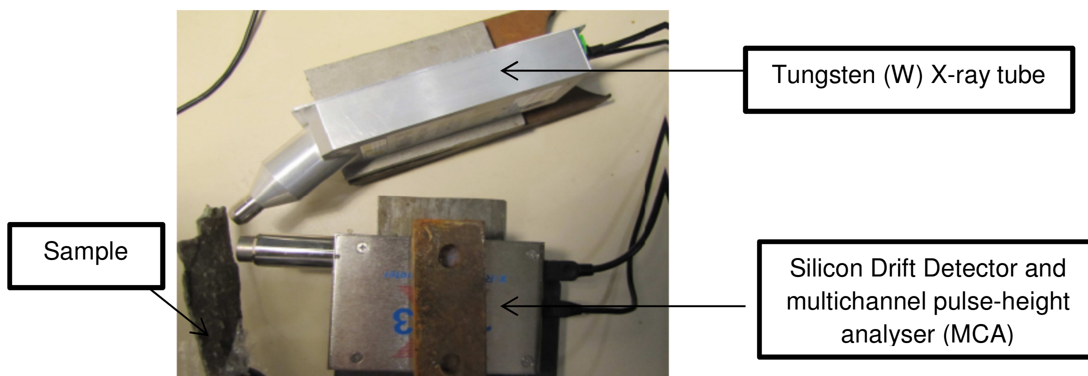

Figure 2.8: Amptek SDD pXRF system setup.

Stellenbosch University http://scholar.sun.ac.za

Figure 2.9: Niton XL3t handheld XRF analyser [17].

2.8.1 X-ray Generator

For the Tungsten (W) anode material, the L line is most effectively used for the exciting of light elements in the range of 1 - 10 keV, since the L_β line and L_α line for W is at 9.81 keV and 8.36 keV respectively. For higher energy lines for example Zirconium Zr K_α at 15.78 keV the L lines of W provide no excitation as they are lower in energy than the absorption edge of the Zr K line at 17.99 keV. Hence the bremsstrahlung hump provides the excitation. For Ag as anode material the K_β, K_α, L_β and L_α line energies are at 25.20 keV, 22.08 keV, 3.25 keV and 2.99 keV, respectively.

The energy distribution directed towards the target governs the effectiveness of excitation and hence the importance of selecting the most optimal excitation energy (eV) and accelerating voltage (kV). The limited counting capacity of the detector and the multi-elemental samples are adding complications to the derivation of the optimum excitation conditions. For X-ray fluorescence to be generated it is necessary to have incident X-ray energies above the absorption edge of the elemental line series that needs to be excited. A general rule of thumb is to use an X-ray tube voltage of about 1.5 to 2 times higher than the absorption edge of interest.

Stellenbosch University http://scholar.sun.ac.za

2.8.2 Silicon Drift Detector (SDD)

The SDD consists of a volume of n-type silicon bulk depleted from both sides: a homogeneous, shallow p^+-n junction on the side where the incoming radiation enters the detector and a structure of circular p^+ drift rings on the opposite side as shown in Figure 2.10.

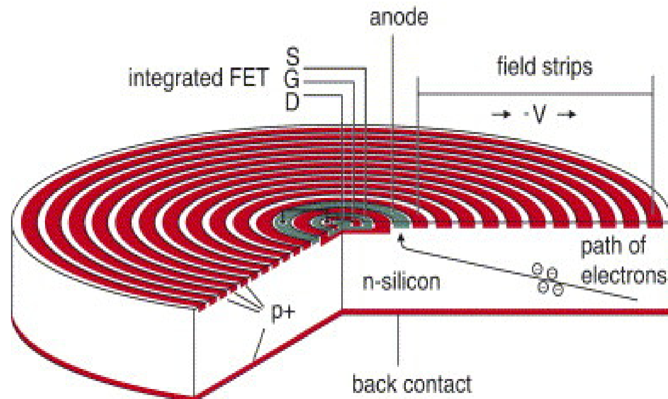

Figure 2.10: Schematic cross section of a SDD with integrated FET [18].

By applying a negative voltage on the homogeneous back side (radiation entrance window) and an increasingly negative voltage on the drift rings, a potential field distribution is created inside the detector such that the electrons generated by the absorption of ionizing radiation drift towards a small sized collecting anode situated in the centre of the device. The detector spectroscopic performance is improved by integrating the first amplification stage (a JFET transistor as shown in Figure 2.10) directly into the sensor. The connection of the anode to the transistor gate is reduced to a small metal strip of a few microns length, which suppress some electronic noise.

In order to minimize the noise from these thermally generated charges, the detector crystal (active part of the detector) must be kept cold throughout the time the bias is applied. This is produced by thermoelectric, Peltier cooling. If cooling is lost or degrades over time the automatic bias shutoff system (temperature sensor) will be activated, which will switch the detector off. Cooling is further essential to minimise the detector leakage current, the main source of noise in a detector, which is derived from the generation of charge carriers in the absence of X-ray(s) through the thermal vibration of the detector crystal lattice. Additionally the detector head (crystal and FET) is enclosed within vacuum, which is retained by a thin (typically 5-50 μm) beryllium entrance window. Any H_2 escaping through the window degrades the high vacuum and leads to increased temperature, leakage current and deteriorating performance.

Stellenbosch University http://scholar.sun.ac.za

Important feature of a detector is the energy resolution. This the precision with which the energy of specific X-ray(s) photons can be determined. Energy resolution is usually expressed as Full Width Half Maximum (FWHM) of the pulse-height distribution measured at a specific energy. With the 7 mm^2 Amptek SDD detectors a FWHM of approximately 140 eV at 5.9 keV for a shaping time (the time constant of the detector) of 9.6 μs is achievable. The resolution of the Niton XL3t varies between 145 to 165 eV for a shaping time of 4 μs or between 155 to 175 eV for 1 μs shaping time.

The FWHM might give a good indication of the quality of the detection system, but other factors such as the maximum count rate, the presence of background and artifacts is of similar importance.

The measured FWHM of the X-ray line (ΔE_{Total}) is the quadratic sum of the contribution due to the detector intrinsic resolution processes (ΔE_{Det}) and that associated with the electronic pulse processing system (ΔE_{Elec}) [15]:

$$\Delta E_{Total} = \sqrt{{\Delta E_{Det}}^2 + {\Delta E_{Elec}}^2} \quad . \tag{3.1}$$

The contribution to resolution associated with electronic noise (ΔE_{Elec}) is due to random fluctuations in thermally generated leakage currents within the detector and in the early stages of the amplifier components, which are intrinsic processes to the overall measurement process. ΔE_{Det} is a result of the statistics of the free-charge production process occurring in the depleted volume of the SDD.

The intrinsic full energy efficiency of a detector corresponds to the probability that an X-ray will enter the front of the detector and deposit all its energy inside the detector via the photoelectric effect. Near-unity intrinsic efficiencies for the detector over a wide range of X-ray energies (2 keV to 15 keV) are can be seen in Figure 2.11 for the Amptek SDD. The high-energy limits are established by the photoelectric cross section of the detector material (silicon) and the thickness of the active depth of the SDD (500μm). The low-energy cutoff is determined by the thickness of the Beryllium window either 0.3 mil (8 μm), 0.5 mil (12.5 μm) and 1 mil (25 μm) as well as the presence of a thin absorbing layer and dead layer on the surface of the detector. The thin absorbing layer is for protection purposes and the dead layer, which is effectively inactive and no charge can be collected.

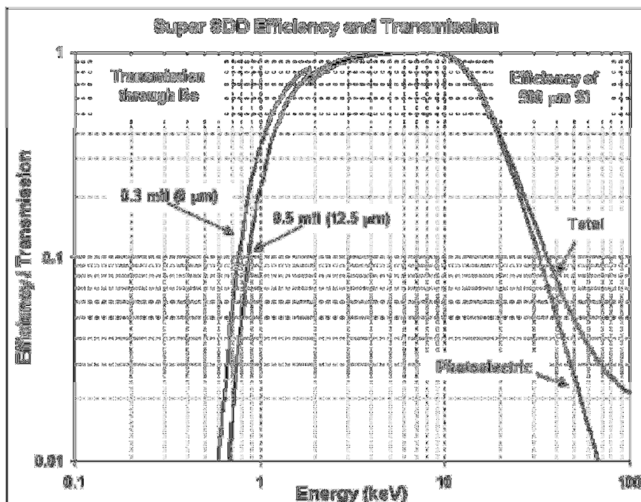

Figure 2.11: Combination of the effect of transmission through the absorbers, such as the Beryllium window and the dead layer of the detectors, and the interaction in the SDD [19].

Most of the photons (with different energies) coming from the sample interact with the detector, except the photons that just pass right through. The detector signal processing chain processes these events in a range of 1 – 500 Hz. A detailed description of the functioning of a digital pulse processor is presented in Appendix A.

For the digital pulse processor there is effectively a trade-off between accuracy or resolution ability and speed [15]. When the shaping time is increased the best resolution is achieved (lowest FWHM) at the expense of a lower count rate. When the count rate increases the resolution degrades. Hence an optimum for resolution and count rate needs to be established. In cases where severe peak overlaps exist, the best resolution should be selected. For light elements measurements the excitation condition need to be optimized to make best use of the limited count rate available. This is done by using two important parameters, namely current of the x-ray generator and measuring time.

The count rate limitations associated with semiconductor spectrometer are an inherent property associated with the finite pulse processing time required by the electronic shaping network. When a random sequence of pulses is incident on the detector system, the events cannot be processed without uncertainty. For each event a total pulse processing time τ_d is required after the arrival of the pulse and before the system is ready to accept the next event. This means that the events are statistically uncorrelated and thus implies that the events are not uniformly distributed in time. Hence there is a probability that two pulses will occur within the same processing time interval and causes pulse overlap. With low counting rate, pulse overlap is not a limiting factor, but as the count rate is increased the probability that the second event will occur before the first has been processed, also increases [15]. If the two events occur within a time internal less than the shaping time of an amplifier, the charge signals are indistinguishable and a “pileup” energy signal results. Modern systems rely on the inspection of fast discriminator output to

Stellenbosch University http://scholar.sun.ac.za

determine if two pulses have occurred in rapid succession. Logic is used to gate the output of the processor to eliminate the resultant uncertain energy signal and produces an uncertain pileup energy output [15].

2.8.3 Spectrometer Geometry

The geometric angle values for the Amptek SDD which form part of the input values for the Peak Deconvolution Fundamental Parameter (PD-FP) method are shown in Table 2.2 and schematically illustrated in Figure 2.12. These angle input values together with information about the equipment properties from part of the PD-FP TRF input file, as presented in Appendix B.

Input parameters	Value
Distance between tube-sample (mm):	15
Distance between sample-detector (mm) :	15
Incident angle (°)	45
Take-off angle (°)	45
Scatter angle (°)	90
Alpha angle (°)	0

Table 2.2: PD-FP (Amptek SDD) input values.

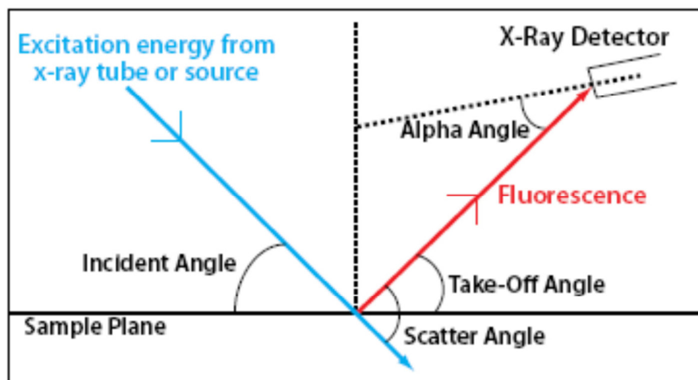

Figure 2.12: Geometry angles of a typical pXRF setup [20].

For the Niton XL3t spectrometer there is no need to provide the analysis software with the geometry, since the experimental angle values are fixed and encoded in the software. From the Niton XL3t product specification the values of the $\theta_{tube\text{-}and\text{-}surface}$ and $\theta_{detector\text{-}and\text{-}surface}$ is given as 71° and 61° respectively.

Stellenbosch University http://scholar.sun.ac.za

2.9 PROTON INDUCED X-RAY EMISSION (PIXE)

The nuclear microprobe is used for quantitative nondestructive microanalysis for various fields including, material science, geology and biomedicine. This is due to the significant progress that has been made with the instrumentation hardware, such as lenses, collimator slits, data acquisition systems and target chambers. The nuclear microprobe combined with PIXE, can detect trace elements to the sensitivities of a few ppm (or even sub ppm) concentrations.

A schematic of the 6 MV Van de Graaff Accelerator equipped with a Nuclear Microprobe (NMP) at iThemba Labs, is shown in Figure 2.13.

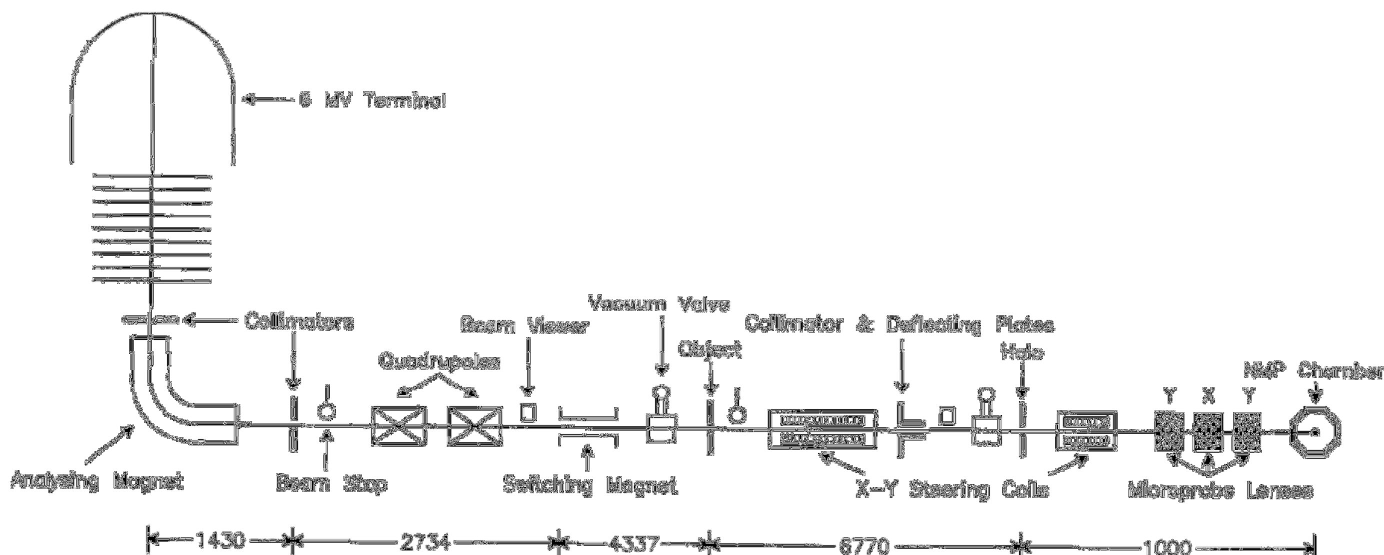

Figure 2.13: Van de Graff accelerator and NMP layout at iThemba Labs [21] (with the most important features shown, which distances in-between shown in mm).

The Van de Graaff accelerator accelerates ions vertically downwards, with energy stabilisation and beam selection made by a 90º analysing magnet. The ions then travel through a horizontal flight path to the target. After the analysing magnet, the ions travel through the energy stabilisation slits situated in front of the main beamstop. Ions then pass through a quadrupole duplet for focusing of the beam at the object slits. Before the object slits, the beam passes through a switching magnet with a narrow entrance port in the Y direction (1.2 mm), which is used for the beam lines at an angle to the NMP line. The primary beam is then allowed to pass through the object slits with a diameter of 1 mm [21].

A beam current of between 50–100 pA is transmitted through the collimator with the use of a variable slit. This allows the use of intense beams, for achieving the smallest beam spot size possible.

Stellenbosch University http://scholar.sun.ac.za

The target chamber is pumped down with a diffusion pump backed by a roughing pump; this allows for quick sample changing and higher throughput. The target chamber is the standard Oxford NMP chamber. The features include an X-ray detector situated 35 mm away from the target at 135º to the incoming ion direction, an annular Si surface barrier (SSB) detector situated close to 180º, channeltron electron detector for secondary electron imaging, electron suppression ring in front and behind the target and the optical microscope at 45º with respect to the normal to the sample surface. The target chamber allows for the stepper motor control of the samples for X, Y and Z axes. Signals from the detectors are fed to the normal electronic units for amplification and digitisation [21].

The data is collected by using the XSYS [22] acquisition system, with event-by-event storing capability, and the GeoPIXEII software package [23] is used for the extraction of the elemental concentrations, from the raw spectra.

For PIXE analysis the target material is bombarded with ions of sufficient energy (usually protons with energy in megaelectron volt (MeV) range) generated by an accelerator, instead of X-ray(s) as in the case of XRF.

The Ha Khotso rock art surface was scanned using a proton probe (microprobe), with energy of 3.0 MeV over an area of approximately 0.8 mm^2. The beam was focused to a minimum spot size of 3 μm^2 with a current of 100 pA. The scanned area were analysed in a rectangular pattern divided in a map size of 128 x 128 pixels, with a dwell time of ~10 ms/pixel. For the elemental mapping, PIXE and proton backscattering spectra were acquired simultaneously in event-by-event mode, using a Si (Li) PGT Pentafet X-ray detector with a 3.0 mm thick Si crystal. The detector diameter, surface area and resolution (FWHM) is 6.18 mm, 29.99 mm^2 and 160 eV at 5.898 keV for Mn, respectively. The count rate was kept below 1000 counts/second to avoid pulse pile-up and to achieve acceptable counting statistics. For the analysis of light elements such as Na and Mg, a proton probe with energy of 1.5 MeV and lateral resolution of approximately 2.5 μm^2 were used. Additionally a 25 µm Be absorber was used to stop the scattered ions reaching the detector.

Stellenbosch University http://scholar.sun.ac.za

CHAPTER 3

SPECTRA EVALUATION AND CONCENTRATION EXTRACTION

Spectrum evaluation uses mathematical techniques to extract peak intensities from the spectrum, which can be used to determine the elements and their concentration. This is done by using Peak Deconvolution Fundamental Parameter (PD-FP) or Inverse Overlap Matrix Fundamental Parameter (IOM-FP).

The PD-FP process is a series of steps used to remove the undesirable occurrences which contribute to the spectra. These steps are illustrated in Figure 3.1. The PD process relies heavily on mathematical techniques to extract useful information; therefore it is important to employ optimal experimental conditions to obtain the spectra, since this will determine the effectiveness of the PD process. Optimal conditions can be achieved in a number of ways either by increasing the counting statistics or by keeping the dead time low. Additionally control over the distance from the sample to the detector is essential to obtain enough statistics for the lower energy lines of the low atomic number elements. Factors internally performed by the electronics of the system such as keeping the detector cold and maintaining the stability of the high voltage power supply are of similar importance.

The IOM-FP process is an accelerated spectrum processing method which is much faster than the PD-FP spectra process. The IOM-FP process is usually required for certain applications where results are needed within a few seconds. This is done by using calibration standards with known Compton-to-Rayleigh (C/R) peak intensity ratios to generate calibration curves (XRF C/R peak intensity ratio versus atomic number). These curves are then use to determine the elements from the spectra. Since the elemental and corresponding peak intensity is known, the elemental concentration can be determined with the FP equations. Full detail of the IOM-FP spectra process is however not known, since it is propriety company information.

Prior to sample measurement an energy calibration needs to be performed. This is done by taking measurements of calibration standards with known elemental composition; since the exact energy of these elements are known [15]. The ADMCA display window for the calibration is presented in Appendix C.

The goal of quantitative XRF is to determine the concentration of the elements present in the sample; this is done by using the FP equations. A first estimate of the concentration is evaluated, from the measured intensities with the FP method, proposed by Criss and Birks [25]. This estimate is then used to calculate a new set of intensities from which a new revised estimate of composition is calculated. This process is iterated until the difference between two consecutive iterations becomes

Stellenbosch University http://scholar.sun.ac.za

insignificant. The main advantage of the FP equation is its theoretical exactness and the ability to correct for matrix effects. However a first estimate is necessary for this method to function properly. Frequently a poor first approximation is generated from measured intensities, because such intensities have been strongly modified by matrix effects. Matrix effects are the result of variations in the physical character of the sample and include parameters such as particle size, uniformity, homogeneity and surface condition [26].

The FP equations are calculated each iteration, which can cause the analysis process to be lengthy and slow. This is due to a large number of iterations which is sometimes required, since the first approximation of the composition is often very far from the final composition [27].

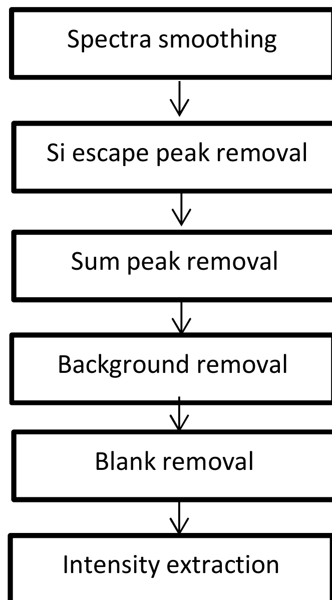

Figure 3.1: Peak Deconvolution (PD) processing steps [20].

Stellenbosch University http://scholar.sun.ac.za

3.1 SPECTRA SMOOTHING

The smoothing technique is ideal to remove or suppress statistical fluctuations, such as fictitious maxima which occur on both the continuum and on the slope of the characteristic peaks. Statistical fluctuations occur due to the uncertainty on each channel content y_i. The technique reduces the uncertainty in the data locally and redistributes the original channel content over the adjacent channels.

To smooth the fluctuating signals the moving average technique can be employed. For a measured spectrum y, a smoothed spectrum y^* is obtained, by calculating the mean channel content around each channel i [15]:

$$y^*_i = \bar{y}_i = \frac{1}{2m+1} \sum_{j=-m}^{+m} y_{i+j} \quad . \tag{3.1}$$

The smoothing effect depends on the width of the filter, $2m+1$. The filter can however introduce peak distortions, which depends on the filter-width-to-peak-width ratio. The peak distortion is caused by the fact that for the calculation of y^*_i , the content of all adjacent channels is used with equal weight. These peak distortions and broadening can be minimized by using a non-uniform filter with some weighing function that place more weight on the central channels and less on the edge of the filter [15]:

$$y^*_i = \frac{1}{N} \sum_{j=-m}^{j=m} h_j y_{i+j} \tag{3.2}$$

where h_j are the convolution integers and N is a suitable normalization factor.

3.2 SILICON ESCAPE PEAK

If the energy of the incoming X-ray(s) is higher than the Si K absorption edge at 1.832 keV, it can produce characteristic Si Kα X-ray(s) (E = 1.739 keV) from the XRF detector material, called escape peaks. Most of the Si K X-ray(s) will immediately be absorbed within the detector volume, because of their low energy and short range in materials. There is however a non-zero probability that the Si Kα X-ray(s) produced will escape from the detector volume and not contribute to the charge collected from the primary photon that was detected. The resulting lower energy peak is called Si escape peak. This usually occurs after photoelectric absorption of the impinging X-ray photon near the edge regions or the front of the detector crystal. The energy deposited in the detector by the incoming X-ray is therefore reduced by the escaping SiK photon energy (the escape peaks are at expected 1.739 keV (Si Kα) below the parent peak). At energies of above 10 keV the Si escape peak effect can effectively be negligible [15], since the X-ray(s) are more penetrating and hence interact deeper in the material before they undergo photoelectric absorption, hence the SiK X-ray(s) do not come out. For energies below 10 keV, the Si escape peak is removed by the PD-FP method and added back to their parent peak.

Stellenbosch University http://scholar.sun.ac.za

3.3 SUM PEAK REMOVAL

Sum peaks arise from a specific form of peak (pulse) pileup, where two events from high-intensity peaks occur in the pulse processing electronics shortly one after the other, without the pileup inspector recognizing them as two separate events. The signal is thus seen as one and the energy is registered as the sum of the two. Therefore it needs to be removed from the spectra by the PD-FP method.

This can either be for two elements from the same sample or the same elemental peak e.g. Si (K_α of 1.74 KeV) and Al (K_α of 1.487KeV) and hence a peak at 3.23 KeV is detected or the sum of two Si K_α events at (3.48 keV). The sum peaks are unlikely to be identified as a different element, but they may interfere with important lines in the analysis.

The intensity of the sum peak is count rate dependant and an effective way to reduce the effect of the sum peak is to reduce the count rate [15]. Furthermore a short pulse shaping time is important, to optimize the detection pulses which are closely spaced in time.

3.4 BACKGROUND REMOVAL

The detector background is mainly the result of fundamental X-ray and electron-energy loss processes i.e. the coherent and incoherent scattering of the excitation X-ray(s). Other effects contributing to the background are the effects associated with the partial collection or incomplete charge collection, usually producing tailings, which are higher than the expected continuum.

The background removal is done by the peak stripping method, which is based on the removal of rapidly varying structures in a spectrum by comparing the channel content y_i with the channel content of its neighbours [15]:

$$m_i = \frac{y_i + y_{i+1}}{2} \, . \tag{3.3}$$

If y_i is smaller than m_i , the content of channel i is replaced by the mean m_i .By repeating this procedure, the peaks are gradually “stripped” from the spectrum.

The method does however pick up local fluctuations in the continuum, which is caused by the Be window. The Si internal fluorescence peak and absorption edge caused by the dead layer effects can further cause fluctuations in the continuum.

Stellenbosch University http://scholar.sun.ac.za

3.5 BLANK REMOVAL

This method is mainly used for the removal of the Argon (which fluorescence in air) and X-ray tube scattering peaks. This method uses a channel-by-channel subtraction of the blank counts from the corresponding counts in the spectrum. For this method it is assumed that a blank sample is acquired under the same conditions as the normal spectra e.g. live-time, X-ray beam parameters and the spectra is evaluated via all the prior mentioned methods i.e. smoothing, escape peak removal, background removal.

3.6 INTENSITY EXTRACTION

After the spectra processing steps have been carried out, the final step is to extract the net peak intensity. The peak intensity extraction analysis is performed by making use of either the Gaussian deconvolution, integration or reference methods. The Gaussian deconvolution method is used for those elements that have well defined Gaussian shape and make use of linear or nonlinear least square fitting where each peak in the spectrum is fitted with an individual Gaussian distribution. For non-Gaussian fitting the integration or reference methods are used. The integration method determine the peak area by integrated over a certain region of interest (ROI) and the reference method uses stored profiles of each element to fit the peaks.

3.6.1 Gaussian Peak Fitting: Linear Least Square [15]

For the linear least square method only the peak heights can be adjusted during the fitting process. The relative peak heights within a series (e.g. $K_{\alpha1}$, $K_{\alpha2}$, $K_{\beta1}$, $K_{\beta2}$, $K_{\beta3}$ for K-series) are taken from tabulated values and are not allowed to vary during linear fitting. For this method to work properly, the spectrum calibration, detector resolution and efficiency need to be known accurately.

The aim is to obtain optimal values for the parameters of a linear function, by fitting the experimental data with the following linear function

$$y = a_1 X_1 + a_2 X_2 + \cdots + a_m X_m \ . \qquad (3.4)$$

This is called least squares parameter estimate, also called curve fitting.

The optimum set of parameters a_1 , ……a_m that gives a least-squares fit of equation 3.4 are the values that minimize the chi-square (χ^2) function:

$$\chi^2 = \sum_{i=1}^{n} \frac{1}{{\sigma_i}^2} (y_i - a_1 X_1 - a_2 X_2 - \cdots - a_m X_m)^2 \ . \qquad (3.5)$$

Stellenbosch University http://scholar.sun.ac.za

3.6.2 Gaussian Peak Fitting: Non-linear Squares

With the non-linear squares fitting procedure the heights, positions and widths of the peaks in the spectrum are fitted. Since, none of these variables are directly solvable by standard linear least square fitting. A standard nonlinear algorithm is employed namely the Marquardt-Levenberg method, which allows the three parameters for each peak to be adjusted independently. This algorithm is however slower than the linear method, since more fitting needs to be done.

For the general case of least-squares fitting with a function that is nonlinear in one or more of its fitting parameters, no direct solution exists. Therefore the function χ^2 is defined:

$$\chi^2 = \sum_i \frac{1}{\sigma^2{}_i}[y_i - y(x_i, a)]^2 \qquad [15] \qquad (3.6)$$

whose minimum is obtained when the partial derivative with respect to the parameters are zero, generally the Leverberg-Marquardt algorithm is used (a detailed description of the method can be found in Appendix D).

3.6.3 Non-Gaussian Fitting: Integrated [15]

Since the number of counts under the characteristic X-ray peak (after the correction for the continuum has been done) is proportional to the concentration of the analyte, the concentration can therefore be determined by using the integrated method, were the peak area N_{p}, is determined by integrating over a certain ROI.

$$N_p = \sum_{i\,p2}^{ip1}[y_i - y_B(i)] = \sum_i y_i - \sum_i y_B(i) = N_T - N_B \qquad (3.7)$$

where N_T and N_B are the total number of counts of the spectrum and the continuum in the integration window $i_{P1} - i_{P2}$.

3.6.4 Non-Gaussian Fitting: Reference [15]

The reference deconvolution method performs quantitative analysis without obtaining the peak area of the characteristic line, but by using stored profiles for each element to fit the peaks. These stored profiles are obtained by measuring pure elements and applying all the spectra processing steps on the measured pure element. The method is particularly useful in cases where the peak shape deviate substantially from Guassian shapes, usually for low energy peaks.

If a measured spectrum of an unknown sample can be described as a linear combination of spectra of pure elements constituting the sample, then

$$y_i^{mod} = \sum_{j=1}^{m} a_j x_{ji} \qquad (3.8)$$

Stellenbosch University http://scholar.sun.ac.za

With y_i^{mod} the content of channel i in the model spectrum, x_{ji} the content of channel i in the jth reference spectrum and a_j coefficients are a measure of the contribution of pure reference spectra to the unknown spectrum. The value of a_j are obtained via multiple linear least-squared fitting, minimizing the sum of the weighted squared differences between the measured spectrum and the model:

$$\chi^2 = \sum_{i=n_1}^{n_2} \frac{1}{\sigma_i^2} [y_i - y(i)]^2 = \sum_{i=n_1}^{n_2} \frac{1}{\sigma_i^2} [y_i - \sum_{j=1}^{m} a_j x_{ji}]^2 \quad (3.9)$$

with y_i being the channel content, σ_i are the uncertainty of the measured spectrum and n_1 and n_2 are the limits of the fitting region

A measure of the goodness of the fit is given by the reduced χ^2 value:

$$\chi^2 = \frac{1}{(n_2 - n_1 + 1) - m} \chi^2 \quad (3.10)$$

The χ^2 value divided by the number of points in the fit minus the number of reference spectra. A value ~ 1 is seen as a good fit, indicating that the reference spectra are describing the unknown spectrum.

3.7 CONCENTRATION EXTRACTION FOR PD-FP AND IOM-FP METHODS

For the FP method [11,12] the measured emitted intensity as a function of the intensity emitted by the pure analyte, the analyte concentration in the specimen and the ratio of their respective absorption coefficients are given in:

$$P_{i\lambda} = P_{(i)\lambda} C_i \left(\frac{\mu_i^*}{\mu_s^*}\right)_\lambda \qquad [28] \qquad (3.11)$$

where

$P_{i\lambda}$ refer to the theoretically calculated primary fluorescence intensity

$P_{(i)\lambda}$ as above for specimen of pure analyte ‘i’

C_i concentration (weight fraction) of element ‘i’

μ_i^* total effective mass abdorption coefficient for pure analyte ‘i’

μ_s^* total effective mass absorption coefficient for specimen ‘s’

With some mathematics, as can been seen in Appendix E, equation 3.11 can be rewritten in a form where a polychromatic excitation source can be used and where absorption, enhancement and their combined (matrix) effects of multi-element systems are taken into consideration.

Stellenbosch University http://scholar.sun.ac.za

3.8 LIMITATION OF THE SPECTRA EVALUATION AND CONCENTRATION EXTRACTION

No method correct for physical effects such as particle size. The physical effects can be limited by the pellet preparation process. Instrumental effects such as background, overlap and dead time is also not corrected for and must therefore be minimised by the selection of measurement conditions.

For the PD-FP method random and systematic errors exist which have an effect on the precision with which the net peak areas area determined. Random errors are associated with the uncertainty σ_i of the channel content y_i, and systematic error is the discrepancies between the fitting model and the observed data [15].

Furthermore, the PD-FP method cannot measure the concentration of low atomic number elements such as C,O and H, called the balance. The balance cannot be measured due to the high absorption of their low energy X-ray K lines, but it can typically be determined by the intensity ratio of the Compton to Rayleigh (C/R) scatter peaks calibrations, since it is a function of the atomic number of the sample. This low atomic number calibration is however not incorporated in the PD-FP method. The IOM-FP however uses the C/R ratio calibrations extensively to determine the elements in the analysed sample [29,30,31]. The functionality of the method is company propriety information, but it basically uses standards and calculates a least-squares fit to obtain the C/R ratios as a function of atomic number of the material. This approach however does not take into account any no matrix effect, therefore the calibration standards can only be used for the analysis of samples with similar (or identical) matrices e.g. the calibration curve generated with a set of alloys will produce incorrect results when analysing mineralogical samples. Furthermore the inverse overlap matrix approach accelerates the spectrum processing process by assumes a constant ratio for K_α / K_β or L_α / L_β of the peak element. This ratio however varies in certain instances, especially where the absorption edge of one element falls between the K_α and K_β lines of another element.

Many assumptions are made with for the FP method such as, the incident radiation is parallel, the X-ray(s) effectively travel in a straight line within the sample until it is absorbed and the measured fluorescent X-ray(s) exit the specimen at the same angle. These assumptions are however not perfect, but experience have shown that the model performs well in practice.

Stellenbosch University http://scholar.sun.ac.za

CHAPTER 4

XRF TECHNIQUE VALIDATION

The validation of the analytical pXRF technique was done with homogeneous standard reference materials (SRMs) with known composition and concentration, to ensure that the XRF technique is property understood and used. SRMs of nine alloys, three coins and two rock reference material were used. The surfaces of the coins were flattened to ensure that errors resulting from surface roughness can be eliminated. The metal SRM was bought with the Niton XL3t spectrometer from Thermo Scientific. The rock SRMs were supplied by the McGregor Museum in Kimberley and the Central Analytical Facility (CAF) in Stellenbosch.

The SRMs used for validation of the XRF technique where specifically selected to cover a range of atomic numbers (13 to 82) and different combinations of atomic numbers. The SRMs can therefore be divided into three categories: metal alloys, coins and rock standards, as presented in Table 4.1.

All the SRM's have been analysed with the Amptek SDD and the Niton XL3t spectrometers.

Alloys	Coins	Rock
Stainless Steel 410	Nordic gold coin	SARM-48
CDA715	Copper centre coin	SARM-69
Inconel-600	Krugerrand coin	
Ti-CP (Grade 2)		
Stainless Steel 316		
Al 29-4-C		
F-255		
20Cb3		
Brass		

Table 4.1: SRM categories.

Stellenbosch University http://scholar.sun.ac.za

4.1 METAL ALLOY STANDARDS

The results of Stainless Steel 410 [32], CDA715 [33], Inconel-600 [34], Ti-CP (Grade 2) [35] and Brass alloy are presented in Table 4.2 to Table 4.6. The other four SRMs were analysed and presented in Appendix F, since they have similar elemental composition than Stainless Steel 410.

4.1.1 Metal standards results

Elements	Atomic number	Niton XL3t Concentration (wt %)	Amptek Concentration (wt %)	SRM Concentration (wt %)
Ni	28	0.25 ± 0.02	0.19 ± 0.01	0.5 max.
Fe	26	87.08 ± 0.06	85.99 ± 0.25	85 – 88.5
Mn	25	0.48 ± 0.03	0.56 ± 0.02	1.0 max.
Cr	24	12.03 ± 0.02	13.26 ± 0.11	11.5 – 13.5
Other	Low	0.16	-	0.82 max.

Table 4.2: Niton XL3t and Amptek SDD measurements for Stainless Steel 410 [32].

The elemental concentrations for both spectrometers were within the known concentration range as per the SRM certificate of analysis. As discussed in the method limitation section 3.8, the low atomic number elements cannot be determined by the PD-FP method, since the method do not use the Compton to Rayleigh scattering ratio.

Elements	Atomic number	Niton XL3t Concentration (wt %)	Amptek SDD Conctration (wt %)	SRM known concentration (wt %)
Cu	29	68.49 ± 0.06	67.15 ± 0.11	69.5
Ni	28	29.96 ± 0.06	31.27 ± 0.26	29.0 – 33.0
Fe	26	0.58 ± 0.01	0.73 ± 0.03	0.4 – 0.7
Mn	25	0.86 ± 0.01	0.89 ± 0.04	1.0 max.
Other	Low	0.11	-	1.05 max.

Table 4.3: Niton XL3t and Amptek SDD measurements for CDA 715 alloy [33].

Stellenbosch University http://scholar.sun.ac.za

For the CDA715 alloy all the elemental concentrations for both pXRF spectrometers were in concentration range, as defined by the certificate of analysis of the SRM.

Elements	Atomic number	Niton XL3t Concentration (wt %)	Amptek SDD Concentration (wt%)	SRM known concentration (wt %)
Ni	28	74.38 ± 0.061	72.94 ± 0.13	72.0 min.
Fe	26	9.79 ± 0.036	9.75 ± 0.05	6.0 – 10.0
Mn	25	0.29 ± 0.02	0.45 ± 0.01	1.0 max.
Cr	24	14.84 ± 0.04	15.99 ± 0.08	14.0 – 17.0
Other	Low	0.7	-	1.165 max.

Table 4.4: Niton XL3t and Amptek SDD measurements for Inconel-600 alloy [34].

The concentrations of the other elements, such as Ni, Fe, Mn, Cr and Ti were all within the known concentration range, as per the SRM certificate of analysis, for both spectrometers.

The Ti-CP alloy analysed, which is an example of an alloy with one abundant element, Ti and a very low concentration of Fe.

Elements	Atomic number	Niton XL3t Concentration (wt %)	Amptek SDD Concentration (wt%)	SRM known concentration (wt %)
Fe	26	0.14 ± 0.01	0.083 ± 0.02	0 – 0.3
Ti	22	99.83 ± 0.03	99.92 ± 0.62	99.3 – 100
Other	Low	0.03	-	0.4

Table 4.5: Niton XL3t and Amptek SDD measurements for Ti-CP (Grade 2) alloy [35].

Both the elements and their respective concentration values for the Ti-CP alloy were within the known concentration range of the SRM.

Stellenbosch University http://scholar.sun.ac.za

For pXRF measurements an X-ray generator with a maximum energy of 40 keV was used, therefore heavier elements are only detected through their L lines. This makes the spectra analysis more complicated since a variety of lines with different intensities are observed in the spectrum. Therefore the spectrometer will be validated for a few high atomic number elements, such as Pb and Au. Pb being part of the composition of brass were comparatively analysed with the two spectrometers. The Amptek SDD and concentration results are presented in Figure 4.1 and Table 4.6, respectively. The Au concentration in the Krugerrand coin will be analysed in the next section.

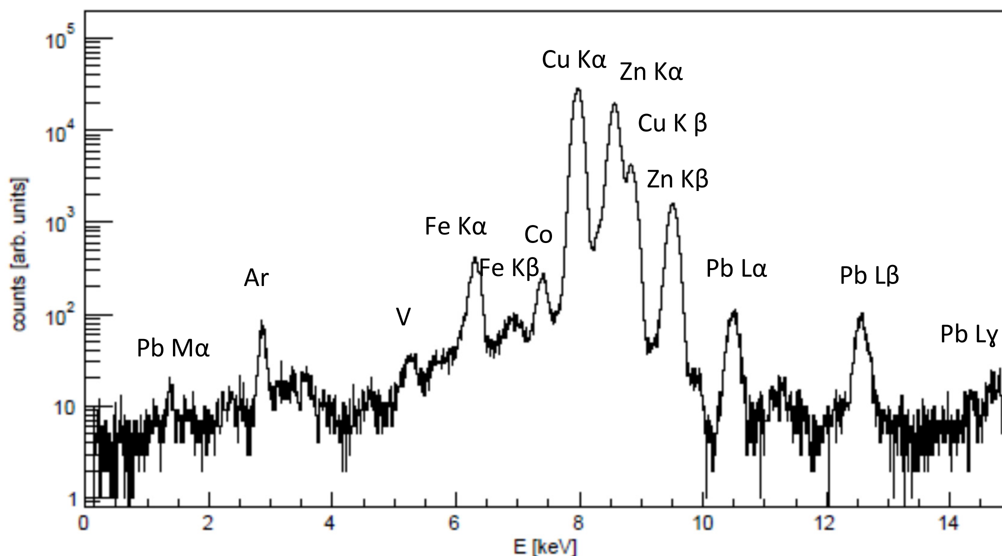

Figure 4.1: Amptek SDD spectrometer spectrum for Brass.

Element	Z number	Niton XL3t concentration (wt %)	Amptek SDD concentration (wt %)
Pb	82	3.09 ± 0.03	3.63 ± 0.12
Zn	30	38.46 ± 0.12	39.39 ± 0.13
Cu	29	57.56 ± 0.15	56.59 ± 0.16
Co	27	0.025 ± 0.008	0.029 ± 0.012
Fe	26	0.31 ± 0.01	0.39 ± 0.01
V	23	0.021 ± 0.001	0.03 ± 0.02
Other	Low	0.53	-

Table 4.6: Brass sample concentration results.

The elemental concentrations of all the elements obtained with both spectrometers are consistent, with a relative low concentration for Pb found. From the results it can be concluded that the concentration extraction by using the excited L lines is effective even though the task is more complex.

Stellenbosch University http://scholar.sun.ac.za

4.2 COIN STANDARDS

The Nordic gold coin and a copper centre coin are 50 euro cents and 2 euros respectively. For both coins only the front surface was prepared by flattening the surface. The back of the coin was also measured, to investigate the effect of surface roughness on elemental concentrations. The elemental concentrations are presented in Table 4.7 and Table 4.8.

The Krugerrand coin was investigated to determine if the concentration of Au can be successfully extracted from the L excitation lines. The measured surface of the Krugerrand coin was not flattened, due to the high monetary value. The elemental concentration for the Krugerrand coin is presented in Table 4.9.

4.2.1 Coin standards results

Element	Z number	Front		Back		Back and Front
		Niton XL3t concentration (wt %)	Amptek SDD Concentration (wt %)	Niton XL3t concentration (wt %)	Amptek SDD Concentration (wt %)	Known concentration (wt %)
Sn	50	0.88 ± 0.01	1.84 ± 0.12	0.87 ± 0.01	1.88 ± 0.16	1.0
Nb	41	0.102 ± 0.002	0.254 ± 0.021	0.126 ± 0.005	0.343 ± 0.010	-
Zr	40	0.096 ± 0.005	0.158 ± 0.016	0.117 ± 0.016	0.141 ± 0.011	-
Zn	30	5.03 ± 0.03	5.46 ± 0.05	5.04 ± 0.03	5.49 ± 0.04	5.0
Cu	29	89.32 ± 0.30	87.67 ± 0.17	88.93 ± 0.32	87.59 ± 0.17	89.0
Fe	26	0.047 ± 0.004	0.061 ± 0.004	0.053 ± 0.012	0.061 ± 0.001	-
Mn	25	0.012 ± 0.005	0.118 ± 0.006	0.035 ± 0.004	0.115 ± 0.003	-
Al	13	4.76 ± 0.35	not determined	5.087 ± 0.34	not determined	5.0
Other	Low	0	-	0.07	-	0.0

Table 4.7: Nordic gold coin concentration results [36].

The elemental concentrations obtained by the Niton XL3t for the Zn, Cu, Al and Sn elements of the Nordic gold coin, were in line with the expected results.

For the Amptek SDD the Al concentration could however not be determined by the PD-FP method, since the histogram bin corresponding to the characteristic x-ray

Stellenbosch University http://scholar.sun.ac.za

energy of Al only contain a few counts as can be seen in Amptek SDD spectrum in Figure 4.2. When analysed by the PD-FP method, it leads to large concentration errors. For the Niton XL3t the Al concentration could be determined, since the IOM-FP method uses the information of the Rayleigh and Scatter peaks intensities to determine the low atomic number concentrations.

There is therefore no means to determine the concentration of Al obtained by the Amptek SDD and hence only the concentrations of Zn, Sn, Cu and a few low concentrations elements could be determined. This can be done by forcing the combined concentrations of Zn, Sn, Cu and the low concentrations elements within the PD-FP code to account for the low atomic number material, such as Al. This can however only be done if the concentration of the low atomic number material is known. In this specific case the assumption is made, since the concentration of the standard is known. The concentrations of the euro coins are available from KME database [36]. From Table 4.7 it can be observed that the elemental concentrations obtained for Zn and Cu are within reasonable values. The forcing of concentration can be seen as a significant weakness of the PD method, used by the Amptek SDD, especially for samples were a large part of the weight percentage is from low atomic number elements.

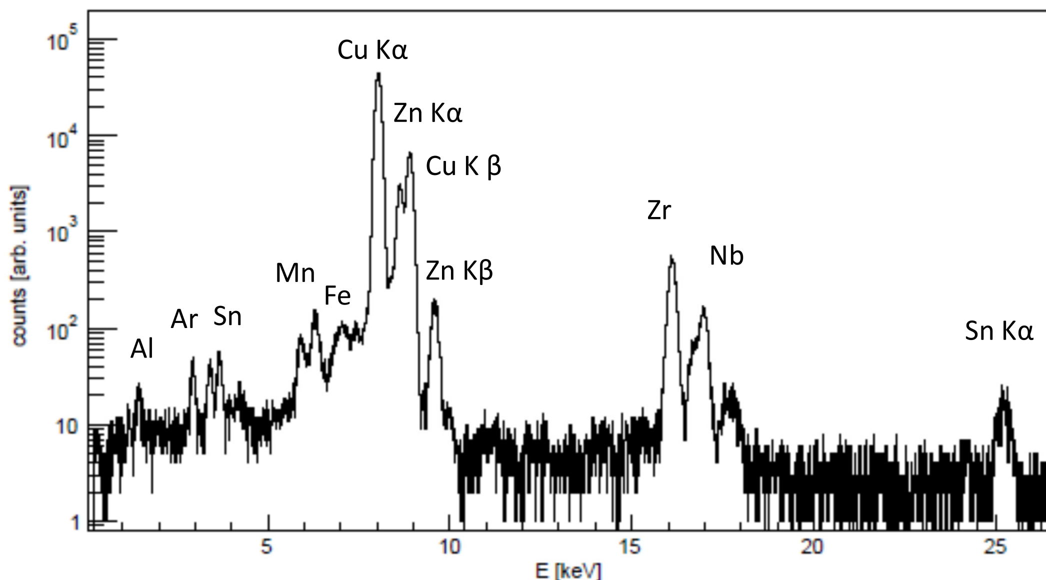

Figure 4.2: Amptek SDD spectrometer spectrum for Nordic gold

By comparing the elemental concentrations of the front of the coin, which is the flattened surface, with the elemental concentrations of the back of the coins; it can be concluded that for pXRF measurements for samples with surface roughness (due to the engraving on the coin) has little to no impact on the elemental concentrations for this coin. The results obtained for the Nordic gold coin were in good agreement

with that of the known elemental concentrations. A few low concentration elements such as Nb, Zr, Fe and Mn were also measured. However, only the high concentration elements were indicated in the certificate.

Element	Z number	Front (flattened surface)		Back		Back and Front
		Niton XL3t concentration (wt %)	Amptek SDD Concentration (wt %)	Niton XL3t concentration (wt %)	Amptek SDD Concentration (wt %)	Known concentration (wt %)
Zn	30	19.75 ± 0.15	20.58 ± 0.10	19.49 ± 0.07	19.41 ± 0.10	20.0
Cu	29	74.98 ± 0.48	73.99 ± 0.18	74.81 ± 0.20	75.29 ± 0.19	75.0
Ni	28	5.14 ± 0.04	5.43 ± 0.03	5.14 ± 0.02	5.29 ± 0.03	5.0
Other	Low	0.13	-	0.56	-	0.0

Table 4.8: Copper coin concentration results.

As in the case of the Nordic gold coin, the elemental concentrations of the back and front of the copper coin compare well, as presented in Table 4.8. Hence there is no need to account for the engraving in the coins, for the conditions where the elemental concentration measurement is performed with PXRF.

The second element used for the validation of the pXRF technique (for high atomic number elements) is Au, as found in the Krugerrand. The Amptek SDD spectrum for the Krugerrand is presented in Figure 4.3.

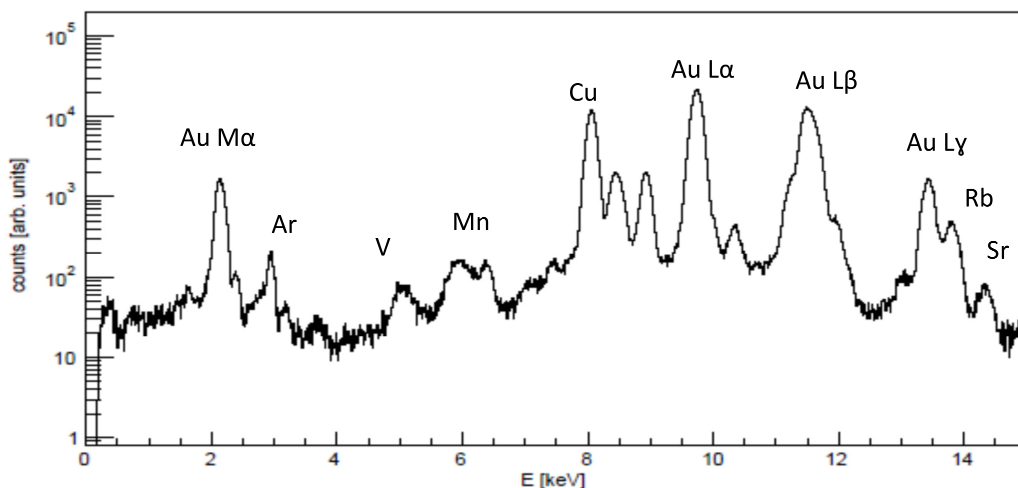

Figure 4.3: Amptek SDD spectrometer spectrum for the Krugerrand coin.

Stellenbosch University http://scholar.sun.ac.za

Element	Z number	Amptek SDD Concentration (wt %)	Known Concentration (wt %)
Au	79	93.21 ± 0.10	91.67
Sr	38	0.072 ± 0.001	-
Rb	37	0.043 ± 0.010	-
Cu	29	6.79 ± 0.03	8.33
Mn	25	0.021 ± 0.001	-
V	23	0.025 ± 0.004	-
Other	Low	-	0.0

Table 4.9: XRF analysis results of the Krugerrand coin [37].

The deviation in the concentration for Au, as found in the elemental concentration results in Table 4.9, is most probably not due to the surface roughness, as concluded from the results of the euro coins. The overlapping of the L_α lines for Au at 9.71 keV and L_β for W at 9.67 keV (originating from the X-ray tube) is the most likely reason. Low concentration elements such as Sr, Rb, Mn and V were also measured. However, only the high concentration elements were indicated in the certificate.

For the most optimal excitation conditions an X-ray tube energy of greater than the K absorption edge is required, which would excite the K_α and K_β lines. Very high energy portable X-ray tubes are nowadays available which can achieve a maximum energy of 100 keV. There is however concerns from a radiation protection point of view, as a result of the high energy.

Stellenbosch University http://scholar.sun.ac.za

4.3 ROCK STANDARDS

Two rock SRMs, SARM-48 [7] and SARM-69 [8] with high SiO_2 content were analysed. The SARM-48 material comes from the Buffalo Mine, South Africa with main compounds such as Al_2O_3, CaO, K_2O and SiO_2. The material was produced in a pellet form by the CAF laboratory at Stellenbosch University. The SARM-69 SRM pellet, which was produced at iThemba Labs, is essentially Late Iron Age pottery vessels remainings found on the Mkgwareng [38] site, with main compounds such as Fe_2O_3, Al_2O_3 and SiO_2.

4.3.1 Rock standard pellet preparation

To ensure homogeneity of the sample the reference material were milled and pressed into a pellet disk.

The homogeneous pellet disk will ensure that reproducible measurements can be obtained. This pellet preparation is done with a press capable of creating a pressure of 20 ton Beckman pressure. The build-up pressure on the sample is initially done over a 30 second period; once the pressure is reached it is maintained for a further 30 seconds period. The pressure on the sample is then decreased to atmospheric pressure over a 30 second period. This method results in a pellet with a smooth surface. The elimination or reduction of the surface contamination was done by cleaning the sample preparation dye with water, acetone and alcohol before each pressing process started.

4.3.2 Rock elemental conversion to oxide

The XRF analysis of oxides is performed in an indirect manner since XRF spectroscopy is only sensitive to elements. Therefore, SiO_2 for example is analysed from the Si element. A conversion factor (as shown in Table 4.10) is used to convert the concentration of the analysed Si K_α elemental line into the oxide form. The conversion factor is the molar ratio of silicon and oxygen in SiO_2. In Table 4.10 all the elements and there major oxide phase in rock art paint are indicated.

Stellenbosch University http://scholar.sun.ac.za

Element	Oxide phase	Conversion factor
Si	SiO_2	2.1393
Ti	TiO_2	1.6681
Al	Al_2O_3	1.8895
K	K_2O	1.2046
Ca	CaO	1.399
Mg	MgO	1.6581
Fe	Fe_2O_3	1.4297
Mn	MnO	1.2912
P	P_2O_5	2.2914

Table 4.10: Stoichiometric factors [39].

4.3.3 Rock standards results

The results for SARM-48 and SARM-69 SRMs obtained by the Niton XL3t and Amptek SDD are presented in Table 4.11 and Table 4.12.

Compounds	Niton XL3t Concentration (wt %)	Amptek SDD Concentration (wt %)	SRM Concentration (wt %)
Fe_2O_3	0.57 ± 0.012	0.31 ± 0.01	0.58
Al_2O_3	9.78 ± 0.14	9.44 ± 0.27	11.24
CaO	7.77 ± 0.12	8.52 ± 0.21	8.90
K_2O	5.79 ± 0.08	4.23 ± 0.11	4.26
SiO_2	72.47 ± 0.43	74.3 ± 3.0	67.11
MgO	0.95 ± 0.36	0.99 ± 0.28	0.18
TiO_2	not detected	not detected	0.10
MnO	not detected	not detected	0.02

Table 4.11: SARM 48 reference material [7].

Stellenbosch University http://scholar.sun.ac.za

Compounds	Niton XL3t Concentration (wt %)	Amptek SDD Concentration (wt %)	SRM (wt %)
Fe_2O_3	7.71 ± 0.04	5.03 ± 0.02	4.76 – 9.8
Al_2O_3	14.40 ± 0.20	18.18 ± 2.04	11.12 – 16.49
CaO	2.23 ± 0.03	2.68 ± 0.04	1.33 – 8.19
K_2O	1.74 ± 0.03	1.83 ± 0.03	1.28 – 2.78
SiO_2	69.78 ± 0.17	70.3 ± 2.3	57.48 – 69.31
MgO	not detected	1.0 ± 1.2	1.14 – 2.68
TiO_2	0.62 ± 0.01	0.72 ± 0.01	0.57 – 1.02
MnO	0.08 ± 0.01	0.12 ± 0.01	0.08 – 0.19
P_2O_5	0.27 ± 0.03	0.27 ± 0.11	0.12 – 0.33

Table 4.12: SARM 69 reference material [8].

From the compound concentration of Table 4.11 and Table 4.12, it can be observed that for the two SRMs the higher atomic number compounds, such as K_2O, CaO and Fe_2O_3 are in good agreement with that of the known SRM concentrations. For the lower atomic number compounds, such as MgO and Al_2O_3 where the concentrations obtained from the two spectrometers are not that reliable due to the high absorption of their low energy X-ray K lines.

For SARM-48 the X-ray lines for the compounds TiO_2 and MnO were not detected by either one the spectrometers. This is due to the very low concentrations.

Stellenbosch University http://scholar.sun.ac.za

4.4 XRF TECHNIQUE VALIDATION CONCLUSIONS

Several homogeneous SRMs were used for the validation of the XRF technique, covering a range of atomic numbers and different combination of atomic numbers. For all the SRMs the elemental concentrations obtained for both the pXRF spectrometers were in good agreement with the known concentrations.

For the coin SRMs the front was prepared by flattening the surface. The back of the coin were also measured to investigate the effect of surface roughness, due to the engraving on the coin, on elemental concentrations. The elemental concentrations of both the back and front, for the two SRMs coins, compared well and therefore there is no need to account for the engraving on coins when elemental concentration measurement is performed. For the Nordic gold coin the very small Al peak detected could not be used to determine the Al concentration. Since the PD method used by the Amptek SDD does not use the C/R calibration to determine the low atomic number concentrations, as in the case with the IOM-FP method used by the Niton XL3t. Therefore only the concentrations of Zn and Cu could be determined. This was done by limiting the combined concentration of Zn and Cu, by assuming the the known concentration of Al from the certificate, and calculating their concentrations respectively. This can be seen as a weakness of the PD method, especially for samples were a large contribution of the weight percentage is from low atomic number elements.

From the two rock SRMs the compound concentrations for the high atomic number compounds are in good agreement with that of the known SRM concentration. However for the low atomic number compounds, such as MgO and Al_2O_3 the concentrations obtained using the two spectrometers are not reliable due to the high absorption of their low energy X-ray K lines.

The Krugerrand coin measured elemental concentrations agreed well the known SRM elemental concentrations, which demonstrate that the extraction of concentrations with the use of L lines is effective, even though the task is more complex. Additionally, the well resolved L X-ray lines by the pXRF detector, between all the other K X-ray lines, play a vital factor to achieve high accuracy results for high atomic number elemental concentrations.

Stellenbosch University http://scholar.sun.ac.za

CHAPTER 5

EXPERIMENTAL RESULTS AND DISCUSSION

5.1 MOUNT AYLIFF ROCK ART FRAGMENT

A rock art fragment from the Mount Ayliff area in Eastern Cape found on the shelter floor of a cave, which had naturally exfoliated from the bigger rock art painting was analysed. The fragment is made of sandstone, which mainly consists of SiO_2. The age of the paint on the fragment is estimated to be about 150 years [40] since scattered remnants of the Bushman still exist in the area. Ten points were specifically selected, as indicated in Figure 5.1 and analysed in order to obtain the compound concentrations of each of the points. The ten points included seven paint points covering a variety of paint colours, two rock varnish points and the back of the rock. The paint colours ranged from black, shades of brown and shades of red, where the black paint is due to manganese or charcoal, the red colour is due to iron oxide and the red-brown colour is due to Hematite (a type of ferrous oxide) [1].

The measurements were performed in consultation with Dr L. Jacobson, the former Deputy Director of the McGregor Museum in Kimberley.

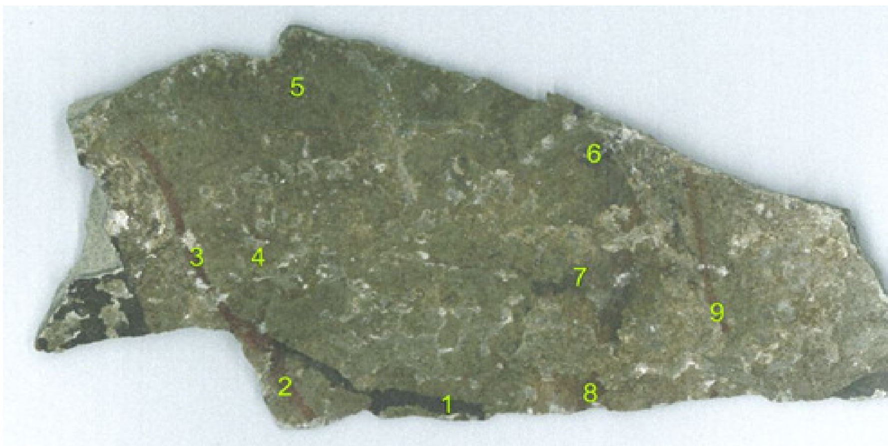

Figure 5.1: Mount Ayliff rock art fragment with the points that were characterised.

For the analysis, the assumption was made that the rock art fragment consists of one layer of infinite thickness. Five measurements (obtained by means of the Amptek SDD and the Niton XL3t spectrometers) were taken at each of the ten points to improve the statistics and also to avoid anomalies because of grain effects. The composition analyses are shown in Table 5.1 and Table 5.2 and the Amptek SDD spectrometer spectrum in Figure 5.2.

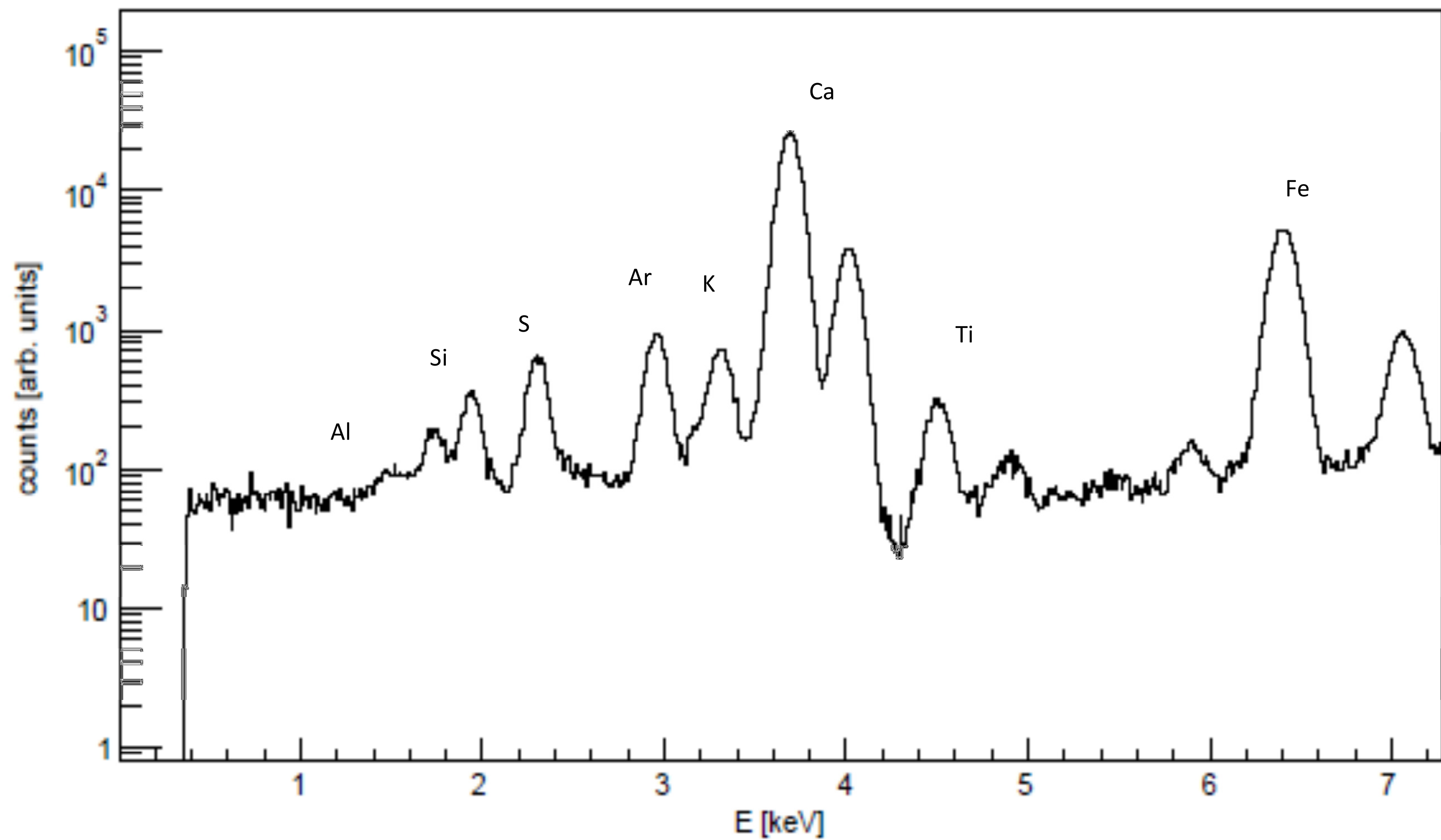

Figure 5.2: Amptek SDD spectrometer spectrum for the Mount Ayliff rock art fragment (point 1).

5.1.1 Compound concentrations and conclusions

Compounds		Al_2O_3	SiO_2	P_2O_5	S	K_2O	CaO	TiO_2	Fe_2O_3
Concentration		wt %	wt %	wt %	wt %	wt %	wt %	wt %	wt %
Point 1 Black	Niton XL3t	0.71 ± 0.11	7.88 ± 0.08	< 0.01	6.89 ± 0.05	0.36 ± 0.01	40.69 ± 0.09	< 0.01	0.78 ± 0.01
	Amptek SDD	not determined	not determined	0.547 ± 0.082	8.338 ± 0.237	1.416 ± 0.015	44.566 ± 0.166	0.699 ± 0.019	2.744 ± 0.019
Point 2 Red/Brown	Niton XL3t	0.89 ± 0.12	11.29 ± 0.09	< 0.01	6.99 ± 0.06	0.38 ± 0.01	35.19 ± 0.08	< 0.01	0.76 ± 0.01
	Amptek SDD	not determined	not determined	0.724 ± 0.081	9.997 ± 0.206	0.929 ± 0.026	41.992 ± 0.137	0.354 ± 0.011	2.424 ± 0.015
Point 3 Red/Brown	Niton XL3t	2.11 ± 0.10	17.91 ± 0.11	< 0.01	9.19 ± 0.06	0.74 ± 0.02	32.29 ± 0.08	< 0.01	1.08 ± 0.02
	Amptek SDD	not determined	not determined	1.317 ± 0.111	10.478 ± 0.198	0.739 ± 0.024	28.796 ± 0.113	0.229 ± 0.008	1.742 ± 0.011
Point 4 Varnish	Niton XL3t	2.17 ± 0.14	13.86 ± 0.10	< 0.01	9.37 ± 0.06	0.56 ± 0.02	36.88 ± 0.08	< 0.01	0.94 ± 0.01
	Amptek SDD	not determined	not determined	0.888 ± 0.07	8.230 ± 0.200	0.792 ± 0.021	34.024 ± 0.018	0.327 ± 0.010	3.439 ± 0.016
Point 5 Varnish	Niton XL3t	1.75 ± 0.01	11.89 ± 0.10	< 0.01	9.19 ± 0.07	0.38 ± 0.01	41.85 ± 0.09	< 0.01	0.97 ± 0.02
	Amptek SDD	not determined	not determined	1.718 ± 0.116	6.919 ± 0.116	0.889 ± 0.023	36.112 ± 0.111	0.350 ± 0.010	1.821 ± 0.011

Table 5.1: Compound and element concentration of measured points 1 to 5 for both the Niton XL3t and Amptek SDD spectrometers.

Compounds			Al_2O_3	SiO_2	P_2O_5	S	K_2O	CaO	TiO_2	Fe_2O_3
Concentration			**wt %**	**wt %**	**wt %**	**wt %**	**wt %**	**wt %**	**wt %**	**wt %**
Point 6	Black	Niton XL3t	1.65 ± 0.15	11.89 ± 0.09	< 0.01	9.01 ± 0.08	0.36 ± 0.01	45.79 ± 0.11	< 0.01	0.73 ± 0.01
		Amptek SDD	not determined	not determined	2.016 ± 0.013	12.360 ± 0.317	1.13 ± 0.011	37.275 ± 0.171	0.419 ± 0.015	2.728 ± 0.022
Point 7	Black	Niton XL3t	1.59 ± 0.15	13.43 ± 0.11	< 0.01	10.39 ± 0.07	0.41 ± 0.01	41.11 ± 0.09	< 0.01	0.88 ± 0.01
		Amptek SDD	not determined	not determined	0.599 ± 0.08	10.184 ± 0.133	1.080 ± 0.031	38.705 ± 0.104	0.338 ± 0.012	1.904 ± 0.004
Point 8	Red / Brown	Niton XL3t	0.21 ± 0.11	22.63 ± 0.13	< 0.01	11.88 ± 0.08	0.96 ± 0.02	31.08 ± 0.08	< 0.01	1.18 ± 0.01
		Amptek SDD	not determined	not determined	1.033 ± 0.032	9.478 ± 0.206	0.865 ± 0.024	31.652 ± 0.110	0.219 ± 0.008	1.854 ± 0.011
Point 9	Red / Brown	Niton XL3t	0.15 ± 0.15	14.68 ± 0.11	< 0.01	9.59 ± 0.07	0.39 ± 0.01	40.79 ± 0.09	< 0.01	0.66 ± 0.01
		Amptek SDD	not determined	not determined	0.436 ± 0.011	8.864 ± 0.024	1.026 ± 0.026	38.860 ± 0.120	0.465 ± 0.060	1.830 ± 0.012
Back of rock		Niton XL3t	2.39 ± 0.09	23.58 ± 0.38	< 0.01	not determined	1.29 ± 0.07	13.82 ± 0.12	< 0.01	1.75 ± 0.02
		Amptek SDD	not determined	not determined	0.377 ± 0.072	0.157 ± 0.033	2.437 ± 0.032	9.250 ±0.050	1.020 ± 0.014	3.589 ± 0.013

Table 5.2: Compound and element concentration of measured points 6 to 9 and back of the rock, for both the Niton XL3t and Amptek SDD spectrometers.

Stellenbosch University http://scholar.sun.ac.za

The elemental concentrations of the low atomic number compounds Al_2O_3 and Si_2O could not be determined by the Amptek SDD PD-FP method, since the PD-FP method does not use the C/R calibrations to determine low energy compounds. When the small Si peak in the Figure 5.2 is analysed with the PD-FP method, it leads to a large concentration error. This is a similar situation as previously encountered with the Al concentration for the Nordic gold coin analysis, where a limiting concentration value was used in the PD-FP code for Zn, Sn, Cu and low concentration elements. A similar approach is used for the low compound and elemental concentrations Al_2O_3 and SiO_2 of the Mount Ayliff fragment. In order to compare the concentration of the high atomic number compounds P_2O_5, S, K_2O, CaO, TiO_2 and Fe_2O_3 the assumption is made that the balance and the concentrations of Al_2O_3 and SiO_2 for the Niton XL3t is correct and used in an attempt to obtain the elemental analysis with the PD-FP method.

From the compound concentrations in Table 5.1 and Table 5.2 it can be seen that the total compound concentration contribution adds up to less than 100 wt %. The difference or balance is as of a result of elements which cannot be detected such as H, Na and C (from organic matter) due to the high absorption of their low X-ray energy in the material. The determination of the balance by the IOM-FP method (used by the Niton XL3t) is propriety information, but it is likely that a similar method is used as with the determination of low atomic compound concentrations i.e. where the information of the Rayleigh and Scatter peaks are used. This ability to calculate the low atomic number compounds with the IOM-FP method makes it a superior technique to the PD-FP method, used by the Amptek SDD.

The concentrations of P_2O_5 and TiO_2 compounds obtained with the Amptek SDD were much higher than the concentrations obtained with the Niton XL3t. Since these two compound are on the lower (Z = 15 for P) and higher (Z = 22 for Ti) atomic number compounds range (15 to 26) measured with the Amptek SDD, it is speculated that the PD-FP method used by the Amptek SDD do not produce accurate concentrations at the limits of the atomic number ranged measured.

From the results it can be concluded that a uniform coating of high Ca and Si concentrations is spread across the fragment. Silica rich deposits commonly known as amorphous silica skins [41] have been observed for certain rock art sites [41]. The deposits are commonly in the order of ≤ 0.5 mm thick, but can be up to 3 mm. The mechanism of silica skin formation is however complex, but in the studies carried by Lovering [42] and Watchman [43] for rock art sites throughout Australia, it was concluded that the coating formation is due to the slow percolation of ground-waters through the sandstones. The typical yearly rainfall for the Mount Ayliff region in the Eastern Cape is about 672 mm per year [44], with leachable elements such as Mg, K, Ca, Fe and to a lesser extend Al, Si and Mn [1] forming the major constituents of the layer. The leach of CaO and Si_2O from the back to the front of the rock is illustrated in Figure 5.3, where the points with the same colour were combined to

obtain an average concentration for each colour. The weathering processes the account for the account for the extensive removal of the relative mobile elements, such as Mg, K, Ca and Fe. It appears that this removal process did not happen for the Mount Ayliff rock fragment, since high CaO concentration was detected. Weathering processes is complex and depends on many environmental factors and the material properties of the rock itself [45], such as crystal structure [46], which result in compositional segregation at the sample surface [47,48,49,50].

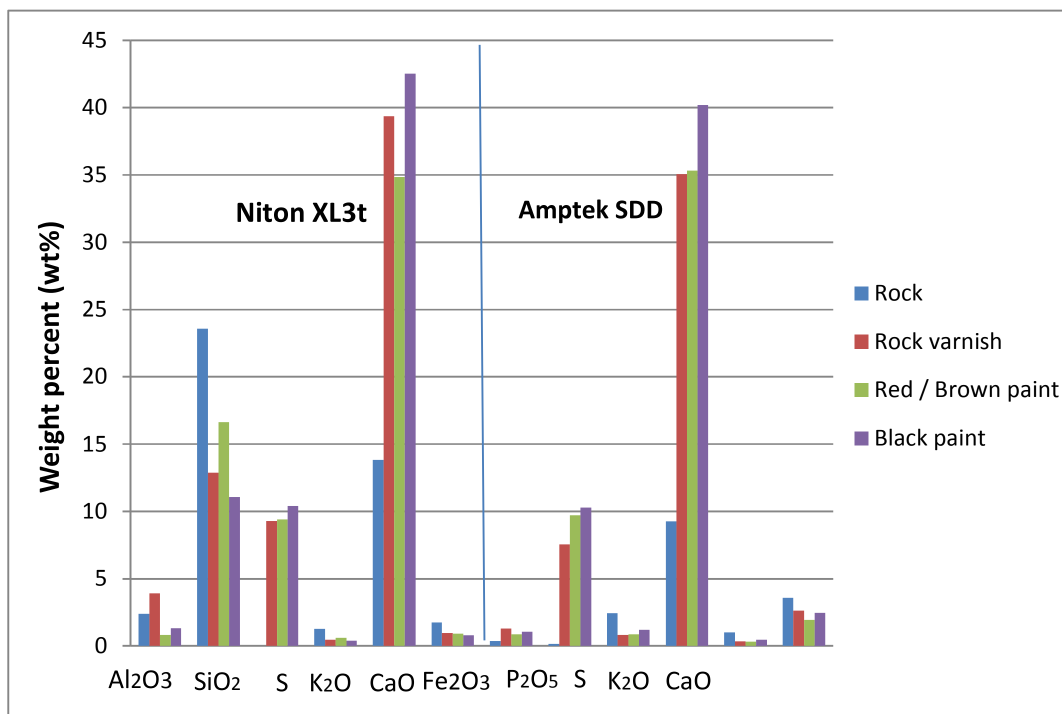

Figure 5.3: Elemental compositions by colour and back of the rock

The occurrence of a uniform CaO layer over the rock art was however unexpected. It was expected that the composition would vary for different colours e.g. the red paint lines have a high concentration of iron oxide (Fe_2O_3).

The graphical illustrations of the low and high compound concentrations for the Niton XL3t are shown in Figure 5.4 and 5.5, Amptek SDD concentrations in Figure 5.6 and 5.7. The concentration of P_2O_5 and TiO_2 for the Niton XL3t is not included since the concentrations obtained from the Niton XL3t were all below 0.01 weight percent.

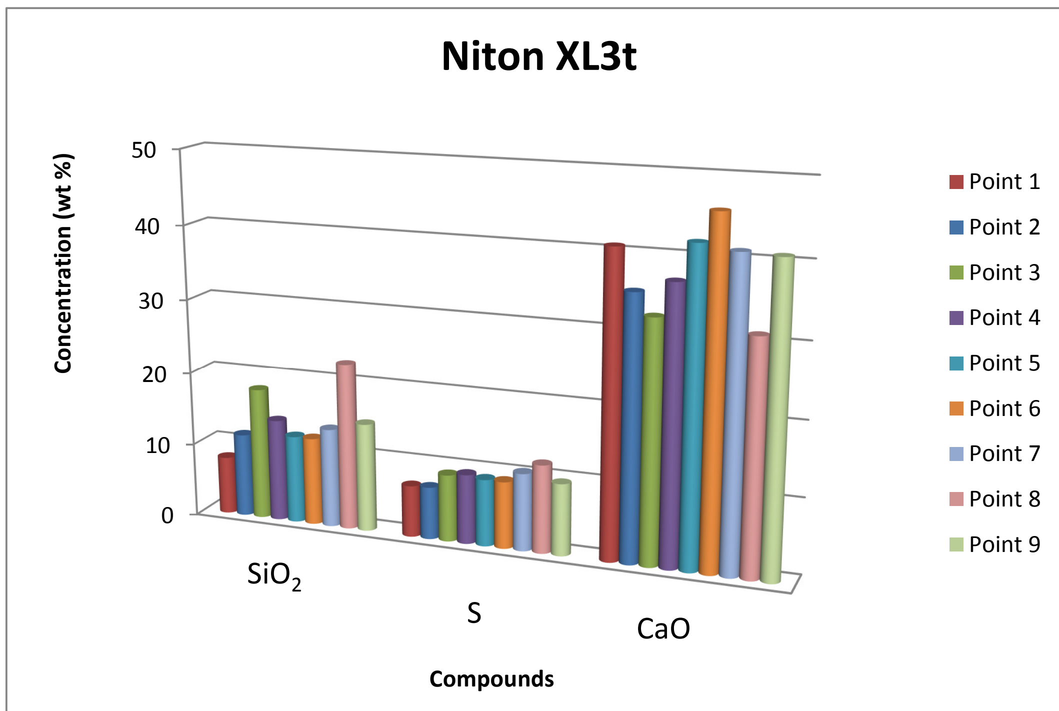

Figure 5.4: Compound and elemental concentrations (wt %) per point for the Niton XL3t spectrometer.

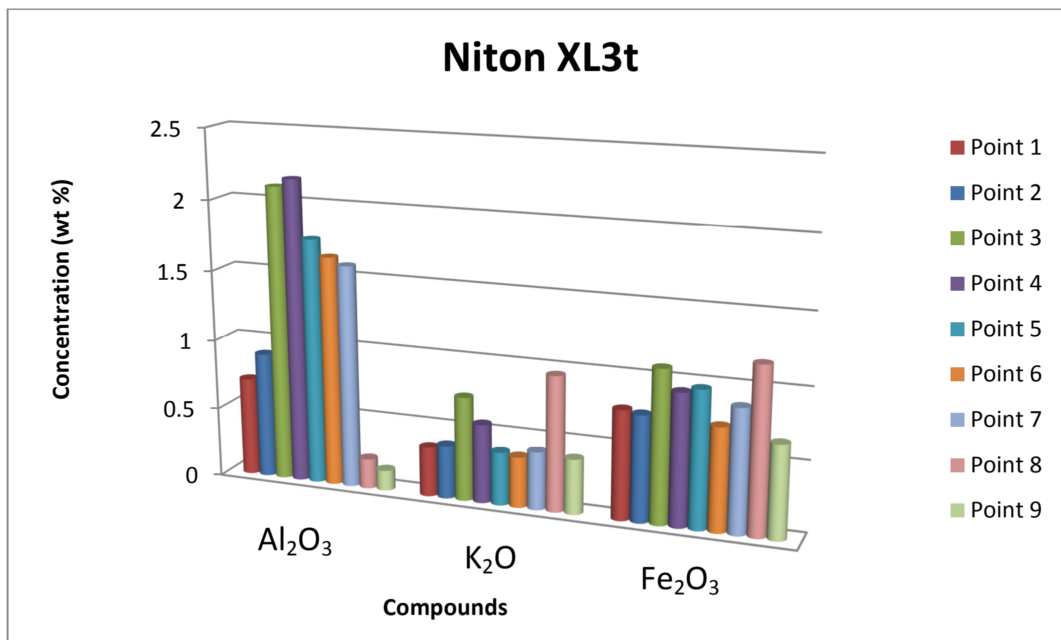

Figure 5.5: Compound and elemental concentration (wt %) per point for the Niton XL3t spectrometer.

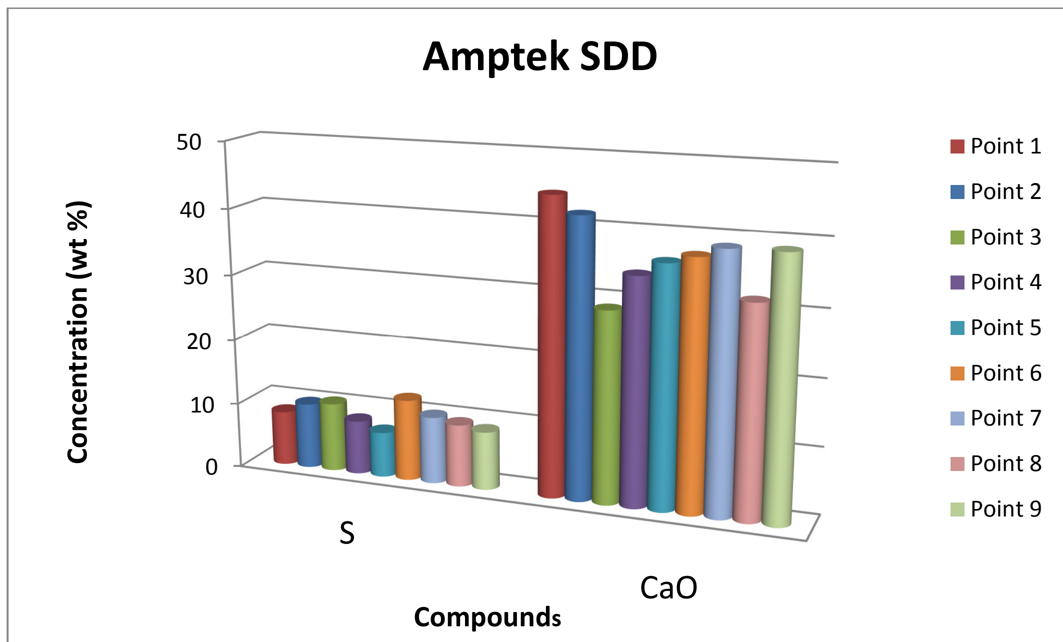

Figure 5.6: Compound and elemental concentration (wt %) per point for the Amptek SDD spectrometer.

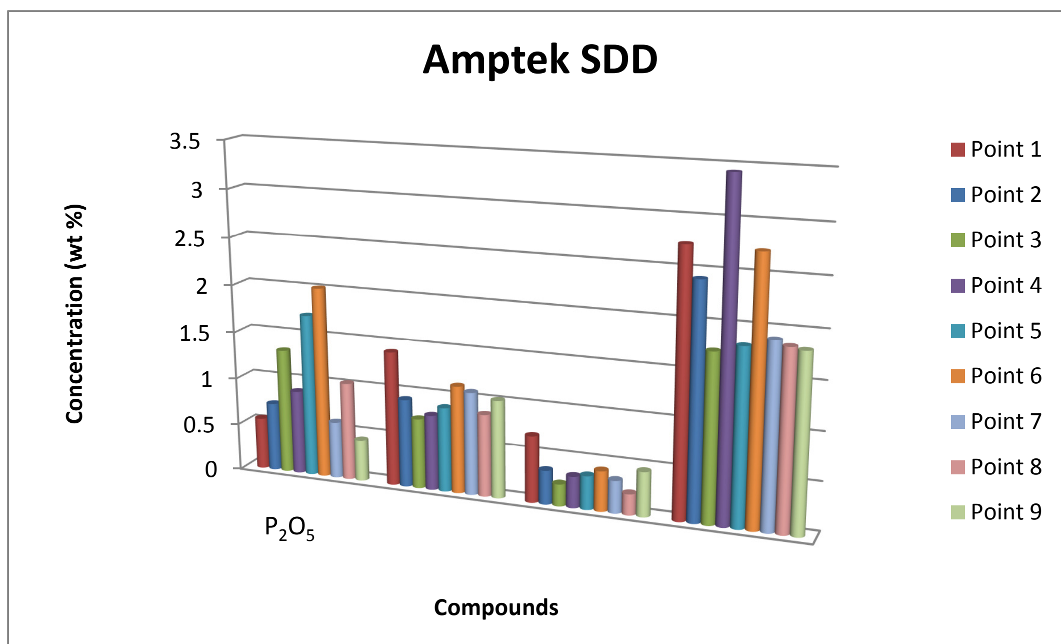

Figure 5.7: Compound and elemental concentration (wt %) per point for the Amptek SDD spectrometer.

Stellenbosch University http://scholar.sun.ac.za

5.1.2 Semi-quantitative comparison of the two pXRF spectrometers

For pXRF spectrometer comparison purposes, the compound ratio value which is determined by dividing the Amptek SDD measured concentration by the measured concentration value of the Niton XL3t spectrometer, for each point is calculated. With the concentration ratios determined for S, K_2O, CaO and Fe_2O_3 compounds and presented in Table 5.3. Since the concentrations of P_2O_5 and TiO_2 for Niton XL3t were all given below 0.01, the concentration ratios were not calculated. The compound ratio serves as a means to do a semi-quantitative comparison of the two pXRF spectrometers. Graphic illustrations of the compound ratio values are presented in Appendix G.

Element	Point Description	S	K_2O	CaO	Fe_2O_3
Point 1	Black	1.21	3.93	1.10	3.52
Point 2	Red / Brown	1.43	2.44	1.19	3.19
Point 3	Red / Brown	1.14	1.00	0.89	1.61
Point 4	Varnish	0.88	1.41	0.92	3.66
Point 5	Varnish	0.75	2.34	0.86	1.88
Point 6	Black	1.37	3.14	0.81	3.74
Point 7	Black	0.98	2.63	0.94	2.16
Point 8	Red / Brown	0.80	0.90	1.02	1.57
Pont 9	Red / Brown	0.92	2.63	0.95	2.77
Average		1.05	2.27	0.97	2.68
Standard Deviation		0.25	1.00	0.12	0.89

Table 5.3: Amptek SDD and Niton XL3t compound concentration ratio analysis for S, K_2O, CaO and Fe_2O_3.

Even though the ratio value could give some insight in the agreement between the two spectrometers it should not be seen as an absolute were a ratio value of 1 is good agreement and were any ratio greater or less than 1 is not such good agreement. Since it should be taken into account that the concentrations for the Amptek SDD were forced. However limited comparison can be done and with success for S and CaO compounds, were the average ratio value is approximately 1. It is speculated that the variation for K_2O and Fe_2O_3 compound concentrations between the two spectrometers are due to spectra evaluation code inaccuracies for the heavy Fe (Z=26) compound and light compound K (Z=19) compound.

Stellenbosch University http://scholar.sun.ac.za

5.2 HA KHOTSO ROCK ART FRAGMENT

The rock art fragment in Figure 5.8 was found in cave Ha Khotso in Lesotho. This is a huge and lengthy shelter with some of the finest rock art in southern Africa. The cave includes animals painting such as eland, hartebeest, lion, leopard, buck and guinea fowl. In between these are hunters, dancers and figures of huts - all of which is done in beautiful styles of red, black and brown shades. The rock fragment analysed was naturally exfoliated from a larger rock art painting. The fragment is made of sandstone and its dimensions are about 9 cm^2. The colour of the paint on the rock fragment can be described as a combination of white and yellow i.e. a cream colour which is covered across the fragment. The Ha Khotso fragment was analysed by making use of both the pXRF and PIXE [5] techniques, with the area measured five times. For pXRF, the Amptek SDD with miniature X-ray generator and for micro-PIXE, the facility at iThemba LABS were used.

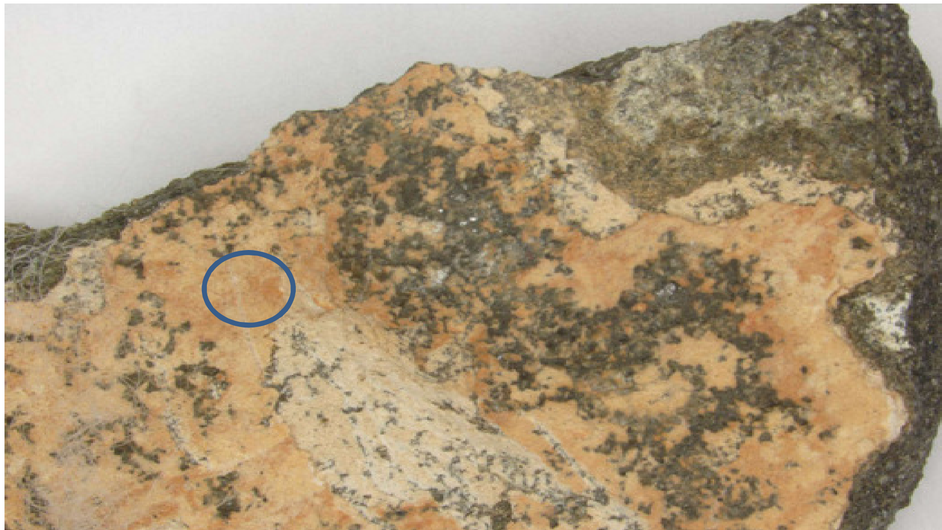

Figure 5.8: Ha Khotso rock fragment, with analysed section indicated with a blue circle.

The Ha Khotso elemental concentrations obtained by PIXE and XRF techniques are given in Table 5.4 and the Amptek SDD spectrometer spectrum in Figure 5.9.

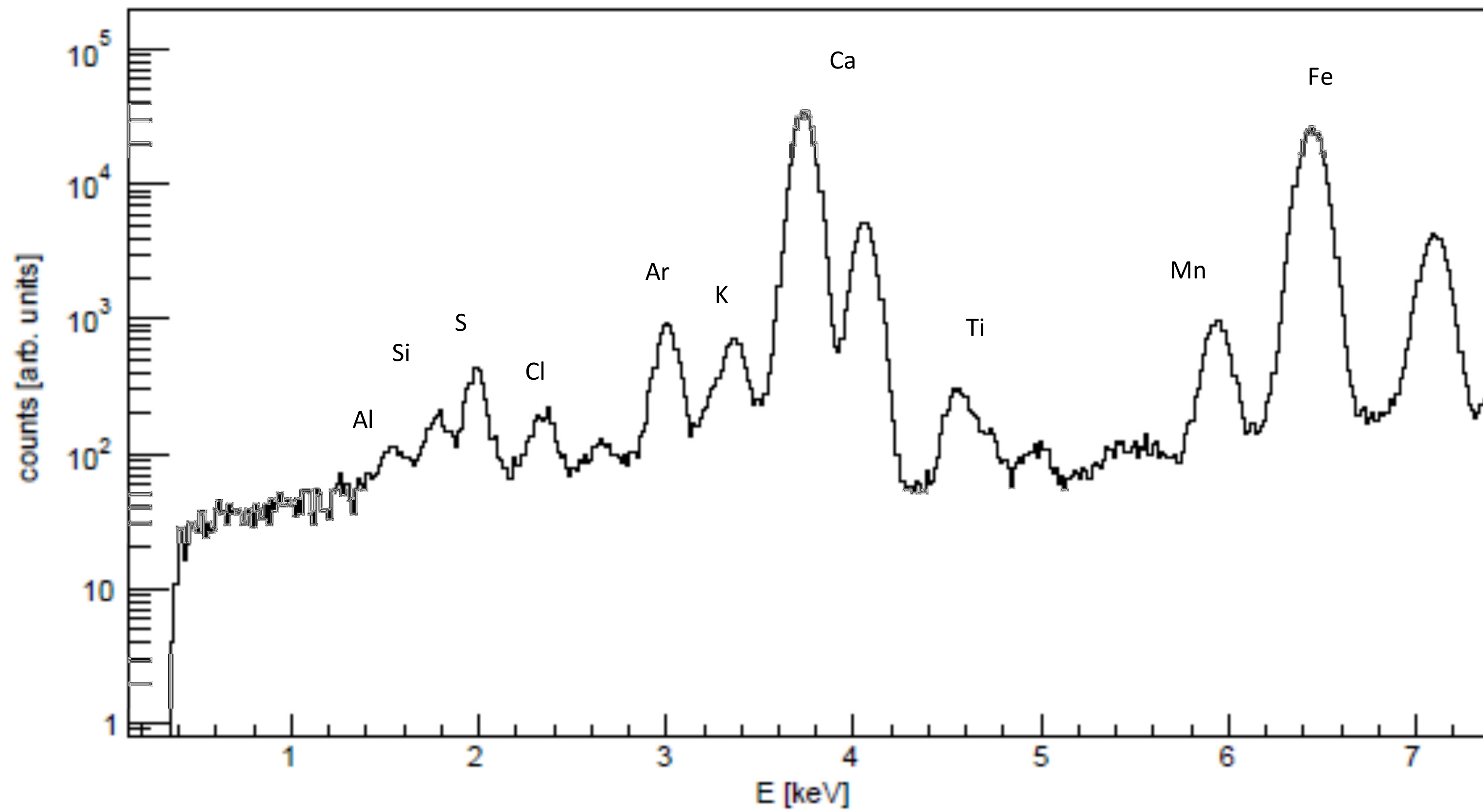

Figure 5.9: Amptek SDD spectrometer spectrum for the front of the Ha Khotso rock fragment**.**

5.2.1 Compound concentrations and conclusions

Compounds		Na_2O	MgO	Al_2O_3	SiO_2	S	Cl	K_2O	CaO	TiO_2	MnO	Fe_2O_3
Concentration		**wt %**	**wt %**	**wt %**	**wt %**	**wt %**	**wt %**	**wt %**	**wt %**	**wt %**	**wt %**	**wt %**
Rock paint (Front of rock)	PIXE	12.71 ± 0.23	3.41 ± 0.04	9.58 ± 0.03	28.29 ± 0.16	12.92 ± 0.07	0.31 ± 0.09	1.31 ± 0.02	28.71 ± 0.33	0.16 ± 0.01	0.15 ± 0.09	1.67 ± 0.03
	Amptek SDD	not determined	not determined	not determined	31.860 ± 1.60	25.921 ± 0.311	0.571 ± 0.069	0.542 ± 0.041	11.239 ± 0.123	0.117 ± 0.009	0.211 ± 0.011	3.854 ± 0.027
Back of rock	PIXE	not determined	1.37 ± 0.04	12.66 ± 0.14	50.84 ± 0.19	18.37 ± 0.15	0.27 ± 0.07	0.91 ± 0.07	13.93 ± 0.05	0.30 ± 0.02	0.41 ± 0.07	0.90 ± 0.01
	Amptek SDD	not determined	not determined	not determined	51.4 ± 2.3	12.897 ± 0.270	0.697 ± 0.077	0.881 ± 0.061	8.524 ± 0.122	0.563 ± 0.023	0.711 ± 0.011	10.98 ± 0.04

Table 5.4: PIXE and Amptek SDD results for Ha Khotso rock art fragment.

Stellenbosch University http://scholar.sun.ac.za

The graphical illustrations of the compound concentrations for the PIXE and the Amptek SDD spectrometer are presented in Figure 5.10 and Figure 5.11, respectively.

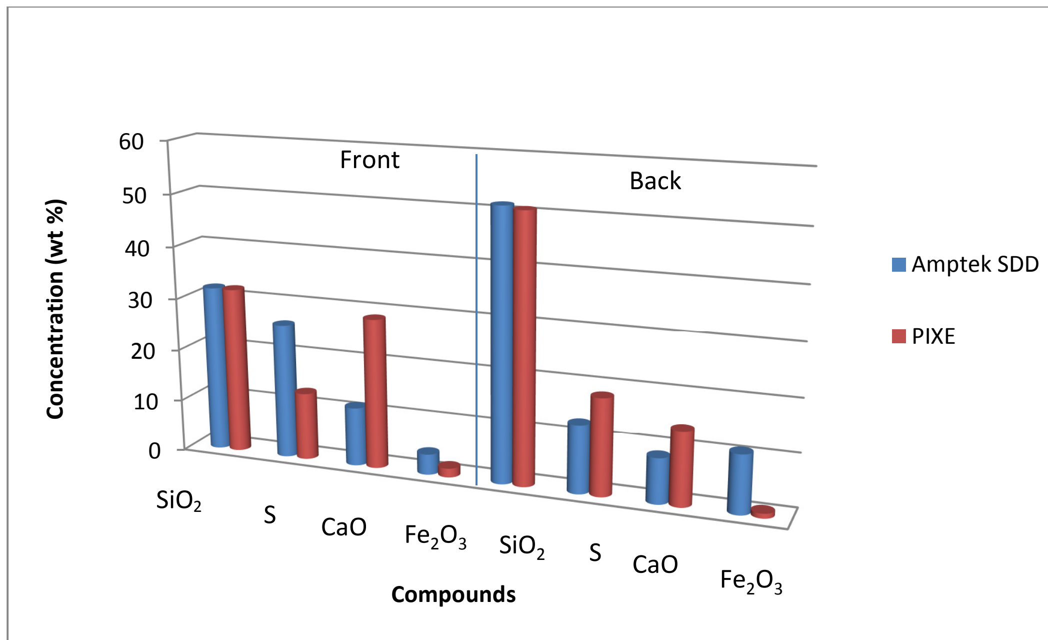

Figure 5.10: SiO_2, S, CaO and Fe_2O_3 concentration measurements with the Amptek SDD and PIXE for the front and back of the Ha Khotso fragment.

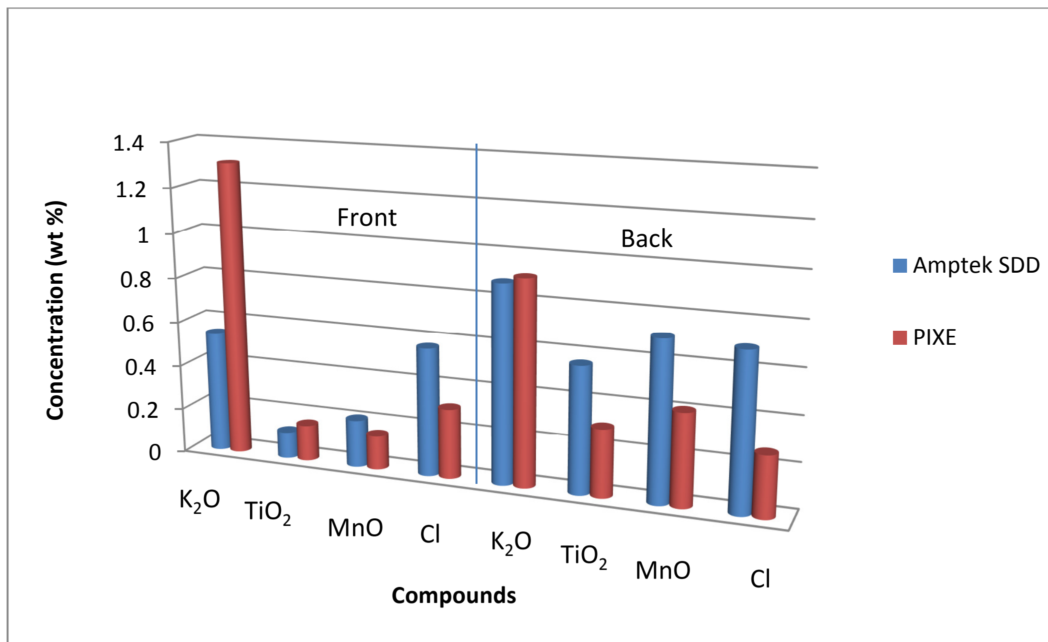

Figure 5.11: K_2O, TiO_2, MnO and Cl concentration measurements with the Amptek SDD and PIXE for the front and back of the Ha Khotso fragment.

Stellenbosch University http://scholar.sun.ac.za

By comparing the CaO compound concentrations for the back and front of the rock (for both techniques) a reduction in the compound concentration can be observed from the front to back of the rock. Therefore the contribution of CaO is a result of the paint on the Ha Khotso rock fragment. The cream colour of the paint, as can be seen from Figure 5.8, can thus be correlated to CaO concentration.

The concentration for Na_2O, MgO and Al_2O_3 could not be determined by the Amptek SDD. From Figure 5.9 it can be seen that Na and Mg was not detected and for Al only a small peak can be observed, which when analysed with the PD-FP method, leads to big concentration errors.

The Si_2O concentrations from the sandstone rock, compared well for the two techniques. However several differences in compound concentration for the two techniques were observed. These differences can be attributed to the fact that the paint on the fragment is most probably layered and heterogeneous, with the surface composition having a different composition than the bulk sample. Therefore the variation in penetration depth due to the difference in energy with which the sample is bombarded for the two techniques, will result in different compound concentrations.

Another factor, which could contribute to differences in compound concentrations of the two techniques, is the distribution of the elements in the analysed region, together with the difference in spectrometer collimation, 3x3 μm^2 and 7 mm^2 for the micro-PIXE and Amptek SDD respectively. Therefore the distribution of the elements (in the analysis area) were analysed with the micro-PIXE technique. For the larger beam spot size the measurement will consist of both rock and rock varnish, since the paint lines are very thin. For the small beam spot size the probability of hitting a sample grain will increase; which could introduce anomalous concentrations and therefore not be a true representation of the sample.

5.2.2 PIXE elemental distribution map

Elemental mapping was performed using the Dynamic Analysis [51,52,53] method, which generate elemental images using K,L and M X-ray lines. The maps are overlap resolve and background subtracted, with the elements concentration expressed in weigh percentage. The elemental maps of the two major elements found in the rock paint Si and Ca are presented in Figure 5.12 and Figure 5.13. The elemental maps of the other elements found in the rock paint can be seen in Appendix H.

Stellenbosch University http://scholar.sun.ac.za

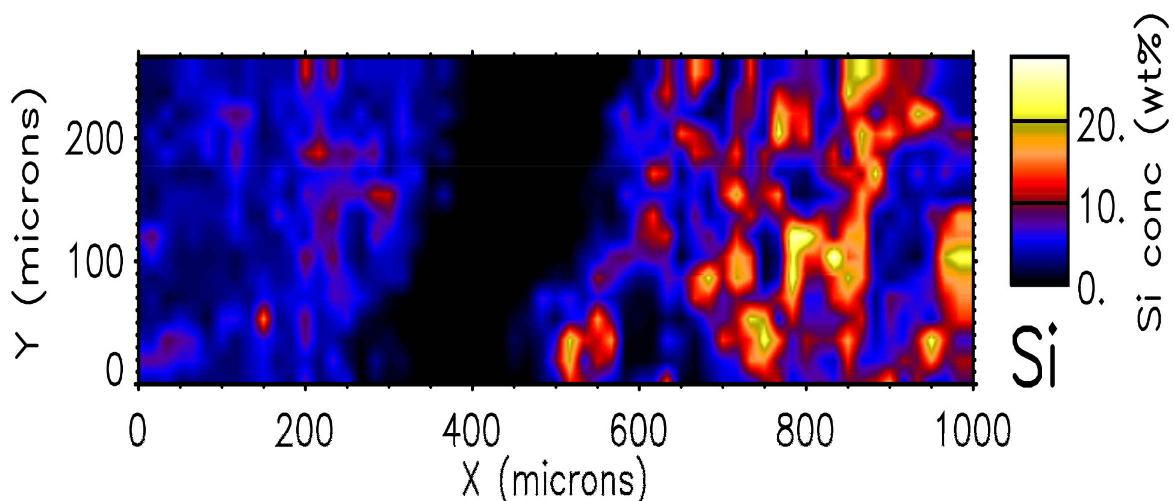

Figure 5.12: Si PIXE elemental composition map for the front of the rock.

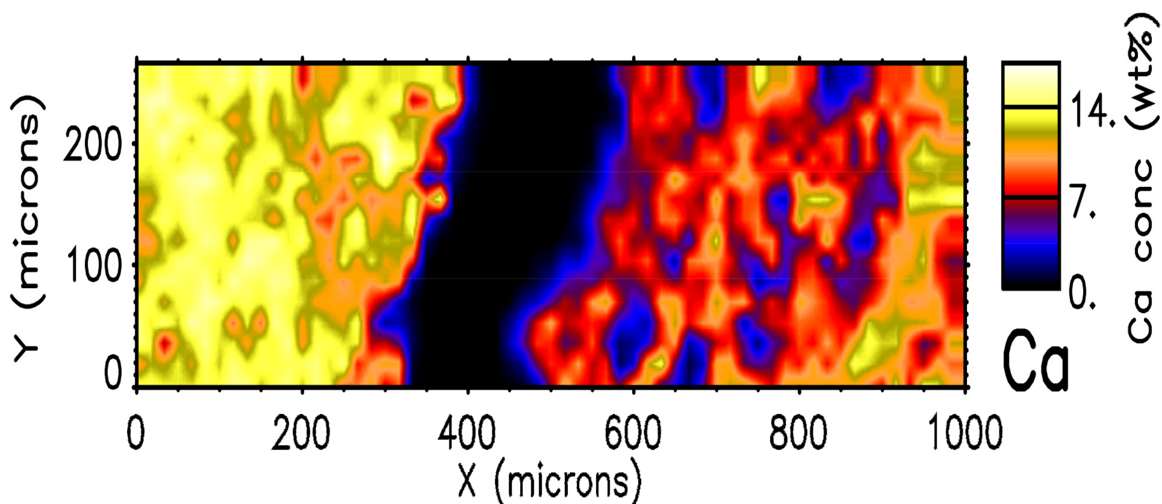

Figure 5.13: PIXE element (Ca) composition map for the front of the rock.

From both PIXE elemental maps (1000x250 µm^2 area) in Figure 5.12 and Figure 5.13 the non-uniform distribution of the elements can be seen. This can definitely result in differences in the compound concentrations for the two techniques. The rock art paint is typically inhomogeneous and includes cracks, as demonstrated by the dark area in the centre of the PIXE elemental maps, which typically occur when the rock art has been exposed to environmental weathering for long periods of time (typically hundreds of years).

Stellenbosch University http://scholar.sun.ac.za

Since the Amptek SDD spectrometer is collimated to 7 mm^2, the compound concentrations obtained is essentially a bulk analysis, where the elemental characterisation is an average of the entire sample volume.

5.3 ROCK ART PAINT THICKNESS PROPERTIES

Even though determination of the thickness of the paint and critical penetration depth was not part of the objective of the study, estimates of the thickness for rock art paint was done by J. Huntley with a scanning electron microscopy (SEM), showing that the thickness can be up to 50 µm [54]. This was measured for the rock art pigment from the Sydney Basin, which are comparable to the Mount Ayliff and Ha Khotso sandstone fragments analysed. The critical depth, beyond which any emitted photon is essentially absorbed and not detected, for light elements such as potassium, calcium, titanium and iron in silicate rock (representation of sandstone rock) is estimated to be 30 µm, 35 µm, 50 µm and 170 µm respectively. Since the detection volume is cone shaped, about half of the contribution of bulk chemical composition is derived from about 5 µm, 5 µm, 7.5 µm and 50 µm, respectively and for silicon the penetration depth is estimated to be ~10 µm [55].

5.4 EXPERIMENTAL RESULT CONCLUSIONS

Not all the low atomic number compound concentrations could be determined by the PD-FP method used by the Amptek SDD. However the higher atomic number compound concentrations could be obtained, by forcing the combined concentrations of the high atomic number compounds within the PD-FP code. This can however only be done if the concentrations of these compounds is known. In the case of the Mount Ayliff and Ha Khotso fragment this assumption were made, since the concentrations are obtained from the Niton XL3t.

From the results of the Mount Ayliff fragment concluded that a uniform coating of high Ca and Si concentrations is spread across the fragment, commonly known as amorphous silica skins (hydrated amorphous silicon dioxide, $SiO_2.nH_2O$). The mechanism for formation is complex, but it can be concluded that the coating is formed due to the slow percolation of ground-waters through the orthoquartzites, with leachable elements such as Mg, K, Ca, Fe and to a lesser extend Al, Si and Mn [1] forming the major constituents of the layer. Weathering processes then account for the removal of the relative mobile elements, such as Mg, K, Ca and Fe. It appears that this removal process did not yet occur for the Mount Ayliff rock fragment, since high Ca concentration was detected. The occurrence of this layer over the rock art was however unexpected. It was expected that the composition

Stellenbosch University http://scholar.sun.ac.za

would vary for different colours. The spectrometer compound concentration ratios for S and CaO were consistent throughout the analysed points. However, large variations of K_2O and Fe_2O_3 concentrations were observed between the two methods, most probably due to the concentration which were not calculated accurately.

The rock art paint on the Ha Khotso fragment is due to Ca and can be related to the cream colour of the rock art paint. The Si_2O concentrations from the sandstone rock, compared well for the two techniques. However several differences in compound concentration for the two techniques can be attributed to the fact that the paint on the fragment is most probably layered, heterogeneous and non-uniform distribution of the elements in the analysed region. Additional differences are spectrometer collimation and X-ray penetration depths.

Stellenbosch University http://scholar.sun.ac.za

CHAPTER 6

CONCLUSIONS AND RECOMMENDATIONS

6.1 CONCLUSIONS

Homogeneous SRMs of metal alloys, coins and rock standards with a range of different atomic numbers and known elemental concentrations were used for the validation of the Amptek SDD and Niton XL3t spectrometers.

The compound concentrations for the metal alloys agreed well with the known concentrations of the SRMs. From the Nordic gold coin it was learned that the Al concentration were not determined by the PD method used for the Amptek SDD, it appears to be an issue with low energy line detection. Therefore in order to determine the elemental concentration values for Zn and Cu a limiting concentration needed to be entered into the PD-FP code. Furthermore the roughness due to the engraving on the coin was not observed to play a significant role in the specific instance of Nordic gold coin. Very little difference was observed with the two spectrometers between the smooth and rough surfaces. Measurements on a Krugerrand coin and brass alloy (with known concentrations) were performed to demonstrate that the concentration of high atomic number elements, such as Au and Pb can be accurately measured.

The validation of the SRMs concentrations was very important to advance the investigation to more complex rock art paintings with heterogeneous and layered properties.

The characterisation of the rock art fragments, by identifying the elements of the paint was successfully done. Form the rock art fragment measurements it was found that the PD-FP method is not effective for low atomic number elements, but with the assumption that the balance from the Niton XL3t is correct, we have observed some agreement for the higher atomic numbers compounds. This is therefore by no means a validation of the PD-FP method but rather show the limitation which is understood and yield relative good results when applying the assumption.

A uniform layer of high CaO and Si_2O compound concentrations were measured. The slow percolation of ground-waters through the rock, leaching elements such as Ca, Mg, Fe and K to the surface of the rock [43] is the most likely reason. The variation of the composition for the different paint colours was hence not observed. The CaO layer appears to be invisible to the naked eye and possibly acts as a preserver of the rock art. This may hold the answer to long term conservation of rock art. A limited comparison of the compound concentrations between the two

Stellenbosch University http://scholar.sun.ac.za

spectrometers showed that CaO and S compounds compared well. It is speculated that the variation in concentration for the K_2O and Fe_2O_3 compound is a result of the PD method not calculating the concentration accurately.

Form the Ha Khotso fragment a reduction in the CaO compound concentration from the front to the back of the rock was observed with both techniques. This contribution is a result of the rock art paint and a relation between the high CaO concentration and the cream colour were established. The difference in compound concentrations between the PIXE and pXRF technique can be contributed to factors such as the differences in penetration depth due to the difference in energy with which the sample is bombarded, the heterogeneous distribution of elements in the analysed area and difference in spectrometer collimation.

In general high accuracy results can be obtained with pXRF by following a sound scientific methodology, with specific knowledge and expertise, not only about the XRF technique, but also about the sample under investigation. Furthermore if appropriate sample preparation is applied, errors resulting from surface roughness, particle size effect or heterogeneous of the material can be eliminating or minimised which will result in high accuracy. Measuring the analysed points 5 times and obtaining the same results, indicated that the particle size and inhomogeneities did not have much effect on the compound compositions.

Stellenbosch University http://scholar.sun.ac.za

6.2 RECOMMENDATIONS

We (as a community) need to integrate the pXRF instruments into archaeological studies, with the goal to produce accurate results that are comparable across instruments and manufacturers. This can be done by instrumentation improvements, characterisation of the effect of rock properties such as grain size, surface texture and weathering on the elemental concentrations measurements and determining optimised measurement condition such as the use of a helium environment for low atomic number compound measurements. The determination of the rock art paint thickness can also provide useful information, which can improve the accuracy of the compound concentrations since it can be ensured that the compound concentration detected is only from the paint layer.

Furthermore, the conservation properties of the CaO layer need to be investigated. This could possible results in the development of a paint, which can be applied to the rock art sketches for conservation purposes.

Stellenbosch University http://scholar.sun.ac.za

BIBLIOGRAPHY

[1] M. Peisach, C.A Pineda and L. Jacobson, Nuclear Analytical Study of Rock Paintings, Journal of Radioanalytical and Nuclear Chemistry, Articles, Vol. 151, No.1, 221 – 227, 1991.

[2] J.D Lewis-Williams, The rock art of Southern Africa, Cambridge University Press, Cambridge, England, 1983.

[3] M.J Nuevo, A. Martin Sanchez, C.Oliveira and J. de Oliveira, In situ energy dispersive X-ray fluorescence analysis of rock art pigment from the 'Abrigo dos Gaivoes' and 'Igreja dos Mouros' cave (Portugal), X-ray Spectrometry, Vol 41, Jan 2012.

[4] A. N. Shugar, Portable X-ray Fluorescence and Archaeology: Limitations of the Instrument and Suggested Methods to achieve desired results, Art Conservation Department, Buffalo State College, New York.

[5] S.A.E. Johansson, J. L. Campbell, PIXE: A Novel Technique for elemental analysis, John Wiley & Sons, New York, 1988.

[6] C.G Ryan, D.R. Cousens, S.H Sie and W.L. Griffin, Quantitative analysis of PIXE spectra in Geoscience applications, Nuclear Instruments and Methods in Physics Research B49, 271 – 276, 1990.

[7] Certified of Analysis, Fluorspar granite, Reference Material SARM-48, Mintek.

[8] L. Jacobson, W.A. Van der Westhuizen, J. Oosthuysen, SARM-69 Ceramic-1: A new pottery certified reference material for inter- and intra-laboratory calibration.

[9] G.L Bosco, Development and application of partable, handheld X-ray fluorescence spectrometers, Trends in Analytical Chemistry, Vol. 45, 121, 2013.

[10] S. Piorek, PPrinciples and applications of man-portable X-ray fluorescence spectrometry, Trends in analytical chemistry, Vol. 13, no.7, page 281, 1994.

Stellenbosch University http://scholar.sun.ac.za

[11] N. Craig, R.J. Speakman, R.S Popelka-Filcoff, M.D Glascock, J.D Robertson, M.S Shackley, M.S Aldenderfer, Comparison of XRF and pXRF for analysis of archaeological obsidian from southern Peru, Journal of Archaeological Science, 34, 2012 - 2024, 2007.

[12] E. Gliozzo, R. Arletti, L. Cartechini, S. Imberti, W.A Kockelmann, I. Memmi, R. Rinaldi, R.H Tykot, Non-invasive chemical and phase analysis of Roman bronze artefacts from Thamusida (Marocco), Applied Radiation and Isotopes, 68, 2246 – 2251, 2010.

[13] Horiba Scientific, XRF Analysis, http://www.horiba.com/scientific/products/x-ray-fluorescence-analysis/tutorial.

[14] A.C Thompson, D.T Attwood, E.M Gullikson, M.R Howells, J.B Kortright, A.L Robinson, J.H Underwood, K. Kim, J. Kirz, I. Lindau, P. Pianetta, H. Winick, G.P. Williams, J.H. Scofield, D.Vaughan, X-ray Data Booklet, X-ray emission energies.

[15] R. E. Van Grieken, A. A. Markowicz, Handbook of X-ray Spectrometry, Second Edition, Practical Spectroscopy Series Volume 29, 2002, p 47 (Appendix I, Table 4), p 12 (7), p 219 (5), p 232 (2), p 233 (5), p 233 (6), p 234 (1), p 235 (Figure 22), p 47 (Appendix I, Table 4), p 249 (2), p 247 (4), p 221 (4), p 225 (2), p 230 (2), p 261 (2), p 306 (3 & 4), p 311 (2), p 265 (1), p 268-269, p 295 (2), p 312, p 312 – 314, p 314.

[16] M.S Shackley, An introduction to x-ray fluorescence spectrometry (XRF) analysis in archaeology. In M.S. Shackley (ed.), X-Ray Fluorescence, Spectrometry (XRF) in Geoarchaeology, pp.7–44. New York: Springer, 2011:30.

[17] Thermo Scientific, Using XRF to Sort, Identify and Analyse Scrap Metals and Alloys in the Recycling Industry with Thermo Scientific Niton XL3t Handheld Alloy Analyzers.

[18] A.Niculae, P.Lechner, H.Soltau, G.Lutz, L.Struder, C.Fiorini, A.Longoni, Optimized readout method of silicon drift detectors for high-resolution X-ray spectrometry, Nuclear Instruments and Methods in Physics Research Section A: Accelerators, Spectrometers, Detectors and Associated Equipment, Volume 568, Issue 1, 30, Pages 336 – 342, November 2006.

Stellenbosch University http://scholar.sun.ac.za

[19] Silicon Drift Detector (SDD) with 125 ev FWHM, Amptek, Figure 12.

[20] Brian Cross, XRF-FP Software Guide v.4.6.0, CrossRoads Scientific, Feb 2010.

[21] V.M. Prozesky, W.J. Prybylowicz, E. van Achterbergh, C.L Churms, C.A. Pineda, K.A. Springhorn, J.V. Pilcher, C.G. Ryan, J. Kritzinger, H.Schmitt, T.Swart, The NAC nuclear microprobe facility, Nuclear Instruments and Methods in Physics Research B 104 (1995) 36 – 42.

[22] N.R. Yoder, IUCF VME Data Acquisition System User Information, Indiana University Cyclotron Facility, 1994, unpublished.

[23] C.G. Ryan, E. van Achterbergh, C.J. Yeasts, T.T. Win, G. Gripps, Nucl. Instr. and Meth. B189 (2002) 400.

[24] Instrumentation for PIXE and RBS, IAEA-TECDOC-1190, International Atomic Energy Agency, December 2000

[25] J.W. Criss, L.S. Birks, Calculation method for fluorescent x-ray spectrometry. Empirical coefficients versus fundamental parameters, Analytical Chemistry, Volume 40, page 1080, 1968.

[26] XL3t DTSC's Portable X-ray Fluorescence Operating Procedure (SOP), SOP, Appendix A, September 2007.

[27] G.R Lachance, Demystification of Algorithms and Influence Coefficients in Quantitative XRF Analysis, JCPDS-International Centre for Diffraction Data, 1999.

[28] R. M. Rousseau, Concept of the influence coefficient, The Rigaku Journal, Vol. 18, No.1, 2001.

[29] P.Duvauchell, G.Peix, D.Babot, Effective atomic number in Rayleigh to Compton scattering ratio, Nuclear Instruments and Mrthods in Physics Research B, 155 , 1999, 221 – 228.

[30] V.Rackwitz, V.D Hodoroaba, An attempt of exploiting the Compton-to-Rayleigh Intensity Ration for improved analysis with µXRF and a SEM, Microsc. Microanal 18 (Suppl 2), 2012.

Stellenbosch University http://scholar.sun.ac.za

[31] M.Donativi, S.Quarta, R. Cesareo, A.Castellano, Rayleigh to Comton ratio with monochromatic radiation from an X-ray tube (preliminary results), Nuclear Instruments and Methods in Physics B, 264 (2007), 189 -193.

[32] East Coast Stainless Inc, Stainless steel 410 certificate of analysis.

[33] Hussy copper, CDA 715 certificate of analysis.

[34] Special metals, Inconel 600 certificate of analysis.

[35] Carpenter, Technical Database, Titanium CP Grade 2 certificate of analysis.

[36] KME, Nordic gold coin certificate of analysis.

[37] Birch Gold Group, South African Krugerrand.

[38] T. Maggs, Iron Age communities of the southern Highveld, Natal Museum, Occasional Publications 2, Pietermaritzburg, 1976.

[39] British Columbia Geological Survey, MINIFILE Coding Manual Version 5.0, Information Circular 2007-4, Appendix VII - Conversion Factors.

[40] Caves and Cave Art of Lesotho, Southern Africa, Belfry Bulletin No 391/392, November / December 1980.

[41] A. Watchman, ii. Properties and Dating of Silica Skins associated with Rock Art. Unpublished PhD Thesis, University of Canberra, Canberra, 1996

[42] J.F Lovering, Epigenetic common opal from the Hawkesbury Sandstone Formation of the Sydney Basin. Records of the Australian Museum 23:29–32, 1952

[43] A. Watchman, What are silica skins and how are they important in rock art conservation? Australian Aboriginal Studies (1):21–29, 1990

[44] Mount Ayliff climate; http://www.saexplorer.co.za/south-africa/climate/mount_ayliff_climate.asp

[45] T. Wells, G. Hancock and J. Fryer, Weathering rates of sandstone in a semi-arid environment (Hunter Valley, Australia). Environmental Geology 54:1047–1057, 2008.

Stellenbosch University http://scholar.sun.ac.za

[46] C.R Twidale, Geomorphology: With Special Reference to Australia. Melbourne: Nelson, 1968:136–137.

[47] N.Cook, I. Davidson, S. Sutton, Why are so many ancient rock paintings red? Australian Aboriginal Studies (1):30–33, 1990.

[48] P.J Potts, Introduction, analytical instrumentation and application overview. In P.J. Potts and M. West (eds), Portable X-Ray Fluorescence Spectrometry: Capabilities for In Situ Analysis, pp.1–12. Cambridge: Royal Society of Chemistry Publishing, 2008.

[49] M.A Smith, B. Fankhauser, M. Jercher, The changing provenance of red ochre at Puritjarra rock shelter, Central Australia: Late Pleistocene to present. Proceedings of the Prehistoric Society 64:275–292, 1998.

[50] O. Williams-Thorpe, The application of portable x-ray fluorescence analysis to archaeological lithic provenancing. In P.J. Potts and M. West (eds), Portable X-Ray Fluorescence Spectrometry: Capabilities for In Situ Analysis, pp.174–205. Cambridge: Royal Society of Chemistry Publishing, 2008.

[51] C.G. Ryan, Quantitative trace element imaging using PIXE and the nuclear microprobe, Int. J. Imag. Syst. Tech. 11 (2000) 219–230.

[52] C.G. Ryan, D.N. Jamieson, Dynamic analysis - on-line quantitative PIXE microanalysis and its use in overlap-resolved elemental mapping, Nucl. Instrum. Methods Phys. Res. B 77 (1993) 203–214.

[53] C.G. Ryan, D.N. Jamieson, C.L. Churms, J.V. Pilcher, A new method for on-line true-elemental imaging using PIXE and the proton microprobe, Nucl. Instrum. Methods Phys. Res. B 104 (1995) 157–165.

[54] J. Huntley, Taphonomy or paint recipe: In situ portable X-ray fluorescence analysis of two anthropomorphic motifs from the Woronora Plateau, New South Wales.

Stellenbosch University http://scholar.sun.ac.za

[55] P.J Potts, O. Williams-Thorpe, P.C. Webb, The bulk analysis of silicate rocks by portable x-ray fluorescence: Effect of sample mineralogy in relation to the size of the excited volume, The Journal of Geostandards and Geoanalysis 21(1):29–41, 1997.

[56] Digital Pulse Processor, DP5, Amptek.

[57] Stainless steel 316 product data sheet, AK Steel.

[58] Al 29-4-C alloy technical data sheet, ATI.

[59] F-255 alloy data sheet, Corrosion Materials.

[60] 20Cb3 alloy specification, Alloy Wire International.

Stellenbosch University http://scholar.sun.ac.za

APPENDIX A:

DIGITAL PULSE PROCESSOR [56]

The function of the digital pulse processor is to digitize the preamplifier output, applies real-time digital processing to the signal, detects the peak amplitude and bins this value in its histrogramming memory to generate an energy spectrum. The proses steps is illustrated in Figure A.1 for the DP5 used by the Amptek SDD.

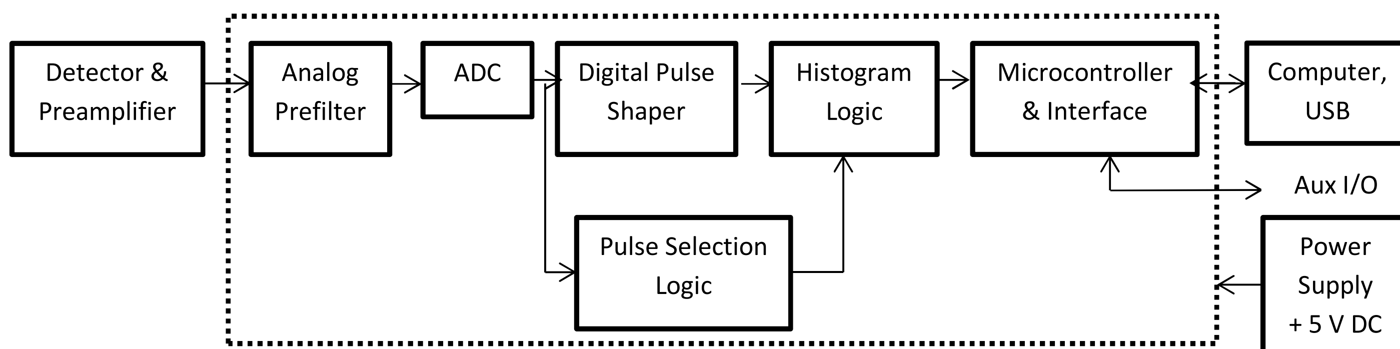

Figure A.1: Block diagram of the Amptek SDD digital pulse processor DP5 [56].

The analog prefilter receives its input from the output of a charge sensitive preamplifier. The main function of this circuit are applying the appropriate gain and offset to utilize the dynamic range of the ADC, and carrying out some filtering and pulse shaping functions to optimize the digitization.

ADC digitizes the output of the analog prefilter at a 20 to 80 MHz rate then sends it in real time to the digital pulse shaper. Two parallel signal processing paths inside the Digital Pulse Shaper receives the output from the ADC, which is being processed continuously by using pipeline architecture to generate a real time shapping amplifier. The shaped pulse is a purely digital entity. There are two parallel signal processing paths inside the DPP, the 'fast' and the 'slow' channels, optimized to obtain different data about the incoming pulse train. The 'slow' channel, has a long shaping time constant, is optimized to obtain accurate pulse heights. The peak value for each pulse in the slow channel, a single digital quantity, is the primary output of the pulse shaper. The 'fast' channel is optimized to obtain timing information: detecting pulses which overlap in the slow channel, measuring the incoming count rate, measuring pulse risetimes etc. The DP5 from Amptek SDD, uses trapezoidal pulse shaping, which offers high energy resolution.

Stellenbosch University http://scholar.sun.ac.za

The pulse selection logic rejects pulses for which an accurate measurement cannot be made. It includes pileup rejection, risetime discrimination logic for an external gating signal etc. At high count rates, the DP5 has both better pileup reject and higher throughput than a traditional, analog shaping amplifier.

Histogramming memory operates as in a traditional MCA. When a pulse occurs with a particular peak value, a counter in a corresponding memory location is incremented. The result is a histogram, an array containing, in each cell, the number of events with the corresponding peak values. This energy spectrum is the primary output of the DP5.

The DP5 includes hardware and software to interface between these various functions and the user's computer. The main function is however to transmit the spectrum to the user. Alternatively it controls the data acquisition, by starting and stopping the processing and by clearing the histogram memory. It also controls certain aspects of the analog and digital shaping, by setting the analog gain or pulse shaping time.

APPENDIX B:

PD-FP TFR INPUT FILE

B.1 LAYER TABLE

```
1
"Thick","Type","Thick.Error","Thick.Units","Density","Fixed","Norm.Flag","Total"
0,"Bulk",0,"mg/cm2",0,"No","On",100
```

B.2 SAMPLE TABLE

```
15
"Layer","Component","Type"
1,"Si","Calc"
1,"Fe","Calc"
1,"Ca","Calc "
1,"Ti","Calc "
1,"P","Calc"
```

```
1,"Mn","Calc"
1,"K","Calc"
1,"C","Calc"
1,"N","Calc"
1,"S","Calc"
1,"Ni","Calc"
1,"Zr","Calc”
1,"Sr","Calc"
1,"Rb","Calc"
1,"Al","Calc"
```

B.3 ELEMENT TABLE

```
15
"Elmt","Line","Cond.Code","Intensity","Int.Err","Back.Int","Back.Err","n-
sigma","Type","Int.Method","Ratio Method","ROI
Low","High","Chi2","Quant.Meth.","Conc","Error","MDL","Atomic%","TCC","TCC
Error","CC","CC2","CC3","LowMT","HighMT"
"C ","Ka",0,0,0,0,0,0,"ConcThresh","Gaussian","None",0,0,0,"None",30,0,0,41.70259,0,0,0,0,0,0,0
"N ","Ka",0,0,0,0,0,0,"ConcThresh","Gaussian","None",0,0,0,"None",30,0,0,35.76014,0,0,0,0,0,0,0
"Al","Ka",0,2.616379,.1811982,0,0,0,"ConcThresh","Gaussian","None",1.410023,1.56298,1.433366,"None"
,1,0,0,.6187962,0,0,0,0,0,0,0
"Si","Ka",1,0,0,0,0,0,"ConcThresh","Gaussian","None",1.661607,1.817797,1.160309,"FP",0,0,0,0,0,0,0,0,0,
0,0
"P
","Ka",1,0,0,0,0,0,"ConcThresh","Gaussian","None",1.933303,2.093103,.3202974,"FP",0,0,0,0,0,0,0,0,0,0,0
"S
","Ka",0,37.40493,.6851221,0,0,0,"ConcThresh","Gaussian","None",2.225513,2.388894,33.37701,"None",.
5,0,0,.260334,0,0,0,0,0,0,0
"K
```

","Ka",0,24.44316,.5382372,0,0,0,"ConcThresh","Gaussian","None",3.224485,3.400429,7.140087,"None",.
9997905,0,0,.4269381,0,0,0,0,0,0,0
"Ca","Ka",0,911.4768,3.286759,0,0,0,"ConcThresh","Gaussian","None",3.5995,3.780319,288.5868,"None",
25.7606,0,0,10.73147,0,0,0,0,0,0,0
"Ti","Ka",0,10.91994,.3597536,0,0,0,"ConcThresh","Gaussian","None",4.412144,4.603585,4.966556,"None
",.2616434,0,0,9.126124E-02,0,0,0,0,0,0,0
"Mn","Ka",0,3.50993,.2039596,0,0,0,"ConcThresh","Gaussian","None",5.788303,5.998248,1.692336,"None
",2.499507E-02,0,0,7.596178E-03,0,0,0,0,0,0,0
"Fe","Ka",0,220.5539,1.616786,0,0,0,"ConcThresh","Gaussian","None",6.289094,6.505564,87.97106,"Non
e",1.134782,0,0,.3392659,0,0,0,0,0,0,0
"Ni","Ka",0,3.54477,.2049694,0,0,0,"ConcThresh","Gaussian","None",7.354451,7.584724,6.17233,"None",
1.098668E-02,0,0,3.125295E-03,0,0,0,0,0,0,0
"Rb","Ka",0,4.776441,.2379289,0,0,0,"ConcThresh","Gaussian","None",13.20637,13.52494,.4070899,"Non
e",2.823822E-02,0,0,5.516309E-03,0,0,0,0,0,0,0
"Sr","Ka",0,38.8594,.6786457,0,0,0,"ConcThresh","Gaussian","None",13.96578,14.29735,8.155778,"None"
,.2525188,0,0,4.811708E-02,0,0,0,0,0,0,0
"Zr","Ka",0,3.49832,.203622,0,0,0,"ConcThresh","Gaussian","None",15.55333,15.91295,3.023425,"None",
2.644894E-02,0,0,4.840742E-03,0,0,0,0,0,0,0

B.4 CONDITION TABLE (ACQUIRE / PROCESSING PARAMETERS)

```
1
"Target","Filter","Thick.(um)","kV","uA","Det.Type","Det.Filter","Thick.(um)","Atmos","Preset
Time","Acq.Time","Smooths","Escape","Sum","Backgrd.","Blank","Blank File"
"C/R Ratio","Compton(c/s)","ROI-Low","ROI-High","Rayleigh(c/s)","ROI-Low","ROI-High","Monitor"
"W ","None",1.5,40,5,"Si pin","None",300,"Air",0,318.752,2,"Yes","Yes","Auto","No",""
"No",0,0,0,0,0,0,0
```

B.5 DETECTOR PARAMETERS

```
"Det.Z","FWHM(eV)","Type","Model","Area(mm2)","Coll.(mm)","Thk.(mm)","Ice(nm)"
14,165,2,0,7,5,.3,0
"Contact(Z)","Cont.Thk(nm)","DL(um)","Azimuth","DetAngle","Alpha","Pressure(Torr)"
79,0,0,0,45,0,0
```

B.6 WINDOW PARAMETERS

```
"Wnd.Type","Thick(um)","Coat(Z)","Coat(nm)","C
Cont(nm)","Grid(nm)","Gr.Fract","Grid2(Z)","Grid2(nm)","Gr2.Fract"
1,25.4,13,0,0,0,0,0,0,0
```

B.7 GEOMETRY PARAMETERS

```
15,0,0,15,45,45,45,90,0,0
```

B.8 TUBE PARAMETERS

```
74,1,3,0,1,0,1.5,90,500,"CapOptic.txt","TubeFile.txt",90,1
4,100
8,64
0,0
0,0
0,0
0,0
```

0,0
0,0
0,0
0,0
0,0
0,0
0,0
0,0
0,0
0,0
0,0
0,0
0,0
0,0
0,0
0,0
0,0
0,0

Stellenbosch University http://scholar.sun.ac.za

APPENDIX C:
ADMCA

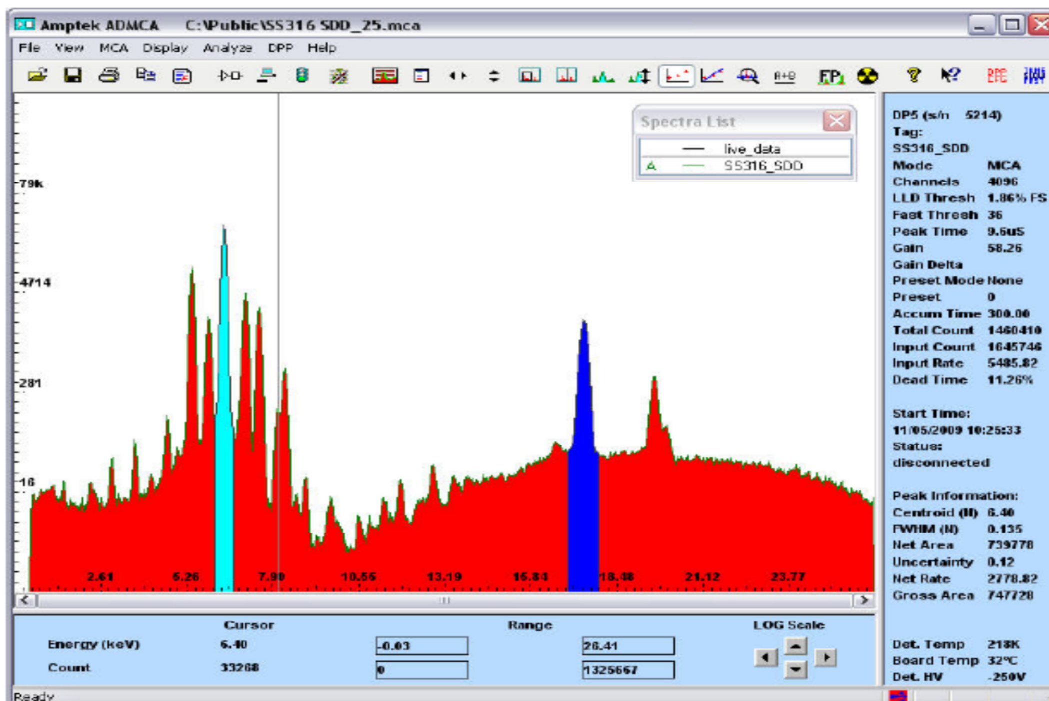

Figure C.1: ADMCA program main display window.

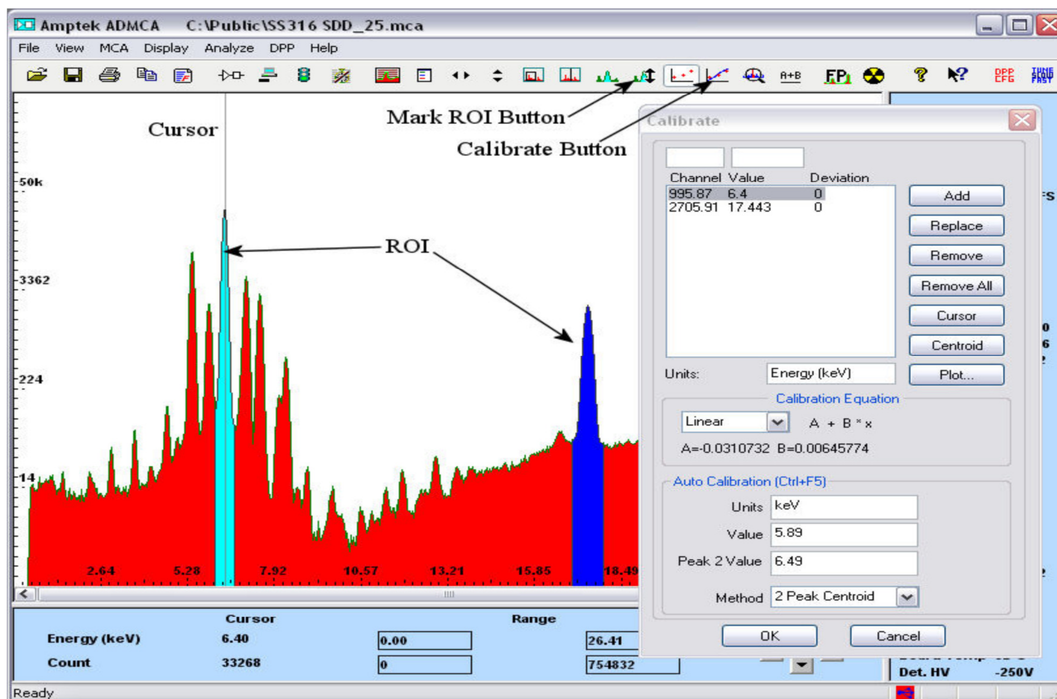

Figure C.2: ADMCA window and calibrate dialog box.

Stellenbosch University http://scholar.sun.ac.za

APPENDIX D:

LEVERBERG-MARQUARDT ALGORITHM

The gradient and first-order expansion form the basis of the popular Leverberg-Marquardt algorithm.

D.1 Gradient method [15]

For the gradient method the fitting function y = y(x,a) and χ^2 defined as a function of m parameters a_j

$$\chi^2 = \chi^2(a) = \sum_{i=1}^{n} \frac{1}{\sigma^2{}_i} [y_i - y(x_i, a)]^2 \tag{D.1}$$

The gradient of χ^2 in the m-dimensional parameter space is given by

$$\nabla\chi^2 = \sum_j \frac{d\chi^2}{da_j} \boldsymbol{j} \tag{D.2}$$

where **j** is the unit vector along the axis *j* and the components of the gradient are given by

$$\frac{\partial\chi^2}{\partial a_j} = -2 \sum_i \frac{1}{\sigma^2{}_i} [y_i - y(x_i, a)] \frac{\partial y}{\partial a_j} \tag{D.3}$$

where β_j is defined as

$$\beta_j = -\frac{1}{2} \frac{\partial\chi^2}{\partial a_j} \tag{D.4}$$

The gradient gives the direction in which χ^2 increases most rapidly. A method to locate the minimum can thus be developed on this basis. Given the set of parameters a_j, a new set of parameters a'_j is calculated, for all *j* simultaneously:

$$a'_j = a_j + \Delta \mathrm{a_j}\, \beta_j \tag{D.5}$$

which follows the direction of steepest descent and guarantees a decrease of χ^2 (at least if the appropriate step sizes Δa_j are taken).

The gradient method works well away from the minimum, but near the minimum, the gradient becomes to small (or even zero) and thus is not a good method to use on its own.

Stellenbosch University http://scholar.sun.ac.za

D.2 First-order Expansion [15]

By writing the fitting function y(x_i, a) as a first-order Taylor expansion of the parameters a_j around y_0

$$y(x,a) = y_0(x,a) + \sum_j \frac{\partial y_0(x,a)}{\partial a_j}\,\delta a_j \quad \text{(D.6)}$$

We obtain an approximation to the fitting function which is linear in the parameter increments δa_j. $y_0(x,a)$ is the value of the fitting function for some initial set of parameters *a*. By inserting equation D.6 into equation D.1 the χ^2 function can be express as

$$\chi^2 = \sum_i \frac{1}{\sigma^2{}_i}\left[y_i - y_0(x_i,a) - \sum_j \frac{\partial y_0(x_i,a)}{\partial a_j}\,\delta a_j\right]^2 \quad \text{(D.7)}$$

The linear least squares method can now be used to find parameters δa_j so that χ^2 will be minimal. Fitting the difference $y_i' = y_i - y_0(x_i,a)$ with the derivatives as variables and the increments δa_j as unknowns.

As defined in the linear least squares fitting section previously:

$$X_j = \frac{\partial y_0(x_i)}{\partial a_j} \quad \text{(D.8)}$$

$$\beta_j = \sum_{i=1}^{n} \frac{1}{\sigma_i^2}\,[y_i - y_0(x_i)]\,\frac{\partial y_o(x_i)}{\partial a_j} \quad \text{(D.9)}$$

$$\alpha_{jk} = \sum_{i=1}^{n} \frac{1}{\sigma_i^2}\,\frac{\partial y_0(x_i)}{\partial a_j}\,\frac{\partial y_0(x_i)}{\partial a_k} \quad \text{(D.10)}$$

Defining a set of *m* normal equations in the unknowns δa_j,

$$\beta = \alpha\delta\alpha \quad \text{(D.11)}$$

with solution

$$\delta a_j = \sum_{k=1}^{m} \alpha^{-1}{}_{jk}\,\beta_k \quad \text{(D.12)}$$

thus

$$\beta_j = -\frac{1}{2}\frac{\partial \chi_0^2}{\partial a_k} \quad \text{(D.13)}$$

and the component of the gradient of χ^2 at the point of expansion

$$\alpha_{jk} \approx \frac{1}{2}\frac{\partial^2 \chi_0^2}{\partial a_j \delta a_k} \quad \text{(D.14)}$$

Thus, α_{jk}, is the first-order approximation to the curvature matrix whose inverse is the error matrix.

Stellenbosch University http://scholar.sun.ac.za

The first-order expansion of the fitting function is closely related to the first order Taylor expansion of the χ^2 hypersurface itself:

$$\chi^2 = \chi_0^2 + \sum_j \frac{\partial \chi_0^2}{\partial a_j} \delta a_j \tag{D.15}$$

where χ_0^2 is the χ^2 function at the point of expansion:

$$\chi_0^2 = \sum_{i=1}^{n} \frac{1}{\sigma_i^2} [y_i - y_0(x_i, a)]^2 \tag{D.16}$$

At the minimum, the partial derivation of χ^2 with respect to the parameter a_k will be zero:

$$\frac{\partial \chi^2}{\partial a_k} = \frac{\partial \chi_0^2}{\partial a_k} + \sum_j \frac{\partial^2 \chi_0^2}{\partial a_j \partial a_k} \delta a_k = 0 \tag{D.17}$$

This results in a set of equations in the parameters δa_k:

$$\frac{\partial \chi_0^2}{\partial a_k} = -\sum_{j=1}^{m} \frac{\partial \chi_0^2}{\partial a_j \partial a_k} \delta a_k \tag{D.18}$$

$$\beta_k = \sum \alpha_{jk} \delta a_k \tag{D.19}$$

which is the same set of equations, except that in the expansion of the fitting function, only a first-order approximation of the curvature matrix is used.

Near the minimum the first-order expansion of the χ^2 surface is a good approximation. We can also conclude that the first-order expansion of the fitting function will yield parameter increments δa_j which will direct us towards the minimum.

For each linear parameter in the fitting function, the first-order expansion of the function in this parameter is exact and the calculated increment δa_j will be such that the new value $a_j + \delta a_j$ is optimum.

D.3 Marquardt Algorithm [15]

Since the gradient method is effective away from the minimum and the first-order expansion is useful near the minimum, Marquardt developed an algorithm that combines both methods using a scaling factor λ that moves the algorithm either in the direction of the gradient search or into the direction of first-order expansion

The diagonal terms of the curvature matrix are modified as follows:

$$\alpha'_{jk} = \begin{cases} a_{jk}(1+\lambda), & j = k \\ \alpha_{jk}, & j \neq k \end{cases} \tag{D.20}$$

where α_{jk} is given by equation D.10

Stellenbosch University http://scholar.sun.ac.za

$$\alpha_{jk} = \sum_{i=1}^{n} \frac{1}{\sigma^2{}_i} \frac{\partial y_0(x_i)}{\partial a_j} \frac{\partial y_0(x_i)}{\partial a_k} \tag{D.21}$$

and the matrix equation to be solved for the increments δ a_j is

$$\beta_j = \sum_k \alpha'_{jk} \, \delta \, a_k \tag{D.22}$$

When λ is very large (λ >> 1), the diagonal elements of α dominate and the equation reduce to

$$\beta_j \approx \alpha'_{jj} \, \delta \, a_k \tag{D.23}$$

or

$$\delta \, a_k \approx \frac{1}{\alpha'_{jj}} \beta_j \approx \frac{1}{\alpha'_{jj}} \frac{d \, \chi^2}{d \, a_k} \tag{D.24}$$

which is the gradient, scaled by a factor α'_{jj} .

For small values of λ (λ << 1) the solution is very close to first-order expansion.

The algorithm proceeds as follows:

1. Given some initial values of the parameters a_j , evaluate $\chi^2 = \chi^2(a)$ and initialize λ = 0.0001
2. Compute **β** and **α** matrices
3. Modify the diagonal elements $\alpha'_{jj} = \alpha_{jj} + \lambda$ and compute δa
4. If $\chi^2(\boldsymbol{a} + \delta\boldsymbol{a}) \geq \chi^2(\boldsymbol{a})$ increase λ by a factor of 10 and repeat Step 3;
   If $\chi^2(\boldsymbol{a} + \delta\boldsymbol{a}) < \chi^2(\boldsymbol{a})$ decrease λ by a factor of 10
   accept new parameters estimates $\boldsymbol{a} \leftarrow \boldsymbol{a} + \delta\boldsymbol{a}$ and repeat Step 2.

The algorithm thus performs two loops: the inner loop incrementing λ until χ^2 starts to decrease and the outer loop calculating successively better approximations to the optimum values of the parameters. The outer loop can be stopped when χ^2 decreases by a negligible absolute or relative amount. Once the minimum is reached, the diagonal elements are an estimate of the uncertainty in the fitting parameters just as in the case of linear least squares: $s_{aj}^2 = \alpha_{jj}^{-1}$
which is equal to $(\alpha_{jj}')^{-1}$ providing the scaling factor λ is much smaller than 1.

Stellenbosch University http://scholar.sun.ac.za

APPENDIX E:
FP EQUATION

By dividing the numerator and denominator of the FP method (equation 4.11) by μ_i^* gives the expression [28]:

$$P_i = \frac{P_{(i)}\, C_i}{C_i + \sum_j K_{ij} C_j} \qquad \text{(E.1)}$$

which leads to the algorithm

$$C_i = R_i\left[C_i + \sum_j K_{ij} C_j\right] \qquad \text{(E.2)}$$

where $R_i = \frac{P_i}{P_{(i)}}$ and Tertian proposed a matrix effect in K_{ij} coefficient

$K_{ij} = \frac{K_{ij}^* - C_i\, h_{ij}}{1+(1-C_i)h_{ij}}$ with K_{ij}^* coefficient relating the absorption effect, while h_{ij} relates the enhancement effect

To eliminate the term C_i on both sides of equation (E.2), Lachance and Traill proposed the expression

$$C_i = R_i\left[1 + \sum_j a_{ij\lambda} C_j\right] \qquad \text{(E.3)}$$

where $a_{ij\lambda} = \left\{\frac{\mu_j^* - \mu_i^*}{\mu_i^*}\right\} = \left\{K_{ij\lambda} - 1\right\}$

and usable for theoretical procedures of monochromatic excitation source, absorption and binary element system.

Criss and Birks [25] proposed that the integrals be replaced by a finite summation over the number of discrete effective wavelength intervals and furthermore that the experimentally measured of the X-ray tube spectra should be used as excitation sources for theoretical calculations. This gave the 'Fundamental Parameter Approach' with general form:

$$P_i + S_i = g_i C_i \sum_\lambda \frac{I_\lambda \mu_{i\lambda}}{absorption\ term}\ (enhancement\ term) \qquad \text{(E.4)}$$

From the general form, the concept of theoretical influence coefficients was developed by de Jongh, Rousseau, Lachance and Claisse with the expression [27]

$$P_{(i)} C_i = P_i + S_i + \sum_j A_{ij} C_j - \sum_j E_{ij} C_j \qquad \text{(E.5).}$$

Stellenbosch University http://scholar.sun.ac.za

APPENDIX F:

NITON XL3t AND AMPTEK SDD FOR IRON (Fe) ALLOY METALS

Elements	Atomic number	Niton XL3t Concentration (wt %)	Amptek Conctration (wt %)	SRM Concentration (wt%)
Mo	42	2.19 ± 0.01	3.04 ± 0.03	2.0 – 3.0
Ni	28	11.16 ± 0.06	9.97 ± 0.07	10.0 – 14.0
Fe	26	67.68 ± 0.07	66.88 ± 0.17	63.0 – 72.0
Mn	25	1.84 ± 0.04	1.62 ± 0.02	2.0 max.
Cr	24	16.84 ± 0.04	18.08 ± 0.07	16.0 – 18.0
Other	Low	0.29	-	1.01 max.

Table F.1: Niton XL3t and Amptek SDD measurements for Stainless Steel 316 [57].

Elements	Atomic number	Niton XL3t Concentration (wt %)	Amptek Conctration (wt %)	SRM Concentration (wt %)
Mo	42	3.85 ± 0.011	3.74 ± 1.44	4.0
Ni	28	0.23 ± 0.02	0.19 ± 0.03	0.3
Fe	26	66.08 ± 0.08	64.94 ± 0.51	65.2 - 66.2
Mn	25	0.34 ± 0.04	0.49 ± 0.06	0.5
Cr	24	28.47 ± 0.06	30.36 ± 0.30	29.0
Other	Low	1.03	-	1.01 max.

Table F.2: Niton XL3t and Amptek SDD measurements for Al 29-4-C alloy [58].

Stellenbosch University http://scholar.sun.ac.za

Elements	Atomic number	Niton XL3t Concentration (wt %)	Amptek Conctration (wt %)	SRM Concntration (wt %)
Mo	42	3.73 ± 0.01	3.49 ± 0.10	2.9 – 3.9
Cu	29	1.45 ± 0.02	1.44 ± 0.12	1.5 – 2.5
Ni	28	5.76 ± 0.05	5.94 ± 0.24	4.5 – 6.5
Fe	26	63.48 ± 0.08	62.16 ± 0.66	58.6 – 67.1
Mn	25	0.96 ± 0.04	1.28 ± 0.08	1.5 max.
Cr	24	24.37 ± 0.05	25.92 ± 0.31	24.0 – 27.0
Other	Low	0.25	-	1.36

Table F.3: Niton XL3t and Amptek SDD measurements for F-255 alloy [59].

Elements	Atomic number	Niton XL3t Concentration (wt %)	Amptek Conctration (wt %)	SRM Concentration (wt %)
Mo	42	2.17 ± 0.01	3.74 ± 1.24	2.0 – 3.0
Cu	29	3.09 ± 0.03	3.13 ± 0.12	3.0 – 4.0
Ni	28	33.07 ± 0.07	33.35 ± 0.34	32.0 – 38
Fe	26	40.96 ± 0.06	39.38 ± 0.32	31.0 - 43.0
Cr	24	19.39 ± 0.04	19.38 ± 0.20	19.0 – 21.0

Table F.4: Niton XL3t and Amptek SDD measurements for 20Cb3 alloy [60].

APPENDIX G:

AMPTEK SDD AND NITON XL3t COMPOUND CONCENTRATION RATIO VALUES FOR S, K_2O, CaO AND Fe_2O_3

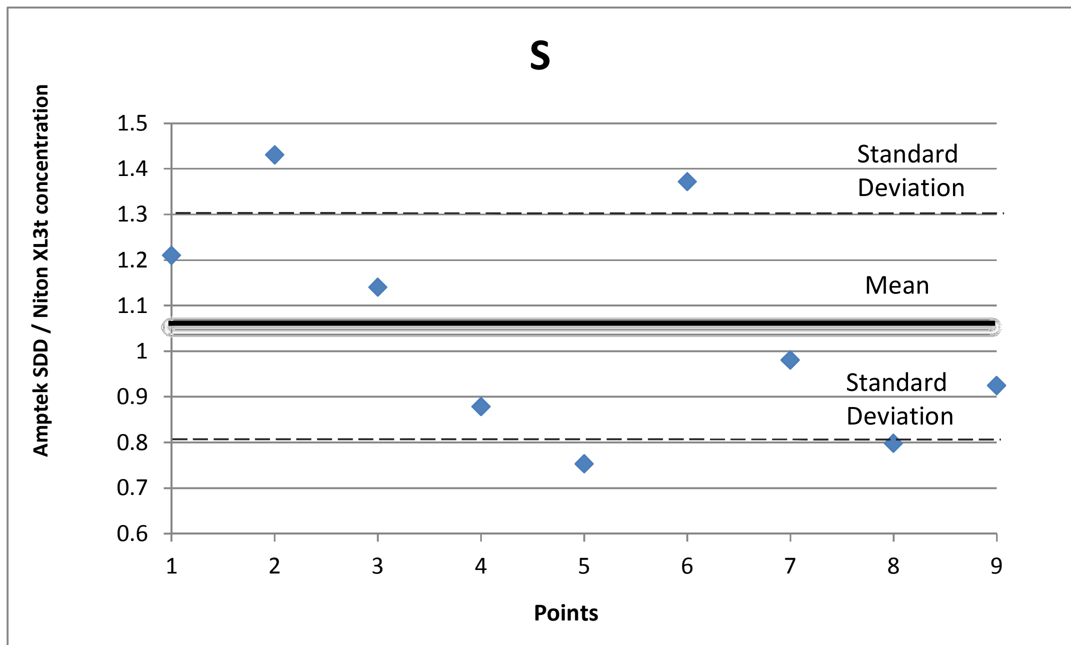

Figure G.1: Amptek SDD and Niton XL3t ratio value for S at all points analysed.

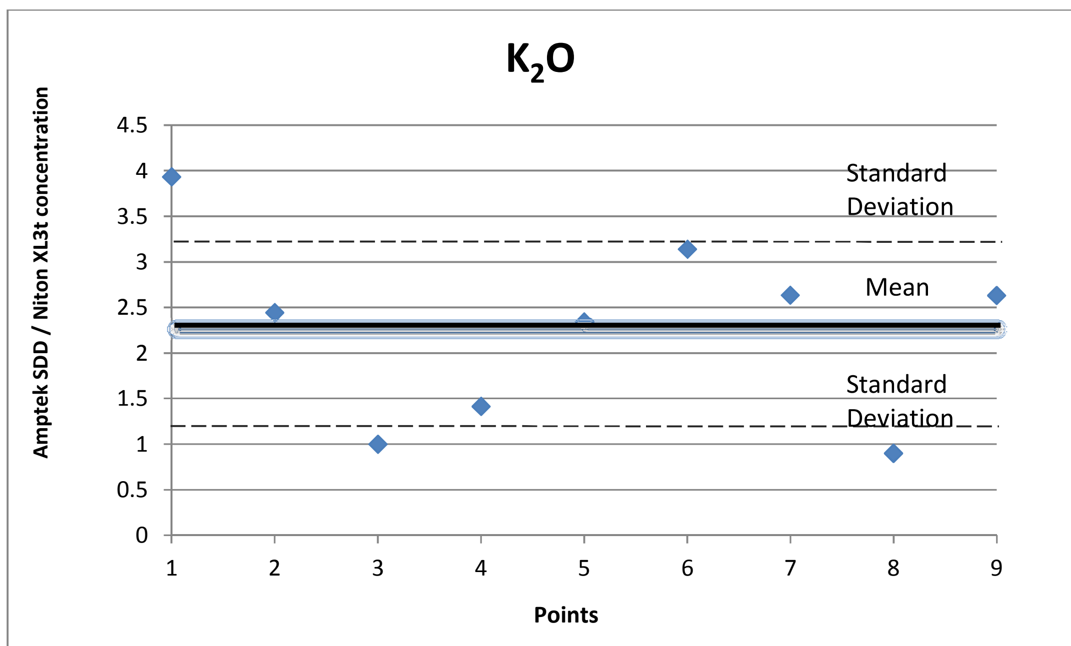

Figure G.2: Amptek SDD and Niton XL3t ratio value for K_2O at all points analysed.

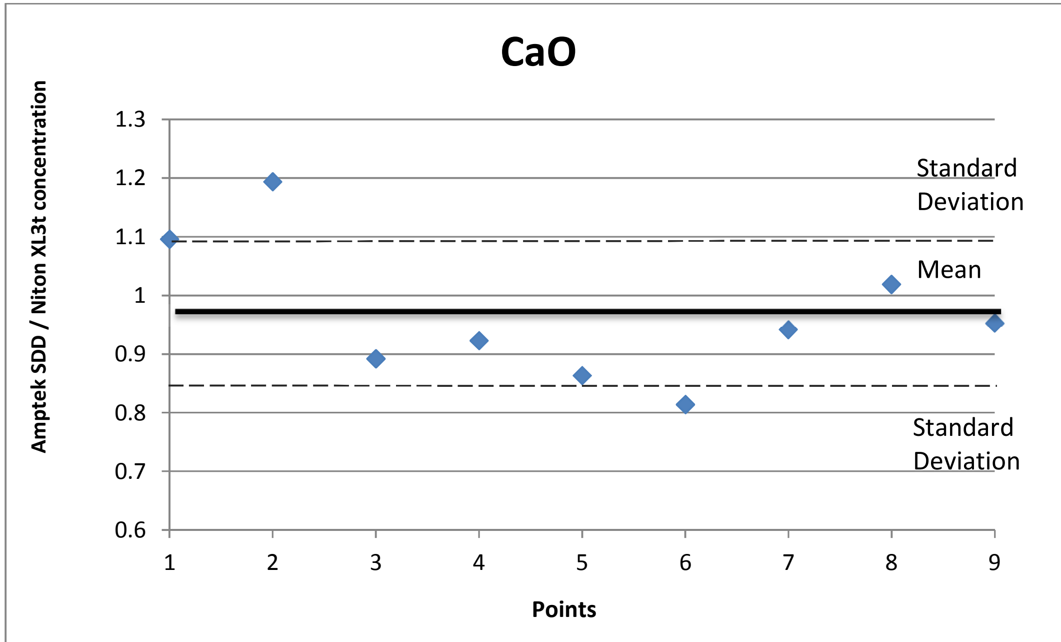

Figure G.3: Amptek SDD and Niton XL3t ratio value for CaO at all points analysed.

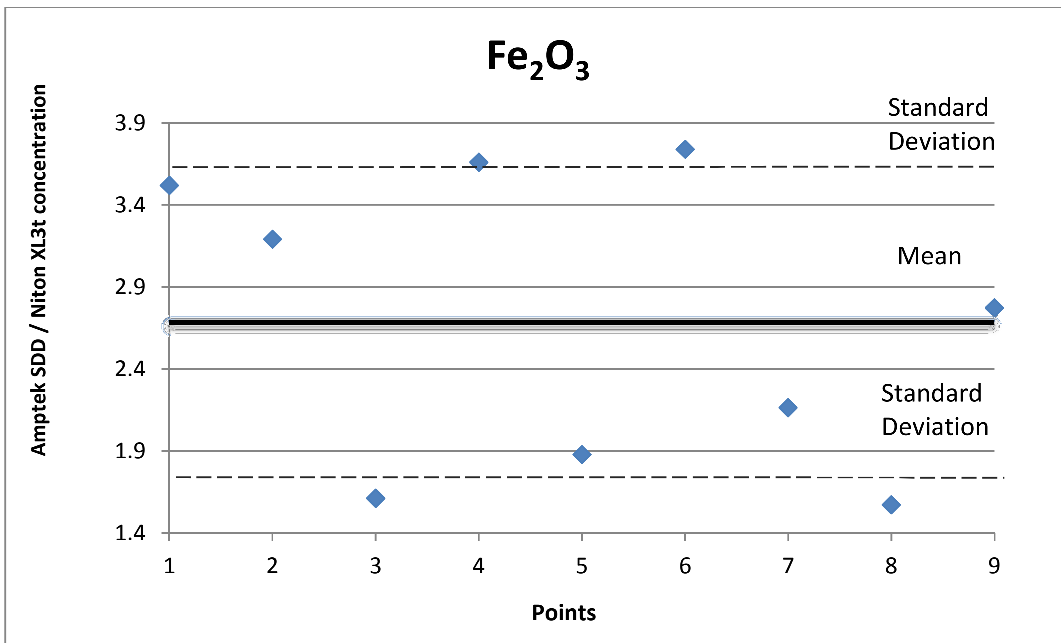

Figure G.4: Amptek SDD and Niton XL3t ratio value for Fe_2O_3 at all points analysed.

Stellenbosch University http://scholar.sun.ac.za

APPENDIX H:

ELEMENTAL MAPS OF THE HA KHOTSO ROCK OBTAINED WITH THE PIXE METHOD

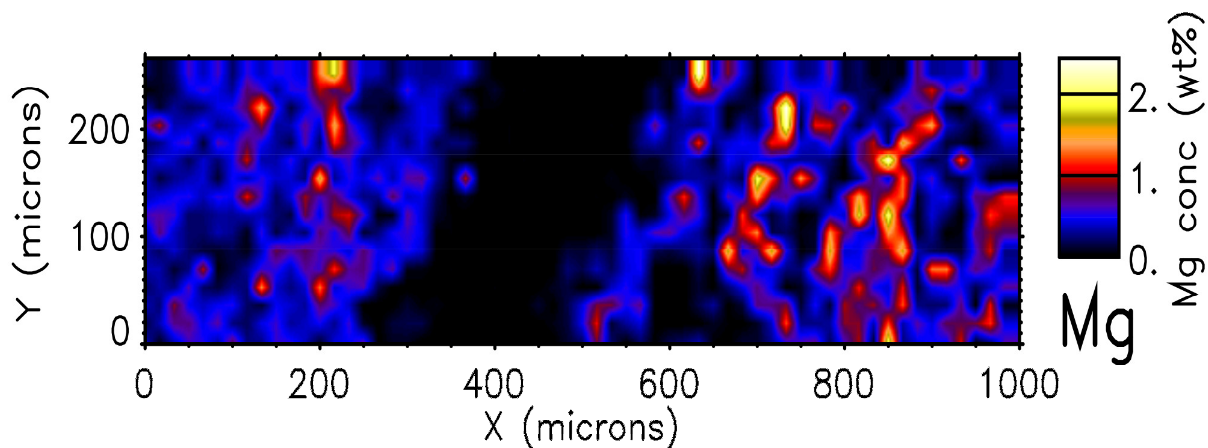

Figure H.1: Mg PIXE elemental composition map for the front of the rock.

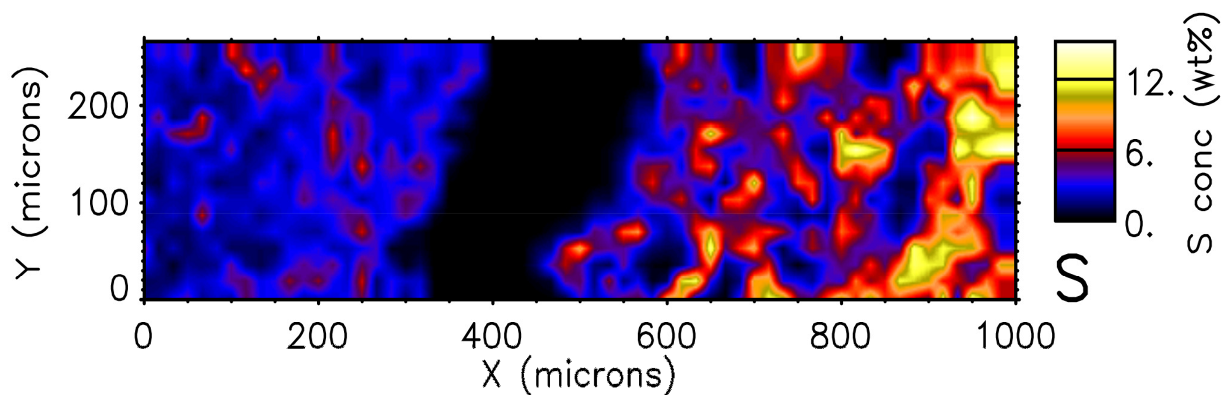

Figure H.2: S PIXE elemental composition map for the front of the rock.

Stellenbosch University http://scholar.sun.ac.za

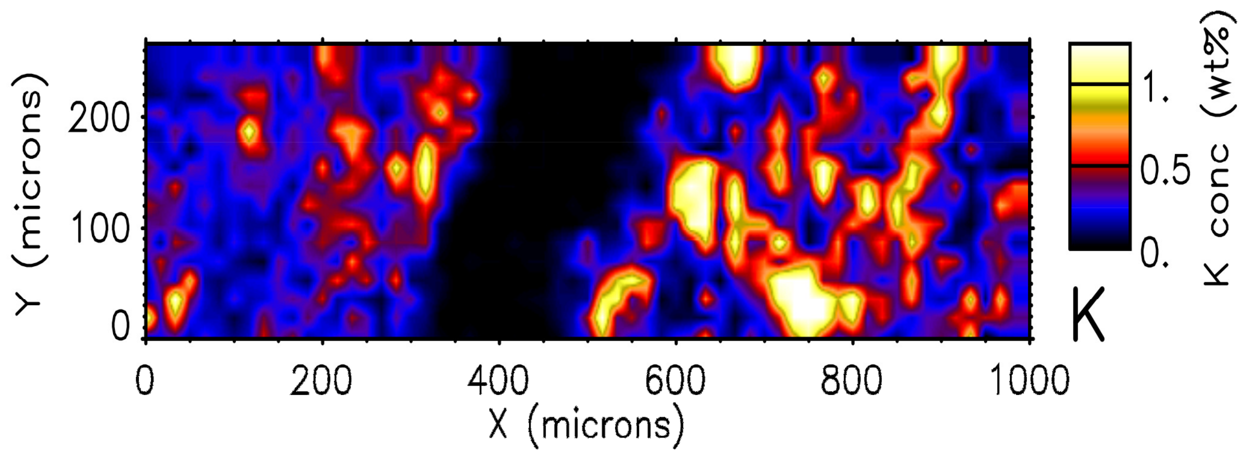

Figure H.3: K PIXE elemental composition map for the front of the rock.

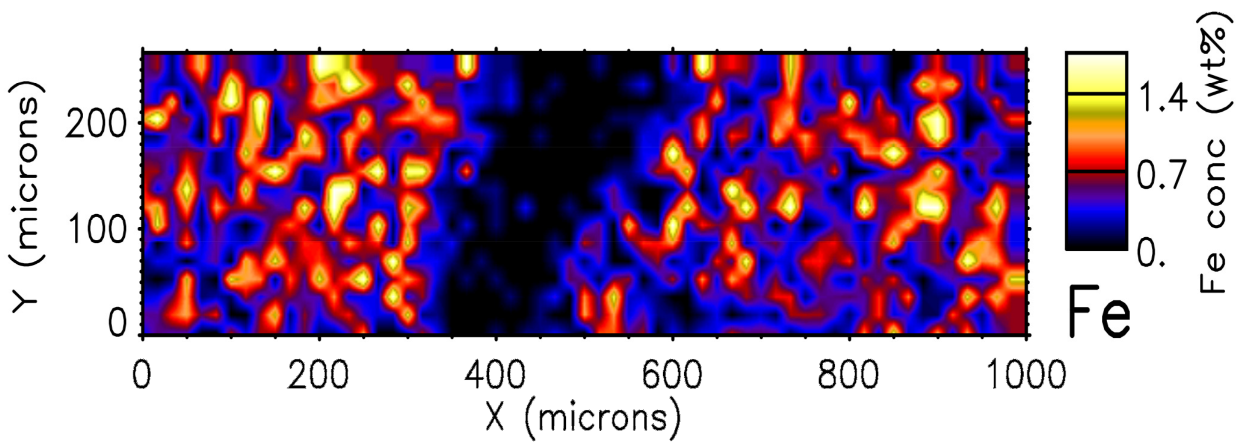

Figure H.4: Fe PIXE elemental composition map for the front of the rock.